VERTICALLY INTEGRATED MODELS OF BOTTOM MIXED LAYER GROWTH IN THE OCEAN

CENTRE FOR NEWFOUNDLAND STUDIES

TOTAL OF 10 PAGES ONLY
MAY BE XEROXED

(Without Author's Permission)

YOU-HUANG JIN

VERTICALLY INTEGRATED MODELS OF BOTTOM MIXED LAYER GROWTH IN THE OCEAN

YOU-HUANG JIN

A thesis submitted to the School of Graduate Studies

in partial fulfillment of the requirements for

the degree of Doctor of Philosophy

DEPT OF PHYSICS

MEMORIAL UNIVERSITY OF NEWFOUNDLAND

January 1991

National Library of Canada
Bibliothèque nationale du Canada

Canadian Theses Service
Service des thèses canadiennes

Ottawa, Canada
K1A 0N4

The author has granted an irrevocable non-exclusive licence allowing the National Library of Canada to reproduce, loan, distribute or sell copies of his/her thesis by any means and in any form or format, making this thesis available to interested persons.

L'auteur a accordé une licence irrévocable et non exclusive permettant à la Bibliothèque nationale du Canada de reproduire, prêter, distribuer ou vendre des copies de sa thèse de quelque manière et sous quelque forme que ce soit pour mettre des exemplaires de cette thèse à la disposition des personnes intéressées.

The author retains ownership of the copyright in his/her thesis. Neither the thesis nor substantial extracts from it may be printed or otherwise reproduced without his/her permission.

L'auteur conserve la propriété du droit d'auteur qui protège sa thèse. Ni la thèse ni des extraits substantiels de celle-ci ne doivent être imprimés ou autrement reproduits sans son autorisation.

ISBN 0-315-65327-2

SUBJECT CATEGORIES

Dissertation Abstracts International is arranged by broad, general subject categories. Choose the *one* listed below (capital letters) which most nearly describes the general content of your dissertation. If the major subject category has sub-fields under it, and *only* if it does, please choose *one* (small letters). (Ex.: ECONOMICS, Theory). Enter subject category on Item 7 of Agreement Form.

HUMANITIES

IA COMMUNICATIONS AND THE ARTS
- ARCHITECTURE
- CINEMA
- FINE ARTS
- INFORMATION SCIENCE
- JOURNALISM
- LIBRARY SCIENCE
- MASS COMMUNICATIONS
- MUSIC
- SPEECH
- THEATER

IIA EDUCATION
- EDUCATION
  - General
  - Administration
  - Adult
  - Agricultural
  - Art
  - Audiovisual
  - Business
  - Community and Social
  - Community Colleges
  - Curriculum and Instruction
  - Early Childhood
  - Elementary
  - Finance
  - Guidance and Counseling
  - Health
  - Higher
  - History
  - Home Economics
  - Industrial
  - Language and Languages
  - Mathematics
  - Middle School
  - Minorities
  - Music
  - Personality Development and Mental Hygiene
  - Philosophy
  - Physical
  - Preschool
  - Programmed Instruction
  - Psychology
  - Religion
  - Sciences
  - Secondary
  - Social Sciences
  - Special
  - Teacher Training
  - Teaching Machines
  - Tests and Measurements
  - Theory and Practice
  - Vocational

IIIA LANGUAGE, LITERATURE AND LINGUISTICS
- LANGUAGE
  - General
  - Ancient
  - Linguistics
  - Modern
- LITERATURE
  - General
  - Classical
  - Comparative
  - Medieval
  - Modern
  - American
  - Asian
  - Dutch and Scandinavian
  - English
  - Germanic
  - Latin American
  - Romance
  - Russian and East European
  - Slavic and Finno-Ugrian

IVA PHILOSOPHY, RELIGION AND THEOLOGY
- PHILOSOPHY
- RELIGION
  - General
  - Clergy
  - History
  - Music
  - Philosophy
- THEOLOGY

VA SOCIAL SCIENCES
- ACCOUNTING
- AMERICAN STUDIES
- ANTHROPOLOGY
  - Archaeology
  - Cultural
  - Physical
- BANKING
- BUSINESS ADMINISTRATION
- ECONOMICS
  - General
  - Agricultural
  - Commerce-Business
  - Finance (includes Public Finance)
  - History
  - Theory
- FOLKLORE
- HISTORY
  - General
  - Ancient
  - Medieval
  - Modern
  - Black
  - Church
  - Africa
  - Asia
  - Australia and Oceania
  - Canada
  - Europe
  - Latin America
  - United States
- HISTORY OF SCIENCE
- LAW
- MANAGEMENT
- MARKETING
- POLITICAL SCIENCE
  - General
  - International Law and Relations
  - Public Administration
- PUBLIC RELATIONS
- RECREATION
- SOCIAL GEOGRAPHY
- SOCIAL STRUCTURE
- SOCIAL WORK
- SOCIOLOGY
  - General
  - Community Organization
  - Criminology
  - Demography
  - Educational
  - Individual and Family Studies
  - Industrial
  - Labor Relations
  - Public Welfare
  - Race Relations
  - Social Problems
  - Statistics–Research Methods
  - Theory
- TRANSPORTATION
- URBAN AND REGIONAL PLANNING
- WOMEN'S STUDIES

SCIENCES

IB BIOLOGICAL SCIENCES
- AGRICULTURE
  - General
  - Animal Culture
  - Animal Pathology
  - Forestry & Wildlife
  - Plant Culture
  - Plant Pathology
  - Plant Physiology
  - Range Management
  - Wood Technology
- AGRONOMY
- ANATOMY
- BIOLOGICAL OCEANOGRAPHY
- BIOLOGY
- BIOPHYSICS
  - General
  - Medical
- BIOSTATISTICS
- BOTANY
- ECOLOGY
- ENTOMOLOGY
- GENETICS
- LIMNOLOGY
- MICROBIOLOGY
- PHYSIOLOGY
- RADIATION BIOLOGY
- VETERINARY SCIENCE
- ZOOLOGY

IIB EARTH SCIENCES
- GEOCHEMISTRY
- GEODESY
- GEOLOGY
- GEOPHYSICS
- HYDROLOGY
- MINERALOGY
- PALEOBOTANY
- PALEONTOLOGY
- PALEOZOOLOGY
- PHYSICAL GEOGRAPHY
- PHYSICAL OCEANOGRAPHY

IIIB HEALTH AND ENVIRONMENTAL SCIENCES
- ENVIRONMENTAL SCIENCES
- FOOD TECHNOLOGY
- HEALTH SCIENCES
  - General
  - Audiology
  - Chemotherapy
  - Dentistry
  - Education
  - Hospital Management
  - Human Development
  - Hygiene
  - Immunology
  - Medicine & Surgery
  - Mental Health
  - Nursing
  - Nutrition
  - Pathology
  - Pharmacy
  - Public Health
  - Radiology
  - Recreation
  - Speech Pathology
- HOME ECONOMICS
- PHARMACOLOGY

IVB PHYSICAL SCIENCES

PURE SCIENCES
- CHEMISTRY
  - General
  - Analytical
  - Biological
  - Inorganic
  - Nuclear
  - Organic
  - Pharmaceutical
  - Physical
  - Polymer
  - Radiation
  - Water
- MATHEMATICS
- PHYSICS
  - General
  - Acoustics
  - Astronomy & Astrophysics
  - Atmospheric Science
  - Atomic
  - Electronics and Electricity
  - Elementary Particles and High Energy
  - Fluid and Plasma
  - Molecular
  - Nuclear
  - Optics
  - Radiation
  - Solid State
- STATISTICS

APPLIED SCIENCES
- APPLIED MECHANICS
- ASTRONAUTICS
- COMPUTER SCIENCE
- ENGINEERING
  - General
  - Aeronautical
  - Agricultural
  - Automotive
  - Biomedical
  - Chemical (includes ceramics and fuel)
  - Civil
  - Electronics and Electrical
  - Heat and Thermodynamics
  - Hydraulic
  - Industrial
  - Marine
  - Materials Science
  - Mechanical
  - Metallurgy
  - Mining
  - Nuclear
  - Petroleum
  - Sanitary and Municipal
  - System Science
- OPERATIONS RESEARCH
- PLASTICS TECHNOLOGY
- TEXTILE TECHNOLOGY

VB PSYCHOLOGY
- PSYCHOLOGY
  - General
  - Clinical
  - Experimental
  - Industrial
  - Physiological
  - Psychobiology
  - Social

ABSTRACT

A new vertically integrated model is developed for the growth of bottom mixed layers. Unlike the usual slab models this model retains the vertical variation of mean speed with height, which appears as a parameter in the energy balance. The mixed layer growth problem is solved analytically for a horizontal flat bottom and numerically for a sloping flat bottom. A relaxation problem, the decay of motion in the bottom mixed layer after the geostrophic flow in the interior ceases, is also solved analytically and numerically. Finally solutions including thermal wind effects on bottom mixed layer growth are obtained for both a horizontal flat bottom and a sloping flat bottom.

For the horizontal flat bottom case, an algebraic formula for mixed layer thickness is obtained for arbitrary values of the Brunt-Vaisala frequency and Coriolis parameter. The results show that the vertical variation of speed must be taken into account when the ratio of the Brunt-Vaisala frequency to the Coriolis parameter is less than or of order unity, and that the formula is consistent with that obtained by Weatherly and Martin (1978). Formulae for dependence of friction velocity and veering angle on stratification are also obtained.

For a sloping bottom at the initial stage of bottom boundary layer growth the vertically integrated model produces results very similar to those obtained by Weatherly and Martin (1978) using the Mellor and Yamada Level II turbulent

closure model. The main effect of bottom slope is to produce upwelling or downwelling within the bottom boundary layer. After the initial period of boundary layer development the vertically integrated buoyancy force can grow to reach a balance with the vertically integrated driving pressure gradient so that the Ekman transport is extinguished and the layer becomes arrested. The length of the initial period greatly depends on the sign of bottom slope.

The effects of thermal wind are shown to be important. For a horizontal flat bottom if the vertical shear in the interior is positive the mixed layer grows indefinitely. If the vertical shear is negative the thickness reaches a constant value or decreases with time. For a sloping flat bottom the thermal wind is important when the isopycnal slope is comparable to or much greater than the bottom slope. The results are in agreement with the observations made by Weatherly and Van Leer (1977) on the western Florida Continental Shelf.

ACKNOWLEDGEMENTS

I would like to express my sincere gratitude to my supervisor Dr. Alex Hay for his guidance, support, encouragement and patience. He suggested the topic of the thesis and continuously offered numerous ideas and results during the course of the work. Without his considerable help it would have been impossible to complete this thesis.

Thanks are also due to my supervisory committee members Dr. Richard Greatbatch and Dr. Brian Sanderson for their discussions and criticism of this manuscript. Dr. Greatbatch in particular made important suggestions for the thermal wind problem. Special thanks are due to Professor C. Garrett of Dalhousie University for his valuable suggestions. I am also indebted to Professor G. L. Weatherly of the Florida State University who kindly provided me with the results obtained from the Level II turbulent closure model, and to Professor M. Lal of Department of Mathematics, Memorial University of Newfoundland for help in solving the mixed layer equations numerically.

I would also thank Dr. F. Aldrich, Dr. D. Rendell, Dr. C. Sharp and Mrs. J Barron for their assistance in dealing with administrative matters.

I am grateful for the financial support provided to me by ICOD (International Center for Ocean Development), the Department of Physics, the School of Graduate Studies and my supervisor Dr. Alex Hay through grants awarded to him.

Table of Contents

LIST OF SYMBOLS

A	proportionality coefficient
C	proportionality coefficient
C_d	bottom drag coefficient, quadratic drag law
f	Coriolis parameter
g	gravitational acceleration
H	total depth of sea water
h	thickness of mixed layer
h_q	thickness of bottom boundary layer, defined as the height at which the turbulent kinetic energy vanishes.
i	$\sqrt{-1}$
k	von Karman's constant
$\vec{k}$	unit vector in z-axis
KE	kinetic energy of local time-mean flow
N_e	Brunt-Vaisala frequency
n , n_i	power index
P	total pressure

P_o pressure in interior

P' local time averaged pressure in the mixed layer

P'' pressure perturbation to the geostrophic field induced by bottom

$\hat{p}$ turbulent part of pressure

PE gravitational potential energy

$\frac{q^2}{2} = \frac{\hat{u}^2 + \hat{v}^2 + \hat{w}^2}{2}$ turbulent kinetic energy

R_i gradient Richardson number

R_o overall Richardson number

R_o' overall Richardson number for transverse flow

r bottom drag coefficient, linear drag law

S temperature gradient

$SN = N_o$ the Brunt-Vaisala frequency

$\hat{s}_{ij} = \frac{1}{2}(\frac{\partial \hat{u}_i}{\partial x_j} + \frac{\partial \hat{u}_j}{\partial x_i})$

fluctuating rate of strain due to turbulence

T_g ramp period

t time

U_g	x-component of geostrophic velocity
$\vec{U} = (u, v + V_g, w)$	local time averaged velocity
$U = \sqrt{\bar{u}^2 + (\bar{v} + V_g)^2}$	vertically-averaged speed in mixed layer
ΔU	speed less the averaged speed U
U	magnitude of velocity
U	x-component of vertically averaged velocity
(u, v)	velocity component within mixed layer minus geostrophic velocity
$(\bar{u}, \bar{v})$	averaged components of (u, v) over the thickness of mixed layer
$\vec{u} = (u_1, u_2, u_3) = \vec{U} + \vec{u}$	total velocity in mixed layer
$\vec{u}$	turbulent part of velocity $\vec{u}$ scale for u
u_*	friction velocity
$\Delta u = u - \bar{u}$	deviation of u from the vertical mean $\bar{u}$
$VS = \frac{\partial V_g}{\partial z}$	vertical shear of geostrophic velocity
V	y-component of vertically averaged velocity.
V_g	y-component of geostrophic velocity.

$\bar{V}_g$	geostrophic velocity averaged over the thickness of mixed layer
$\Delta v = v - \bar{v}$	deviation of v from the vertical mean $\bar{v}$
w_e	entrainment velocity
(x, y, z)	coordinates of bottom coordinate system with z-axis perpendicular to sea bottom
(x', y', z')	coordinates of a system of which z'-axis is in vertical
α	veering angle
α^i	velocity profile parameter
$\beta = -\frac{\partial H}{\partial x}$	bottom slope
$\beta_1' = -\arctan\left[\frac{\frac{\partial \rho_o}{\partial x}}{\frac{\partial \rho_o}{\partial z}}\right]$	isopycnal slope
$\beta_1 = \beta_1' - \beta$	isopycnal slope relative to bottom
ξ	thermal expansion coefficient
$\varsigma = 2\mu \langle \hat{s}_{ij}\, \hat{s}_{ij} \rangle$	viscous dissipation term
$\langle\ \rangle$	local time averaged turbulent quantities
$\varsigma_1 = \frac{z}{h}$	nondimensional parameter

δ	inertial sublayer thickness
ϵ	advective contribution to the change of density in mixed layer
Φ	dimensionless function
$\vec{\Omega} = (\Omega_x, \Omega_y, \Omega_z)$	angular velocity of earth's rotation
Ω	angular speed of earth's rotation
ρ_o	reference density
$\rho_o(z, z)$	density in the ocean interior
ρ'	local time-averaged density in mixed layer
$\hat{\rho}$	turbulent part of density ρ
ρ''	deviation from density of interior caused by local mixing
$\delta\rho$	density difference across interface
θ	temperature
$\tau_b = \tau_b^x + i\,\tau_b^y$	complex form of bottom stress
$\vec{\tau}_b = (\tau_b^x, \tau_b^y)$	stress on the sea floor
$\vec{\tau}_i = (\tau_i^x, \tau_i^y)$	stress at interface between mixed layer and interior

LIST OF FIGURES

page

page

page

page

page

page

page

page

LIST OF TABLES

page

page

CHAPTER 1

INTRODUCTION

The bottom boundary layer in the ocean is nearly uniform in terms of its physical and chemical properties because of turbulent mixing induced by bottom friction. Therefore it is often called the bottom mixed layer. When the sea floor is inclined, upwelling or downwelling can occur parallel to the bottom within the mixed layer due to the effect of the earth's rotation. This vertical mixing and upwelling or downwelling can have important physical and biological consequences.

In the interior of the ocean we can often assume that the flow is nearly geostrophic. Near the bottom boundary, however, the flow speed must decrease because of friction, and the Coriolis force no longer balances the pressure gradient force. This imbalance drives a near-bottom transverse flow which is directed in the northern hemisphere to the left of the interior geostrophic flow, as first demonstrated by Ekman (1905). Using a constant eddy viscosity for steady flow in a neutrally stratified fluid he showed that the velocity vector follows a logarithmic spiral with distance from the boundary.

In the presence of stratification, a bottom mixed layer is formed and the transverse motion is largely confined to this mixed layer. This transverse flow

affects the budgets of heat, nutrients and other scalars on the continental shelf (Bowden, 1978), mixing at the ocean boundaries (Armi, 1978 and 1979; Garrett, 1979), and the response of the ocean to forcing at time scales larger than the inertial period (Wimbush and Munk, 1970).

There have been several different approaches to the bottom mixed layer problem. In one approach the vertical variation of the turbulent fluxes is retained. This may be through the use of a mixing length hypothesis (Zilitinkevich, 1970) or an eddy viscosity, which may be a function of time and height (Gutman, 1969; Ng and Spalding, 1972). These assumptions permit the set of governing equations to be closed, and the results are given in the form of vertical profiles of velocity, density and other quantities. Recently very promising results have been obtained by requiring closure assumptions for the triple turbulence moments. This approach was reviewed by Mellor and Yamada (1974), and summarized as Levels I to IV of their turbulent closure scheme. Weatherly and Martin (1978) were the first to use a Level II turbulent closure model to investigate the effects of stratification and bottom slope on mixed layer growth in the ocean. In this thesis extensive comparisons are made with their results.

A number of contributions have been made in terms of this approach (Mellor, 1973; Yamada and Mellor, 1975; Weatherly, 1975; Weatherly et al., 1980; Dickey and Van Leer, 1984; etc.). The second order scheme created by Launder et al. (1975) and further developed by Gibson and Launder (1978), Richards (1982)

and Mofjeld and Lavelle (1984) also belongs to this category.

Another approach has been to use similarity theories. Csanady (1967) used dimensional analysis, matching a wall layer with an outer layer in terms of a logarithmic layer existing between them, and obtained a resistance law for a turbulent, stationary, horizontally homogeneous and neutrally stratified atmospheric Ekman boundary layer. For this same problem Blackadar and Tennekes (1968) deduced directly from the equations of motion the wall law, velocity-defect law and the logarithmic law between them for the planetary boundary layers in terms of similarity theory. Brown (1974) achieved a continuous solution for semi-infinite flow over a surface consisting of geostrophic, Ekman-layer, and surface-layer solutions in terms of dimensional analysis.

The third approach is to use equations of motion which are integrated over the boundary layer thickness, which reduces with certain assumptions to the so-called slab model. The advantage of this approach is that after vertical integration the turbulent momentum flux appears in the form of stresses at the bottom boundary and at the interface between the boundary layer and the interior. There was some early observational evidence which indicated that the slab model should be useful, particularly in stably stratified environments. Riehl et al. (1951) and Kraus (1968) showed that there was no apparent evidence of a velocity spiral, logarithmic or otherwise, in the atmospheric boundary layer over the sea. Instead the observations seemed to show the existence of a well-stirred layer

of almost uniform potential temperature, and that even the velocity was more or less constant in this layer. (This result has been corroborated in the ocean more recently by Weatherly and Van Leer (1977), who found that most of the Ekman veering occurs in the strong density gradient region between the bottom mixed layer and the overlying fluid.) This led Geisler and Kraus (1969) to use the slab model with vertically uniform potential temperature and velocity within the well-stirred layer to simulate the growth and the dynamics of the atmospheric boundary layer in the presence of stable stratification. Subsequently, slab models were applied to the oceanic surface mixed layer by Pollard et al. (1973) and to the oceanic bottom mixed layer by Thompson (1973). With assumptions that there exists a thin layer with linear distributions of velocity and density between the mixed layer and the interior the slab model has also been extended by Manins (1982) to include the effects of thermal wind in the interior, and successfully applied to the atmospheric boundary layer. Similarly Price et al. (1986) applied the slab model, with a transition zone to eliminate the density jump between the mixed layer and the interior, to the dynamics of deepening of oceanic upper mixed layers solely driven by the local surface fluxes of heat and momentum.

1.1. Previous Results

These three approaches have yielded the following results for the boundary layer thickness over a horizontal bottom. According to similarity theory

(Csanady, 1967) the thickness h of the Ekman layer for neutrally stratified flow is

$$h = k \frac{u_*}{f} \tag{1.1a}$$

where f is the Coriolis parameter, and u_* is the friction velocity defined by the bottom friction τ_b and the density ρ_o, that is

$$u_* = \sqrt{\frac{|\tau_b|}{\rho_o}}. \tag{1.1b}$$

The value of u_* is often estimated by $0.03 - 0.05\ V_g$ (Weatherly, Blumsack and Bird, 1980) where V_g is the geostrophic velocity. The value of k is usually taken as 0.4, based on laboratory experiments by Caldwell et al. (1972) and Howroyd and Slawson (1975), and field observations made for example by Mercado and Van Leer (1976). Zilitinkevich (1972) theoretically deduced that k is von Karman's constant, which is about 0.4.

When stratification is included it can be shown by using the Rayleigh method and the π - theorem (Pao, 1961) that the thickness for a horizontal flat bottom must take the form

$$h = A \frac{u_*}{f} \Phi\left(\frac{N_o}{f}\right), \tag{1.2}$$

where N_o is the Brunt-Vaisala frequency, $N_o^2 = -\frac{g}{\rho_o}\frac{d\rho_o}{dz}$. The constant A and function Φ need to be determined from additional physical considerations.

Thompson (1973) showed using a slab model that

$$h = 1.2 \frac{u_*}{\sqrt{f N_o}}, \tag{1.3}$$

for constant N_o. Using the Mellor and Yamada Level II closure scheme, Weatherly and Martin (1978) obtained:

$$h = \frac{1.3\, u_*}{f \left(1 + \frac{N_o^2}{f^2}\right)^{\frac{1}{4}}}, \tag{1.4}$$

for $0 \leq \frac{N_o}{f} \leq 200$. It is important to note that Equation (1.4) is not an analytic result, but was shown to provide a reasonable fit to their computed thicknesses. Each of Eqs. (1.3) and (1.4) has the form (1.2).

Note that the physical meaning of h in each of Eqs. (1.1), (1.3) and (1.4) is somewhat different. In Eq. (1.1), the thickness of the Ekman layer is defined by Howroyd and Slawson (1975) as the height at which the velocity is parallel to the geostrophic velocity. Caldwell et al. (1972) and Nowell (1983) define the thickness in Eq. (1.1) to be the height where the velocity is 99%-99.9% of the geostrophic velocity. In Eq. (1.3), h is the thickness of the bottom mixed layer, while in Eq. (1.4) h is defined as the height at which the turbulent kinetic energy goes to zero. Other definitions of bottom boundary layer thickness are similar to these three above. For example, Richards (1982) defined the thickness as the height at which the turbulent kinetic energy is reduced to 5 % of its value at the bottom. This

gives $h = 0.86u_*/f$ for constant geostrophic velocity and $h = 0.57u_*/f$ for a bottom boundary layer driven by the M_2 semi-diurnal tide.

When $\frac{N_0}{f} \gg 1$, Eq. (1.4) approaches $1.3\frac{u_*}{\sqrt{N_0 f}}$ which is very similar to Eq. (1.3). The small difference between them may be due to the different definitions of thickness. Both are in rough agreement with the observations made by Weatherly and Van Leer (1977) on the western Florida Shelf, for which $\frac{N_0}{f} = 203$.

For the case of $\frac{N_0}{f} = 0$, it is found that the thickness obtained from Eq. (1.4) is more than three times that obtained from Eq. (1.1). Weatherly and Martin (1978) attributed this to the different definitions of thickness. Thompson's formula does not apply to this case.

For a sloping flat bottom in the ocean, theoretical results have been presented by Weatherly and Martin (1978) and by Bird et al. (1982). Weatherly and Martin (1978) assumed horizontal isopycnals (no thermal wind) with the interior flow parallel to isobaths, and again used the Mellor and Yamada Level II closure scheme. They solved the problem numerically, for a situation in which density varied solely with temperature. They showed that the bottom mixed layer is no longer a simple, laterally homogeneous well-mixed layer. Instead, it is strongly affected by upwelling (downwelling) of denser (lighter) water induced by Ekman

veering. In the northern hemisphere, for the case of shallow water to the left of the interior flow (upwelling) the density of the bottom mixed layer increases with time due to advection of water from greater depths, and the thickness reaches a constant value which is approximately equal to that given by Eq. (1.4). For the case of shallow water to the right (downwelling) the density of the layer decreases and the thickness increases with time. These results were compared with observations made by Weatherly and Van Leer on the western Florida Continental Shelf, with basically favourable agreement being found, except that for the downwelling case the observed thickness was found to be constant and less than that for the upwelling case. Bird et al. (1982) also used the level II closure model, and included thermal wind effects. They still assumed that all departures from geostrophic flow within the bottom boundary layer were independent of position on the plane parallel to the bottom. Their thermal wind sensitivity studies show that when the isopycnal slope increases, the thickness decreases and the veering angle increases. Rhines and MacCready (1989) showed that the driving pressure gradient force in the upslope direction must finally be balanced by the buoyancy force and the Ekman flux will be extinguished. The Ekman layer becomes arrested.

Contributions to mixing on a sloping bottom in the ocean made by Phillips (1970) and Wunsch (1970) show that a mean upwelling current along the slope induced by the sloping bottom which is different from the simple diffusive process

might account for the vertical velocity needed in the abyssal circulation. Phillips et al. (1986) show that on a sloping bottom there exists a bidirectional secondary flow in the turbulent boundary layer with a net significant downslope buoyancy flux. Garrett (1990) discussed the secondary circulation and the related the turbulent Ekman layer in detail and particularly, verified theoretically the existence of secondary circulation when the turbulent eddy viscosity decreases exponentially with distance away from the bottom.

1.2. Present Approach

In this thesis the vertically integrated equations of motion are used, as in the slab model. The approach differs from that usually employed in slab models, however, in that the vertical dependence of mean speed on height is retained, appearing as a parameter in the energy equation. The objectives are to provide a unified interpretation of Eqs. (1.1), (1.3) and (1.4) for the horizontal bottom case, and to apply the model to bottom mixed layers on a slope and in the presence of thermal wind in the interior flow, which Weatherly and Martin (1978) did not include in their simulations. The results are compared primarily to those obtained by Weatherly and Martin (1978), Bird et al. (1982), and to Weatherly and Van Leer's observations. Chapter 2 presents the analytic solutions for the horizontal flat bottom case. Chapter 3 gives the formulation of the boundary layer problem for a sloping flat bottom. Chapter 4 gives the numerical results for mixed layer

growth over a flat bottom for both the horizontal and sloping cases. Chapter 5 shows how the thermal wind affects the growth of the bottom mixed layer over both a horizontal flat bottom and a sloping flat bottom. The summary and conclusions are presented in Chapter 6. Analytic and numerical results for a relaxation problem in bottom mixed layers are given in Appendix 3.

CHAPTER 2

ANALYTIC SOLUTIONS FOR THE HORIZONTAL FLAT BOTTOM CASE

The problem of bottom mixed layer development over a horizontal flat bottom due to constant geostrophic velocity in the interior is formulated in this chapter. A continuous velocity profile is considered, and vertically integrated governing equations are derived, consisting of the momentum equations, a mass conservation equation and a new energy equation. The energy equation is derived both from first principles and from bulk energy arguments. Analytic solutions for thickness, veering angle and other flow quantities are obtained and compared with previous results.

2.1. Momentum Equations

It is assumed that the fluid is stratified and incompressible, and that the motion is hydrostatic and driven by a constant geostrophic velocity V_g in the y-direction (Fig. 2.1) so that the flow is assumed to be independent of y. Based on observations (see for example, Riehl et al., 1951; Kraus, 1968; Weatherly and Van Leer, 1977; Dickey and Van Leer, 1984), the density within the boundary layer is assumed to be uniform in the vertical direction while the velocity varies with height (Fig. 2.1). This distinction between the dependence of velocity on height and that of other quantities on height is important in the analysis to be

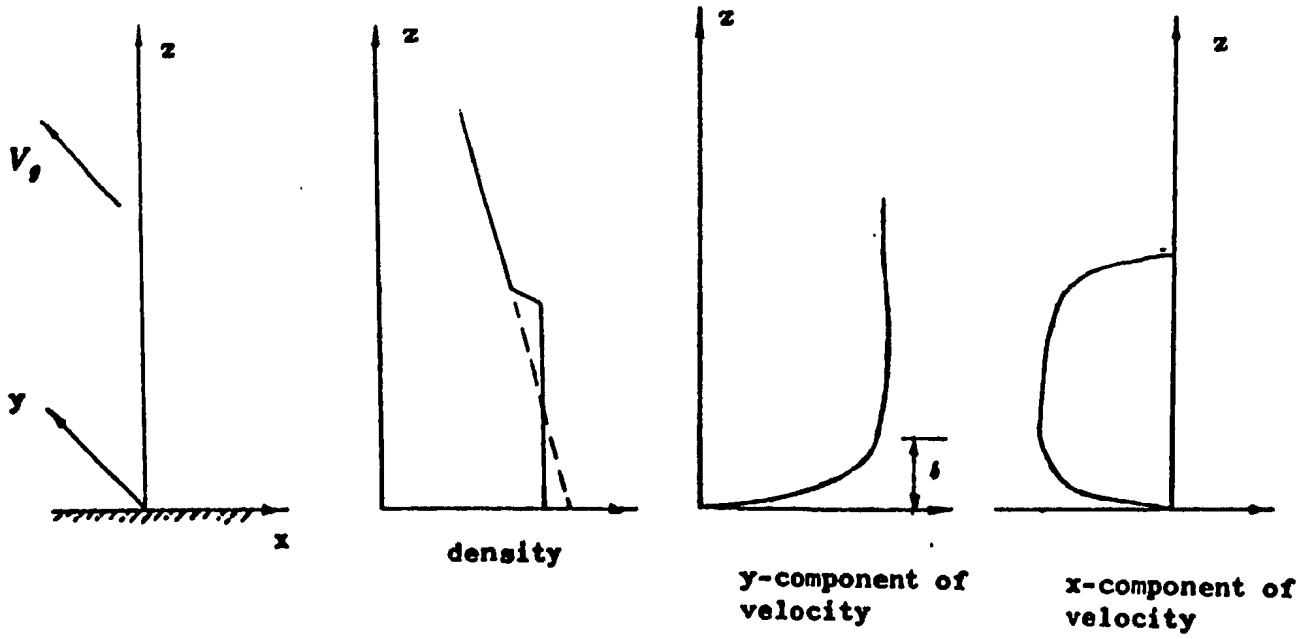

Figure 2.1. Coordinate system and schematic profiles for the horizontal flat bottom problem.

presented.

Let (u, v) be the local time averaged velocity components in the layer minus the interior geostrophic velocity $(0, V_g)$. Then the vertical averages of these quantities are given by

$$\bar{u} = \frac{1}{h}\int_0^h u \, dz \tag{2.1}$$

and

$$\bar{v} = \frac{1}{h}\int_0^h v \, dz \tag{2.2}$$

where h is the height over which the density is well-mixed and uniform.

The continuity equation in the bottom boundary layer is

$$\frac{\partial u}{\partial x} = -\frac{\partial w}{\partial z}. \tag{2.3a}$$

When there is entrainment, the interface at $z = h$ is not a material surface and the kinematic boundary condition can be written in the form

$$w(h) - w_e = u(h)\, h_x + h_t. \tag{2.3b}$$

where w_e is the entrainment velocity. When mass is entrained downward into the bottom boundary layer, w_e is negative and the interface moves upward with an extra speed of w_e besides $w(h)$. Making use of Eq. (2.3b) and integrating Equation (2.3a) the following can be deduced:

$$h_t + \frac{\partial}{\partial x}(h\bar{u}) = -w_e. \tag{2.4}$$

Assuming uniformity in the x-direction (since V_g is independent of x)

$$\frac{\partial}{\partial x}(h\bar{u}) = 0, \tag{2.5}$$

and substituting Eq. (2.5) into Eq. (2.4) yields

$$h_t = -w_e . \tag{2.6}$$

The linearized vertically integrated momentum equations may, therefore, be shown to be

$$\frac{\partial(\bar{u}h)}{\partial t} - f\bar{v}h = -\frac{1}{\rho_o}\tau_b{}^x \tag{2.7}$$

$$\frac{\partial(\bar{v}h)}{\partial t} + f\bar{u}h = -\frac{1}{\rho_o}\tau_b{}^y \tag{2.8}$$

where ρ_0 is a reference density, and $\vec{\tau_b} = (\tau_b{}^x, \tau_b{}^y)$ is the stress at the bottom. These are the same as the momentum equations for the slab model used by Geisler and Kraus (1969), Pollard et al. (1973), and Thompson (1973). To obtain them it has been assumed that the vertical scale is much less than the horizontal scales so that horizontal variations of mean quantities including the horizontal Reynolds stresses can be ignored. The Rossby number is therefore small (Geisler and Kraus, 1969), so that the nonlinear terms can be ignored. Also the Boussinesq approximation has been used. Furthermore, it is assumed that during growth the friction at the interface $\vec{\tau_i}$ is given by

$$\frac{\vec{\tau_i}}{\rho_o} = [u(h), v(h)]\, w_e , \tag{2.9}$$

so that the interfacial friction is due solely to the entrainment of water from the interior into the bottom boundary layer. This assumption was also made by Pollard et al. (1973).

2.2. Energy Equation

The energy balance in the entire water column from surface to bottom is considered, since the geostrophic flow in the interior provides the energy source for mixed layer development. Two approaches are used to obtain an approximate energy equation, one starting from first principles, the other based on a bulk energy argument.

2.2.1. Derivation from first principles.

The derivation of the energy equation starts with the momentum equation:

$$\rho\frac{\partial\vec{u}}{\partial t} + \rho(\vec{u}\cdot\vec{\nabla})\vec{u} + \rho(2\vec{\Omega}\times\vec{u}) = -\vec{\nabla}p - \rho g\vec{k} + \mu\nabla^2\vec{u} \tag{2.10}$$

where μ is the molecular shear viscosity of the fluid, $\vec{k}$ is the vertical unit vector, $\vec{\Omega}$ is the angular speed of the earth's rotation and $\vec{u}$ is the velocity of a fluid particle. If $\vec{u}$ is the turbulent part of the total velocity and $\vec{U} = (u, v + V_g)$ is the local time averaged velocity, the total velocity $\vec{u}$ is

$$\vec{u} = \vec{U} + \vec{u} = (u + \hat{u},\ v + V_g + \hat{v},\ \hat{w}). \tag{2.11a}$$

Similarly ρ and p can be written as

$$\rho = \rho' + \hat{\rho} \tag{2.11b}$$

and

$$p = P' + \hat{p} \tag{2.11c}$$

where $\hat{\rho}$ is the turbulent part of the density, $\hat{p}$ the turbulent part of the pressure, ρ' the local time averaged density and P' the local time averaged pressure. Substituting Eqs. (2.11a) to (2.11c) into Eq. (2.10), taking the dot product of the

resulting equation with $\vec{U}$ and time-averaging yields the mean kinetic energy equation for incompressible flow

$$\frac{\rho_o}{2}\frac{\partial}{\partial t}[u^2 + (v + V_g)^2] = -uP'_x - \rho_o u\frac{\partial}{\partial z}<\hat{u}\hat{w}> - \rho_o(v + V_g)\frac{\partial}{\partial z}<\hat{w}\hat{v}>, \tag{2.12}$$

where the Boussinesq approximation has been invoked in order to set $\rho' = \rho_o$, and the assumptions that $\frac{\partial}{\partial x} \ll \frac{\partial}{\partial z}$ and $\frac{\partial}{\partial y} \ll \frac{\partial}{\partial z}$ have been made which permits the horizontal advection of mean quantities to be ignored. The viscous terms have been dropped because the Reynolds number is large (Wimbush and Munk, 1970; Tennekes and Lumley, 1972).

Similarly the dot product of Eq. (2.10) with $\vec{u}$ produces the turbulent kinetic energy equation

$$\frac{\rho_o}{2}\frac{\partial<q^2>}{\partial t} = -\frac{\partial}{\partial z}<\hat{w}\hat{p}> - \rho_o<\hat{w}\hat{u}>\frac{\partial u}{\partial z} - \rho_o<\hat{w}\hat{v}>\frac{\partial(v + V_g)}{\partial z}$$
$$-\frac{\rho_o}{2}\frac{\partial}{\partial z}<\hat{w}q^2> + \mu\frac{\partial}{\partial z}[<\hat{u}(\frac{\partial\hat{u}}{\partial z} + \frac{\partial\hat{w}}{\partial x})> + <\hat{v}(\frac{\partial\hat{v}}{\partial z} + \frac{\partial\hat{w}}{\partial y})> + 2<\hat{w}\frac{\partial\hat{w}}{\partial z}>]$$
$$-\varsigma - <\hat{w}\hat{\rho}>g, \tag{2.13a}$$

where

$$\varsigma = 2\mu<\hat{s}_{ij}\hat{s}_{ij}> \tag{2.13b}$$

is the dissipation term (see Appendix 1),

$$\hat{s}_{ij} = \frac{1}{2}[\frac{\partial\hat{u}_i}{\partial x_j} + \frac{\partial\hat{u}_j}{\partial x_i}]$$

and

$$q^2 = \hat{u}^2 + \hat{v}^2 + \hat{w}^2.$$

The second term and the third term on the right hand side of Eq. (2.13a) are the shear production terms. The last term is the buoyant production term (Mellor, 1973). Adding Eq. (2.13a) to Eq. (2.12) yields the total kinetic energy balance,

$$\frac{\rho_o}{2}\frac{\partial}{\partial t}(u^2+(v+V_g)^2+\langle q^2\rangle) = -\rho_o\frac{\partial}{\partial z}[u\langle\hat{w}\hat{u}\rangle+(v+V_g)\langle\hat{w}\hat{v}\rangle]$$
$$-uP'_x-\frac{\rho_o}{2}\frac{\partial}{\partial z}\langle\hat{w}q^2\rangle-\frac{\partial}{\partial z}\langle\hat{w}\hat{p}\rangle-\langle\hat{w}\hat{\rho}\rangle g-\varsigma$$
$$+\mu\frac{\partial}{\partial z}[\langle\hat{u}(\frac{\partial\hat{u}}{\partial z}+\frac{\partial\hat{w}}{\partial x})\rangle+\langle\hat{v}(\frac{\partial\hat{v}}{\partial z}+\frac{\partial\hat{w}}{\partial y})\rangle+2\langle\hat{w}\frac{\partial\hat{w}}{\partial z}\rangle]. \quad (2.14)$$

After integration from the bottom to the sea surface, Eq. (2.14) reduces to terms involving integrals of quantities which are non-zero only in the mixed layer:

$$\frac{\rho_o}{2}\int_0^h\left[\frac{\partial}{\partial t}(u^2+(v+V_g)^2+\langle q^2\rangle)\right]dz = -\int_0^h uP'_x\,dz$$
$$-\int_0^h\langle\hat{w}\hat{\rho}\rangle g\,dz-\int_0^h\varsigma\,dz \quad (2.15)$$

The $\frac{\partial}{\partial z}$ terms in Eq. (2.14) do not appear in Eq. (2.15) both because they vanish in the interior above the mixed layer, where it is assumed that the turbulence vanishes, and because they are zero at the bottom boundary due to the no slip condition and $\hat{w}$ being zero at the bottom. These terms redistribute energy within the mixed layer but do not result in any net flux into or out of the layer.

Substituting Eqs. (2.11a) and (2.11b) into the mass conservation equation, $\rho_t+\vec{\nabla}\cdot(\vec{u}\rho)=0$, and time-averaging the result yields

$$\rho'_t=-\frac{\partial}{\partial z}\langle\hat{w}\hat{\rho}\rangle. \quad (2.16a)$$

Therefore when $z < h$

$$- <\hat{w}\hat{\rho}> = \rho'_t z. \tag{2.16b}$$

because the mean density of the mixed layer is independent of z. Note that ρ' is equal to ρ_o at $z = \frac{h}{2}$, where $\rho_o(z)$ is the distribution of density before formation of the bottom mixed layer: that is

$$\rho_o(z) = \rho_o(0) + \rho_{oz}\ z. \tag{2.16c}$$

Therefore $\rho_t' = \frac{1}{2}\rho_{oz} h_t$. Note also from the hydrostatic relation that

$$P' = P_o + \int_z^h (\rho' - \rho_o) g dz$$

where P_o is the undisturbed pressure, and that therefore $P_z' = P_{oz}$ which is independent of z. Eq. (2.15) can therefore be rewritten as

$$\frac{\rho_o}{2}\int_0^h \left[\frac{\partial}{\partial t}(u^2 + (v + V_g)^2 + <q^2>)\right] dz = - h\bar{u}P_{oz}$$
$$+ g\frac{\rho_{oz}}{4}h^2 h_t - \int_0^h \varsigma dz. \tag{2.17}$$

The left hand side of this equation represents the time rate of change of total kinetic energy. The right-hand side is the sum of the rate of work done by the geostrophic pressure gradient, the negative of the time rate of change of potential energy, and total dissipation per unit area in the mixed layer. It remains to express the dissipation in terms of mean flow quantities.

It is assumed that during the growth of the mixed layer,

$$\frac{\rho_o}{2}\int_0^h \frac{\partial <q^2>}{\partial t} dz + \int_0^h \varsigma dz = \vec{\tau}_b \cdot \vec{U}, \tag{2.18}$$

where $\bar{U} = (\bar{u},\ \bar{v} + V_g)$ is the vertically averaged mean velocity. Eq. (2.18) indicates that the total time rate of change of turbulent kinetic energy per unit area plus the total dissipation per unit area is equal to the rate of work done by the mean flow against bottom friction. Justification for assuming this balance is given below.

When the flow is statistically steady Eq. (2.18) can be deduced from Eq. (2.13a). From Eq. (2.16b) $<\hat{\rho}\hat{w}> = 0$ for steady flow, and after vertical integration from the bottom to the sea surface Eq. (2.13a) becomes

$$\int_0^h \varsigma dz = -\int_0^h \left[\rho_o <\hat{w}\hat{u}> \frac{\partial u}{\partial z} + \rho_o <\hat{w}\hat{v}> \frac{\partial (v + V_g)}{\partial z}\right] dz.$$

which is the balance between shear production of turbulent energy and viscous dissipation. Equation (2.18) therefore represents the essentially well known result for homogeneous, steady, pure shear flow that the rate of shear production of turbulent kinetic energy equals the rate of viscous dissipation. The velocity distribution is quite uniform in the upper part of the mixed layer above the inertial sublayer so that most of the shear production of turbulent energy occurs within the lower part of the mixed layer, the inertial sublayer (constant stress layer, Mellor 1973; Kline et al., 1967). Therefore the integral of the shear production term can be rewritten as an integral from 0 to δ where δ is the inertial sublayer thickness. Furthermore the Reynolds stresses are constant in the inertial sublayer, so the right hand side of the above equation can be written as

$$\int_0^\delta \vec{\tau} \cdot \frac{\partial \vec{U}}{\partial z} dz \approx \vec{\tau}_b \cdot \vec{U}_o$$

where $\bar{U}_o$ is the velocity at the outer edge of the inertial sublayer, assumed to be close to the vertically averaged velocity.

For the case of unsteady flow the term $\frac{\partial <q^2>}{\partial t}$ in the inertial sublayer is small relative to other terms in Eq. (2.13a) (Mellor, 1973). The measurements made by Wyngaard and Cote (1971) in the inertial sublayer of the atmospheric boundary layer under stable conditions show that this is true and that the rate of shear production of turbulent energy almost equals the rate of viscous dissipation because the buoyant production and other terms are also quite small. Therefore the integral of Eq. (2.13a) from 0 to δ becomes

$$-\int_0^{\delta}\left[\rho_o <\hat{w}\hat{u}> \frac{\partial u}{\partial z} + \rho_o <\hat{w}\hat{v}> \frac{\partial (v + V_g)}{\partial z}\right] dz \approx \vec{\tau}_b \cdot \vec{U} = \int_0^{\delta} \varsigma dz.$$

In the upper part of the boundary layer viscous dissipation is small when the Reynolds number is large, and therefore $\int_0^{\delta} \varsigma dz \approx \int_0^{h} \varsigma dz$. For completeness the term involving the integral of $\frac{\partial <q^2>}{\partial t}$ is included (although it is expected that this term is small) and Eq. (2.18) is, approximately, obtained. Equation (2.18) was also used by Manins (1982) with an additional turbulent kinetic energy production term caused by surface heat transfer.

Substituting Eq. (2.18) into Eq. (2.17) yields

$$\frac{\rho_o}{2}\int_0^{h}\frac{\partial}{\partial t}[u^2 + (v + V_g)^2]dz - \frac{1}{4} g \rho_{oz} h^2 h_t = -h\bar{u}\rho_o f V_g - \bar{u}\tau_b^x - (\bar{v} + V_g)\tau_b^y \qquad (2.19)$$

since $\frac{\partial P_o}{\partial z} = \rho_o f V_g$. In Eq. (2.19) the last two terms represent the power lost to bottom friction. The first two terms on the left hand side are respectively the time rate of change of local mean kinetic energy per unit area and the time rate of change of potential energy per unit area. The first term on the right hand side is the rate of work done by the geostrophic pressure gradient.

2.2.2. Derivation using bulk energy arguments.

Equation (2.19) can also be obtained using bulk energy arguments. The mean kinetic energy KE in the total water column (see Fig. 2.2) is

$$KE = \int_0^H [u^2 + (v + V_g)^2] dz = \int_0^h [u^2 + (v + V_g)^2] dz + \int_h^H V_g{}^2 dz$$

where H is the total depth. Therefore

$$\frac{\partial KE}{\partial t} = \frac{\rho_o}{2} [\int_0^h \frac{\partial}{\partial t} [u^2 + (v + V_g)^2] dz + [u^2 + (v + V_g)^2] |_{z=h} \frac{\partial h}{\partial t} - V_g{}^2 \frac{\partial h}{\partial t}]$$

$$= \frac{\rho_o}{2} \int_0^h \frac{\partial}{\partial t} [u^2 + (v + V_g)^2] dz.$$

The potential energy per unit area of the water column is

$$PE = \int_0^h \rho' z g dz + \int_h^H \rho_o(z)\, z g dz$$

$$= -\frac{1}{12} g \rho_{os} h^3 + \frac{g}{2} \rho_o(0) H^2 + \frac{g}{3} \rho_{os} H^3.$$

Thus

$$\frac{\partial PE}{\partial t} = -\frac{1}{4} g \rho_{os} h^2 \frac{\partial h}{\partial t}.$$

The rate of working by the geostrophic pressure gradient is

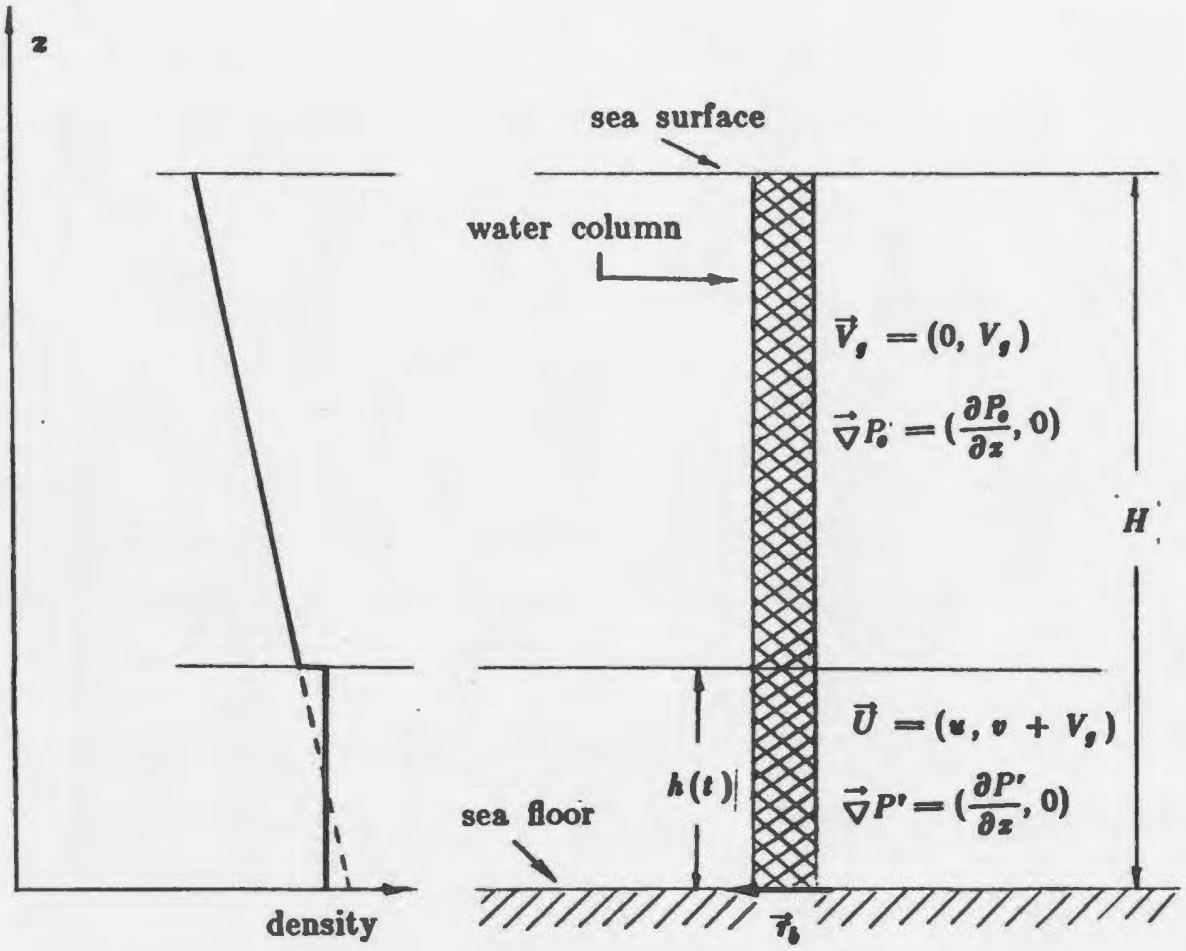

Figure 2.2. A sketch of the water column during bottom mixed layer growth in the view of bulk total energy balance. H is the total depth of water column from the sea floor to the sea surface. $h(t)$ is the thickness of the bottom mixed layer. $\vec{U}(t)$ is the velocity in the layer. $\vec{\tau}_b$ is the bottom friction. $\vec{V}_g$ is the geostrophic velocity. $\vec{\nabla} P$ is the pressure gradient.

$$-\int_0^h \vec{\nabla} P' \cdot \vec{U} dz - \int_h^H \vec{\nabla} P_o \cdot \vec{V}_g dz = -h\bar{u}\rho_o f V_g$$

where, as in Eq. (2.17), $P'_z = P_{oz}$ has been used. If it is assumed that the time rates of change of total mean flow kinetic energy and potential energy in the water column from $z = 0$ to H, plus the power gained from the geostrophic pressure gradient in the bottom boundary layer, are balanced by the power lost to bottom friction, then Eq. (2.19) results. This energy balance basically has the same form as that used by Pollard et al. (1973) except for the geostrophic pressure gradient term which does not enter their wind-mixed layer problem. The balance implies that the role of turbulence is to change the potential energy and that the turbulent kinetic energy, the dissipation and the surplus of the power lost to bottom friction acting on the real velocity other than the vertically averaged velocity, which are omitted here, reach a balance themselves.

2.2.3. Introduction of the velocity profile parameter (α')

Examining Eq. (2.19) the velocity components appear in vertically averaged form as in the momentum equations except for the first term on the left hand side. It is needed to express this integral in terms of vertical means. Referring to Fig. 2.3, the deviations of the velocity components from their vertical means are

$$\Delta u = u - \bar{u} \tag{2.20a}$$

$$\Delta v = v - \bar{v}. \tag{2.20b}$$

Substituting Eqs. (2.20a) and (2.20b) in Eq. (2.19) and using Eqs. (2.7) and (2.8) gives

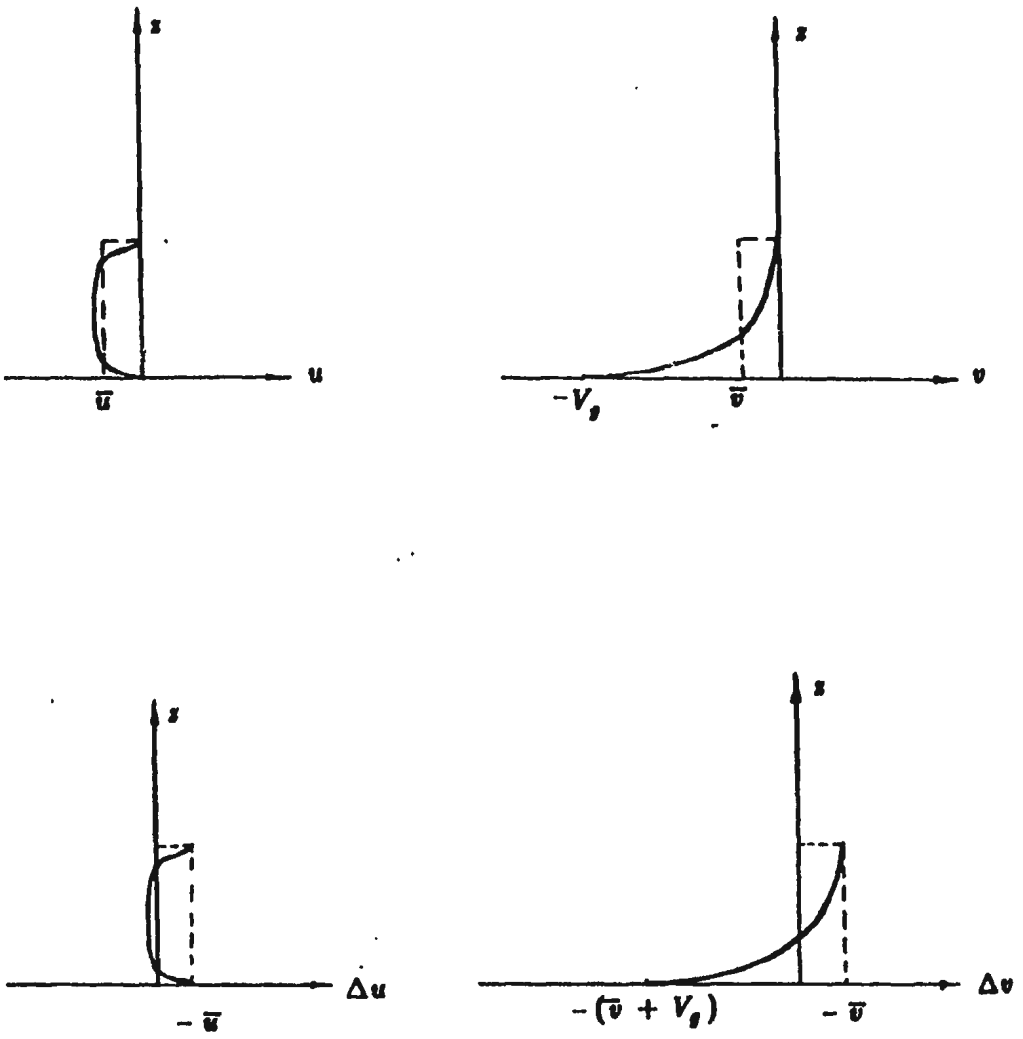

Figure 2.3. Schematic profiles of u and v, the components of velocity less geostrophic velocity, and the differences Δu and Δv from the vertical means $\bar{u}$ and $\bar{v}$ during mixed layer growth.

$$\frac{\rho_o}{2}\frac{\partial}{\partial t}\left[\int_0^h[(\Delta u)^2+(\Delta v)^2]dz\right]+\frac{\rho_o}{2}\left[\frac{1}{2}N_o{}^2h^2-(\bar{u}^2+\bar{v}^2)\right]\frac{\partial h}{\partial t}=0 \qquad (2.21)$$

where it is assumed that the speed at the interface is equal to the geostrophic speed. Eq. (2.21) is identical to the equivalent relation obtained by Pollard et al. (1973), except for the additional term involving departures from the vertically averaged velocity.

The integral in Equation (2.21) can be expressed in terms of bulk parameters by using dimensional analysis and a similarity argument. During the growth of bottom boundary layer the velocity profile varies as thickness increases. The velocity profile also depends on z, N_o, f and u_*. Thus

$$\Delta u = g(h, z, f, N_o, u_*)$$
$$\Delta v = f(h, z, f, N_o, u_*)$$

where the dependence on V_g is incorporated into the friction velocity u_* (Weatherly et al., 1980 and Bird ,1981). The dimensional analysis yields

$$\frac{\Delta u}{u_*} = G\left(\frac{z}{h}, \frac{N_o}{f}, \frac{hf}{u_*}\right)$$
$$\frac{\Delta v}{u_*} = F\left(\frac{z}{h}, \frac{N_o}{f}, \frac{hf}{u_*}\right),$$

If it is furthermore assumed that the velocity profiles remain self-similar during growth, then F and G cannot depend on the thickness, and therefore not on $\frac{hf}{u_*}$. Therefore we may write

$$\int_0^h[(\Delta u)^2+(\Delta v)^2]dz = u_*{}^2h\int_0^1(G^2+F^2)d\zeta_1 = \alpha' u_*{}^2h \qquad (2.22a)$$

where $\varsigma_1 = z/h$. The dependence on $\frac{z}{h}$ has been lost as a result of the integration with respect to ς_1 from 0 to 1, and thus

$$\alpha' = \int_0^1 (G^2 + F^2) d\varsigma_1$$

can only depend on $\frac{N_o}{f}$. From Eq. (2.22a) it is deduced that when V_g is constant (so that u_* is constant)

$$\frac{\partial}{\partial t} \int_0^h [(\Delta u)^2 + (\Delta v)^2] dz = \alpha' u_*^2 \frac{\partial h}{\partial t} \tag{2.22b}$$

for a given value of $\frac{N_o}{f}$.

Krauss (1973) has also equated the vertical integrals of the products of the deviations of velocity components from their vertical means to stresses, in his case to horizontal shear stresses. However, Krauss was dealing with the vertically integrated non-linear momentum equations. His approach is therefore fundamentally different, because here the momentum equations are linearized and the products $(\Delta u)^2$ and $(\Delta v)^2$ therefore appear only in the energy equation.

After substituting Eq. (2.22b) into Eq. (2.21) the energy equation becomes

$$[\alpha' u_*^2 + \frac{1}{2} N_o^2 h^2 - (\bar{u}^2 + \bar{v}^2)] \frac{\partial h}{\partial t} = 0$$

which has two possible solutions:

$$\alpha' u_*^2 + \frac{1}{2} N_o^2 h^2 - (\bar{u}^2 + \bar{v}^2) = 0 \tag{2.23a}$$

and

$$\frac{\partial h}{\partial t} = 0. \tag{2.23b}$$

Because when $t = 0$, $h = 0$, Eq. (2.23b) only gives the trivial solution $h \equiv 0$ at all later times: that is there is no bottom mixed layer formed. Therefore the solution Eq. (2.23b) is meaningless. Only Eq. (2.23a) is an acceptable solution and represents the energy balance.

Rewriting Eq. (2.23a) in the form

$$\frac{1}{2}N_o{}^2h^2 = (\overline{u}^2 + \overline{v}^2) - \alpha' u_*{}^2,$$

it can be seen that the left-hand side is the change in potential energy due to mixing, and therefore the right-hand side defines the kinetic energy available for mixing. It can also be seen that there is less kinetic energy available for mixing when considering the velocity profile ($\alpha' \neq 0$) than in the slab model. Noting from Eqs. (2.22a) and (2.20) that

$$\alpha' u_*{}^2 = \overline{U^2} - \overline{U}^2 \tag{2.24}$$

where U is the magnitude of $\vec{U}$, it becomes clear that the physical reason for this is the fact that the actual total mean kinetic energy in the boundary layer is greater than the squared mean velocity.

Equation (2.23a) is a central result in the present development. If the distribution of velocity in the vertical direction were uniform, as it would be in the usual slab model, α' would vanish and Eq. (2.23a) would become

$$\frac{N_o{}^2h^2}{2} = \overline{u}^2 + \overline{v}^2. \tag{2.25}$$

This specifies that for a growing boundary layer the overall Richardson number

R_* is unity, since R_* is given by (Turner, 1973)

$$R_* = \frac{g\, h\, \Delta\rho/\rho_*}{\overline{u}^2 + \overline{v}^2} = \frac{N_*^2 h^2/2}{\overline{u}^2 + \overline{v}^2}. \tag{2.26}$$

Here $\Delta\rho = \rho' - \rho_*(h)$, the density difference across the interface. Eq. (2.25) is the marginally stable condition used by Pollard et al. (1973) and Thompson (1973).

The velocity is not vertically uniform however (Fig. 2.1). It is therefore interesting to explore the consequences of taking $\alpha' \neq 0$. This is done in the next section.

2.3. Analytic Solution

In the limit $t \to \infty$ for V_g = constant, a steady state solution is sought and the time-dependent terms in Eqs. (2.7) and (2.8) are therefore dropped. Then the governing equations become

$$f\, h\, \bar{v} = \frac{1}{\rho_o} \tau_b{}^x \tag{2.27a}$$

$$f\, h\, \bar{u} = -\frac{1}{\rho_o} \tau_b{}^y \tag{2.27b}$$

$$\alpha' u_*{}^2 + \frac{1}{2} N_o{}^2 h^2 - (\bar{u}^2 + \bar{v}^2) = 0. \tag{2.27c}$$

Squaring Eqs. (2.27a) and (2.27b) and using

$$\frac{1}{\rho_o} | \tau_b | = u_*{}^2,$$

Eq. (2.27c) can be rewritten as

$$\frac{1}{2} f^2 N_o{}^2 h^4 + \alpha' u_*{}^2 f^2 h^2 - u_*{}^4 = 0. \tag{2.28}$$

Solving Eq. (2.28) for h^2 and taking the positive root, eventually yields

$$h = \sqrt{\frac{2}{\alpha'}} \frac{u_*/f}{\left[\sqrt{1 + \frac{2}{\alpha'^2} \frac{N_o{}^2}{f^2}} + 1\right]^{\frac{1}{2}}}. \tag{2.29}$$

Expressions for the veering angle and velocity components $(\bar{u}, \bar{v})$ are also needed. The veering angle is defined by (see Fig. 2.4)

$$\tan\alpha = \frac{\bar{u}}{\bar{v} + V_g} \tag{2.30}$$

so that in the northern hemisphere $\alpha < 0$ since $\bar{u} < 0$: that is, the transverse flow in the mixed layer is directed to the left of the interior geostrophic flow (Fig. 2.4).

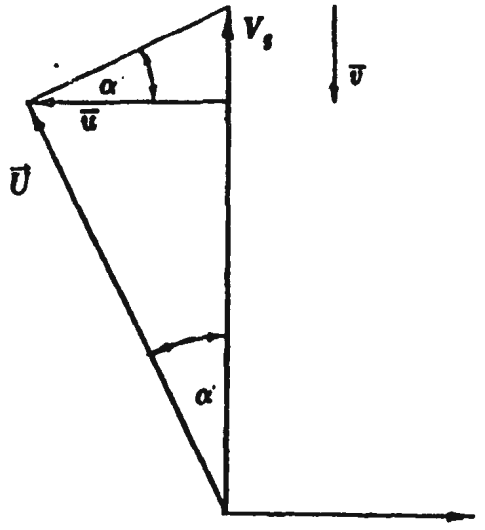

Figure 2.4. Velocity components and veering angle ($\alpha < 0$ as shown).

The bottom stress components may be written as:

$$\tau_b^{\,x} = \rho_o u_*^2 \sin\alpha \tag{2.31a}$$

$$\tau_b^{\,y} = \rho_o u_*^2 \cos\alpha \tag{2.31b}$$

which when substituted in Eqs. (2.27 a and b) yields an expression for $\tan\alpha$ in terms of $\bar{u}$ and $\bar{v}$ alone:

$$\tan\alpha = -\frac{\bar{v}}{\bar{u}} \tag{2.32}$$

as shown in Fig. 2.4.

Now, since

$$\bar{u} = \bar{U}\cos\alpha \tag{2.33}$$

where $\bar{U}^2 = \bar{u}^2 + (\bar{v} + V_g)^2$ as before, both Eqs. (2.27a) and (2.27b), using Eqs. (2.30), (2.31) and (2.32), reduce to

$$\bar{U}\tan\alpha = -\frac{u_*^2}{fh}. \tag{2.34}$$

$\bar{U}$ can be expressed in terms of u_* by defining a bottom drag coefficient C_d such that

$$u_*^2 = C_d \bar{U}^2. \tag{2.35}$$

This was also the form for bottom stress used by Thompson (1973) in his slab model of the bottom mixed layer. Then, using Eq. (2.29), Eq. (2.34) becomes

$$\tan\alpha = -\frac{\sqrt{a'C_d/2}}{\Phi} \tag{2.36}$$

where Φ is

$$\Phi = \frac{1}{\left[\sqrt{1 + \frac{2}{a'^2}\frac{N_o^2}{f^2}} + 1\right]^{\frac{1}{2}}}. \tag{2.37}$$

Using Eqs. (2.35) and (2.36), Eq. (2.33) becomes

$$\bar{u} = -\sqrt{\frac{\alpha'}{2\Phi^2 + \alpha' C_d}}\, u_* \tag{2.38}$$

and thus from Eq. (2.32)

$$\bar{v} = -\frac{\alpha'\sqrt{C_d}}{\Phi\sqrt{4\Phi^2 + 2\alpha' C_d}}\, u_* \tag{2.39}$$

Finally, Equation (2.35) can be shown, by equating Eq. (2.30) and Eq. (2.32), to reduce to:

$$u_* = \sqrt{\frac{C_d}{1 + (\alpha' C_d)/(2\Phi^2)}}\, V_g$$

$$= \left[\frac{C_d}{1 + \frac{C_d}{2}(\alpha' + \sqrt{\alpha'^2 + \frac{2N_o^2}{f^2}})}\right]^{\frac{1}{2}} V_g . \tag{2.40}$$

The model therefore yields an explicit relation between u_* and V_g (This relation can also be obtained by recognizing from Fig. 2.4 that $\bar{U} = V_g \cos\alpha$.)

Finally it is worth noting with respect to Eq. (2.36) that α is non-zero when α' is zero. Using Eq. (2.37) it is seen that

$$\tan\alpha = -\sqrt{C_d/2}\sqrt{\alpha' + \sqrt{\alpha'^2 + \frac{2N_o^2}{f^2}}} \tag{2.41}$$

so that in fact when $\alpha' = 0$

$$\tan\alpha = -\sqrt{\frac{C_d N_o}{\sqrt{2} f}}$$

which is the result obtained by Thompson (1973).

2.4. Comparisons with Previous Results

If the velocity distribution were uniform as in the slab model, then $\alpha' = 0$ and Eq. (2.29) reduces to Eq. (1.3), the result obtained by Thompson (1973). When $\frac{N_e}{f}$ is large, Eq. (2.29) also reduces to Thompson's result. Equation (2.29) represents an improvement over Thompson's result in the sense that by including the velocity profile parameter α', the mixed layer thickness does not become infinite as $\frac{N_e}{f} \to 0$. Equation (2.29) is also comparable in form to Eq. (1.4) obtained by Weatherly and Martin (1978), although the two results are clearly not identical.

It was argued earlier that α' should depend only on $\frac{N_e}{f}$. Furthermore, it can be seen that Eq. (2.29) is consistent with Eq. (1.2), the expected form, if α' is a function of $\frac{N_e}{f}$. We now estimate the range of possible values for α' when the mixed layer is fully developed.

For the neutrally stratified case $\frac{N_e}{f} = 0$, and $A\,\Phi = 0.4$ (Eqs. 1.1 and 1.2). Using this in Eq. (1.2), and equating Eqs. (1.2) and (2.29) yields

$$\alpha' = 6.3. \tag{2.42}$$

Substituting this value of α' into Eq. (2.29) gives

$$h = 0.57 \frac{u_* / f}{\left[1 + \sqrt{1 + 0.051 \frac{N_e^2}{f^2}}\right]^{\frac{1}{2}}} \tag{2.43}$$

An alternate value for α' can be obtained by setting Eq. (2.29) equal to Weatherly and Martin's formula Eq. (1.4) when $N_o = 0$. This gives

$$\alpha' = 0.59 \tag{2.44}$$

and Eq. (2.29) becomes

$$h = 1.8 \frac{u_o / f}{\left[1 + \sqrt{1 + 5.7 \frac{N_o^2}{f^2}}\right]^{\frac{1}{2}}}. \tag{2.45}$$

Now, how should the value of α' vary with the buoyancy frequency? This can be investigated by equating the analytic solution of thickness obtained here to Thompson's result Eq. (1.3) or Weatherly and Martin's result Eq. (1.4). In order to be consistent with both Eq. (1.3) and Eq. (1.4) let Eq. (2.29) be

$$\sqrt{\frac{2}{\alpha'}} \frac{u_o / f}{\sqrt{1 + \sqrt{1 + \frac{2}{\alpha'^2} \frac{N_o^2}{f^2}}}} = \frac{2^{\frac{1}{4}} \frac{u_o}{f}}{\left[1 + \frac{N_o^2}{f^2}\right]^{\frac{1}{4}}} \tag{2.46a}$$

replacing the factor 1.3 in Eq. (1.4) by $2^{\frac{1}{4}} \cong 1.2$. Solving Eq. (2.46a) for α' yields

$$\alpha' = \frac{1}{\sqrt{2\left(1 + \frac{N_o^2}{f^2}\right)}} \tag{2.46b}$$

which is plotted in Fig. 2.5. Eq. (2.46b) shows that the value of α' will decrease when the stratification increases and eventually tends to zero. However at large $\frac{N_o}{f}$, it is readily shown that the expression (2.29) for h becomes independent of

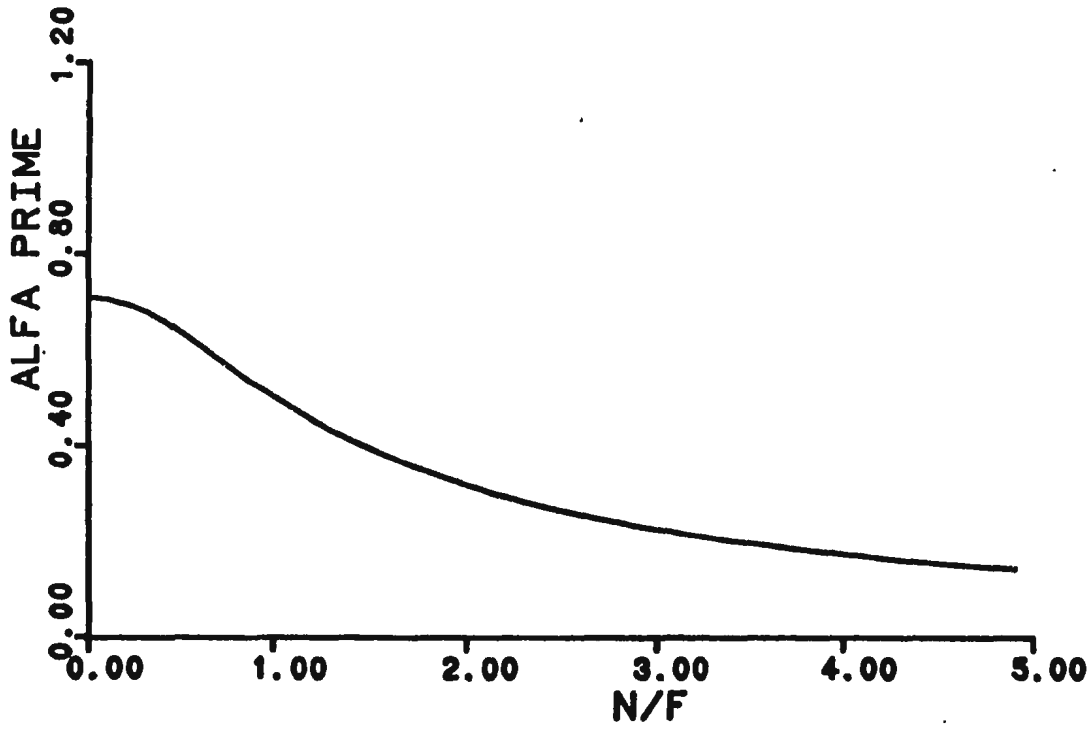

Figure 2.5. Variation of α' with $\frac{N_e}{f}$ according to Eq. (2.46b).

α' since

$$\frac{2}{\alpha'^2}\frac{N_o^2}{f^2} \gg 1$$

which leads to Thompson's result Eq. (1.3) with an error less than 6% when $\frac{N_o}{f} > 2$. Therefore when $\frac{N_o}{f}$ is larger than 2 the thickness is almost independent of the value of α'. Within the range of $\frac{N_o}{f}$ from 0 to 2 the effective values of α' change from 0.7 to 0.3. This variation of α' is not large.

Equations (2.43), (2.45) and (2.29) with α' given by Eq. (2.46b) are compared with Weatherly and Martin's formula (Eq. 1.4) in Figures 2.6 and 2.7. The numerical values are those obtained by Weatherly and Martin (1978), and were supplied by Weatherly (Table 2.1). Fig. 2.6 shows that Eq. (2.45) gives results which are almost the same as Weatherly and Martin's result, Equation (1.4), in spite of the fact that the two equations are clearly different. This can be understood by examining Table 2.1. It is seen that the values of $\frac{N_o}{f}$ used by Weatherly and Martin are either zero or much larger than one. When $\frac{N_o}{f} \gg 1$, Eqs. (2.45) and (1.4) are nearly identical. That is, Eq. (2.45) reduces to Eq. (1.3):

$$h = 1.2\frac{u_o}{\sqrt{N_o f}},$$

while Eq. (1.4) becomes

$$h = 1.3\frac{u_o}{\sqrt{N_o f}}.$$

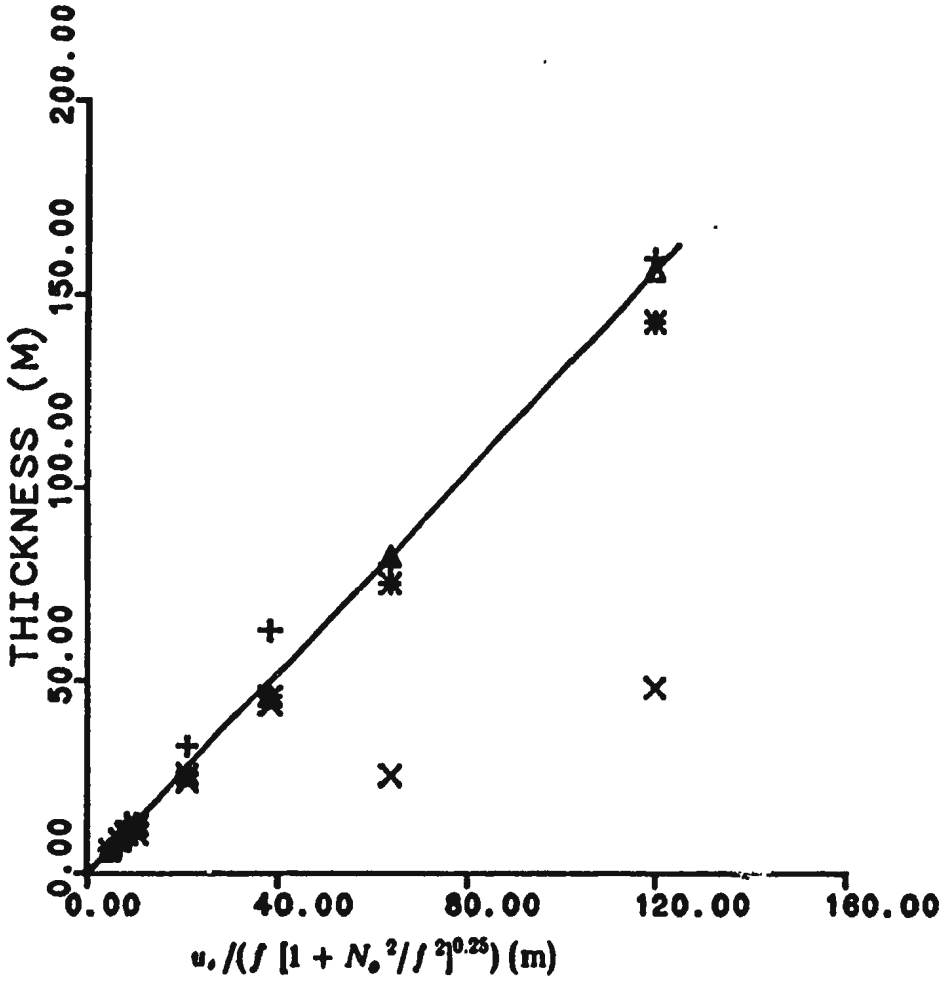

Figure 2.6. Bottom mixed layer thicknesses plotted against $u_*/(f\,[1 + N_e^2/f^2]^{0.25})$.

The symbols:

+ stands for the numerical results from the Level II turbulent closure model given by Weatherly and Martin (1978),

x for Eq. (2.43),

Δ for Eq. (2.45), and

✱ fro Eq. (2.29) when α' is Eq. (2.46b).

The straight line is Eq. (1.4).

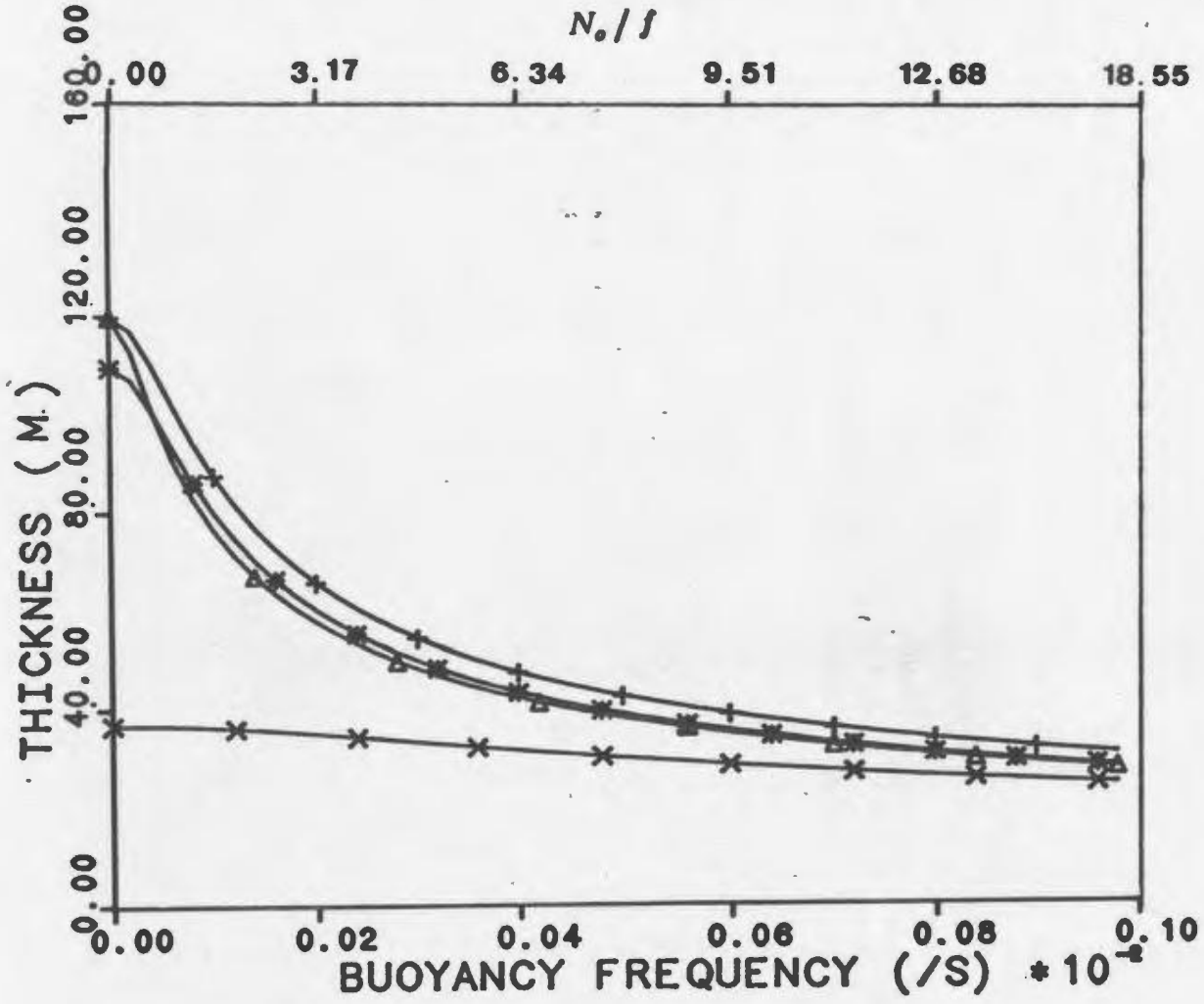

Figure 2.7. The thicknesses plotted against buoyancy frequency N_o for $u_* = 0.58$ cm/s and $f = 0.63 \times 10^{-4}$ /s. The symbols:

+ stands for Eq. (1.4) (Weatherly and Martin, 1978),

x for Eq. (2.43),

Δ for Eq. (2.45), and

✱ fro Eq. (2.29) when α' is Eq. (2.46b).

$h_{q=0}$ (m)	f $(\times 10^{-4})$/s	V_g cm/s	N_o $(\times 10^{-3}$ /s)	u_* $(\times 10^{-3})$cm/s	$\frac{N_o}{f}$
159	.63	20	0	7.56	0
80	.63	15	0	4.05	0
63	.71	40	3.	17.8	42.3
33	.63	20	1.9	7.45	30.16
13	.63	20	12.8	7.68	203.17
7	.63	15	12.8	5.97	203.17
6.2	.63	10	12.8	4.46	203.17
12.8	.68	5.	.7	2.29	10.29

Table 2.1. Values for $h_{q=0}$, f, V_g, N_o provided by Weatherly, corresponding to Fig. 8 in Weatherly and Martin (1978). The values for u_* are evaluated from Fig. 8 of their paper. The thickness $h_{q=0}$ is defined as the height at which the turbulent kinetic energy goes to zero, where q is the turbulent kinetic energy.

When $\frac{N_o}{f} = 0$ Eqs. (2.45) and (1.4) are identical, because of the choice $\alpha' = 0.59$.

Even at intermediate values of $\frac{N_o}{f}$, however, Eq. (2.45) is not very much different from Weatherly and Martin's result. This is demonstrated in Figure 2.7, where the thicknesses are plotted as a function of N_o and $\frac{N_o}{f}$ for values of u_* (0.58 cm/s) and f (0.63×10^{-4} /s) used by Weatherly and Martin (1978). Figs. 2.6 and 2.7 show that the thickness given by Eq. (2.45) with $\alpha' = 0.59$ is very close to the thickness with α' given by Eq. (2.43b).

Figure 2.7 also shows a comparison between Eqs. (2.43) and (1.4). When $\frac{N_o}{f} \gg 1$, Eq. (2.43) also tends to Eq. (1.3), explaining the good agreement between Eq. (2.43) and Eq. (1.4) at large $\frac{N_o}{f}$. But the difference between these two equations is very large when $\frac{N_o}{f} \ll 1$. The reason for this is that the thickness calculated from Eq. (1.4) when $\frac{N_o}{f} = 0$ is $h = 1.3\frac{u_*}{f}$ which is three times greater than the thickness computed from Eq. (2.43) with $\frac{N_o}{f} = 0$, which is then the same as Eq. (1.1). Weatherly and Martin (1978) attributed this difference to their use of $q = 0$ to define the thickness h.

It is concluded that the predicted mixed layer thickness depends critically on the choice of α' only when $\frac{N_o}{f}$ is of order unity or smaller, consistent with the

fact that the vertically-integrated model tends to Thompson's model in the limit of large $\frac{N_o}{f}$. This could imply that the shape of the velocity profile is less critical to the dynamics of bottom mixed layers when $\frac{N_o}{f}$ is large, which would be consistent with the observation (Weatherly and Van Leer) that for $\frac{N_o}{f}$ large, most of the veering occurs in the interfacial region, and the velocity within the mixed layer is more uniform with height. However, the definitions of bottom boundary layer thickness based on turbulence intensity on the one hand, and velocity on the other, yield very different thickness estimates when $\frac{N_o}{f}$ is small, and this appears to account for the largest differences in Figs. 2.6 and 2.7.

2.5. Direct Estimates of α'

The velocity profile parameter α' can be estimated directly from measured or theoretical velocity profiles using Eq. (2.24). Note that different definitions of thickness will yield different values of α'. As an example, consider the speed profile obtained by Weatherly and Martin (1978) using the Level II turbulent closure scheme for a horizontal bottom for $\frac{N_o}{f} = 0$, $V_g = 15$ cm/s and $u_* = 0.58$ cm/s (Fig. 6 in their paper). This profile is replotted in Fig. 2.8a, and the profile of U^2 in Fig. 2.8b. Computed values of $\bar{U}$, $\overline{U^2}$ and α' based on Fig. 2.8 and three definitions of thickness are given in Table 2.2. From this Table it can be seen that all three values of α' are in the range spanned by Eq. (2.43) ($\alpha' = 6.3$) and Eq. (2.45) ($\alpha' = 0.59$). Furthermore, the results in Table 2.2 exhibit the proper trend. That is, α' is smaller when the thickness is defined as $h_{q=0}$, as in Eq. (2.44); whereas α' is larger when the thickness is defined by Eq. (1.1) or by $U = 0.999 V_g$, as in Eq. (2.42).

2.6. Richardson Number Dependence

The magnitude of the overall Richardson number Eq. (2.26) is, using Eq. (2.23a)

$$R_o^{-1} = 1 + \frac{\alpha'^2}{N_o^2/f^2}\left[1 + \sqrt{1 + \frac{2}{\alpha'^2}\frac{N_o^2}{f^2}}\right]. \tag{2.47}$$

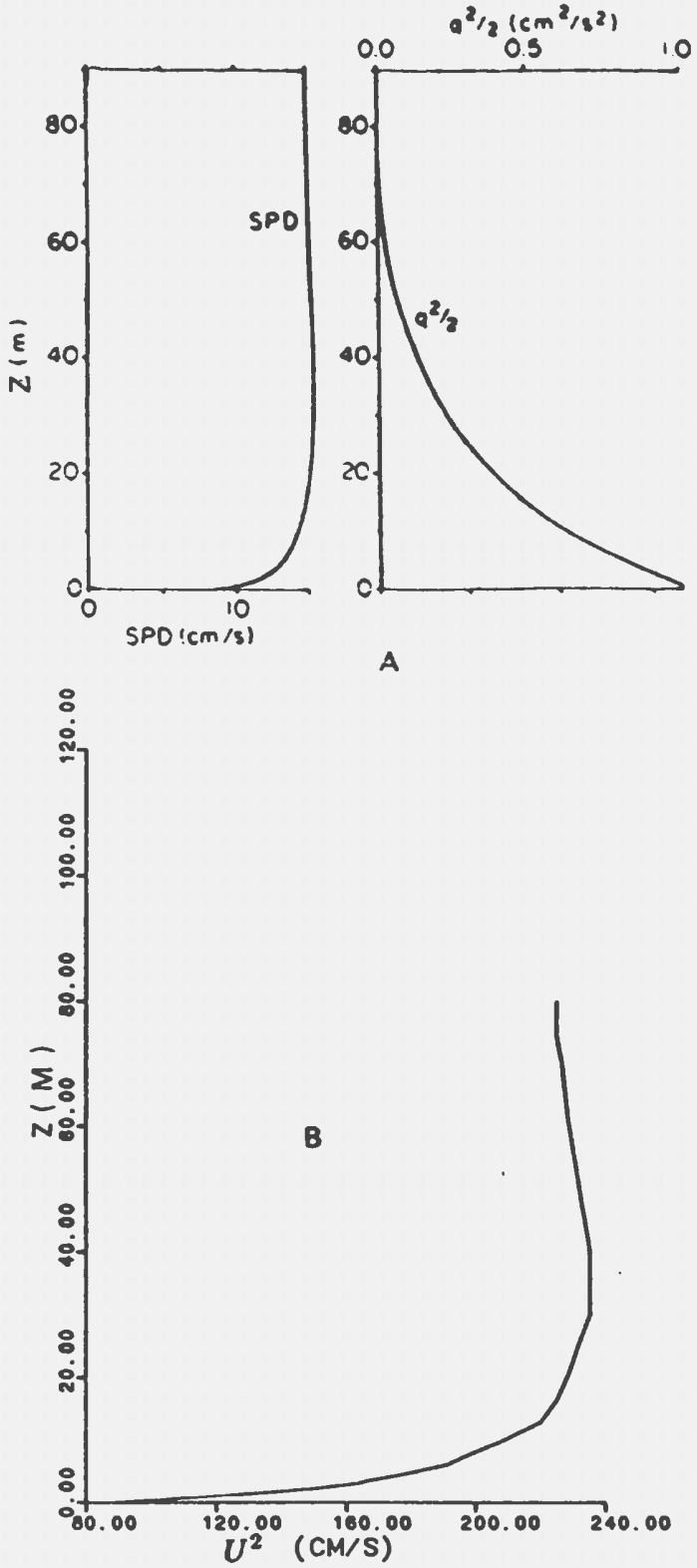

Figure 2.8. (A) Speed and turbulent kinetic energy ($\frac{1}{2}q^2$) profiles given in Fig. 6 of Weatherly and Martin's paper (1978) and (B) the profile of U^2.

Definition	h (m)	$\bar{U}$ (cm/s)	$\overline{U^2}$ (cm /s)^2	α'
1	80	14.87	222.0	2.2
2	36.83	14.54	212.9	4.2
3	16.15	13.67	188.9	5.6

Table 2.2. Comparisons of average speed $\bar{U}$, average speed squared $\overline{U^2}$ and the values of α' for different definitions of thickness. In Definition 1 the thickness is defined as the height at which the turbulent kinetic energy goes to zero. In Definition 2 the thickness is calculated based on Eq. (1.1). In Definition 3 the thickness is defined as the height where the speed is 99.9% of the geostrophic speed.

For $\frac{N_e}{f} \ll 1$, it is seen that

$$R_e = \frac{N_e^2/f^2}{2\alpha'^2}$$

which is much less than unity, implying supercritical flow. For $\frac{N_e}{f} \gg 1$, Eq. (2.47) shows that $R_e \sim 1$, which is consistent with the marginally stable condition used by Pollard et al. (1973) and Thompson (1973).

However, because most of the shear at the interface between the boundary layer and the interior is due to the transverse component of velocity $\bar{v}$, it is convenient to define the overall Richardson number R'_e due to $\bar{v}$ alone as pointed out by Weatherly and Martin (1978). From Eqs. (2.23a), (2.32) and (2.34) it can be shown that

$$[R'_e]^{-1} = \frac{\bar{v}^2}{\frac{1}{2}N_e^2 h^2}$$

$$= \frac{[1 + \sqrt{1 + \frac{2N_e^2}{\alpha'^2 f^2}}]}{\frac{N_e^2}{\alpha'^2 f^2}[\alpha' C_d + 2/(1 + \sqrt{1 + \frac{2N_e^2}{\alpha'^2 f^2}})]} \tag{2.48}$$

Therefore for $\frac{N_e}{f} \ll 1$, $R'_e \ll 1$ as was the case for R_e. For $\frac{N_e}{f} \gg 1$, Eq. (2.48) becomes

$$R'^{-1}_e = \frac{\sqrt{2}}{\frac{C_d N_e}{f} + \sqrt{2}}, \tag{2.49}$$

and thus $R'_e > 1$. By using this Richardson number definition it is seen that for

$N_o/f \ll 1$ the transverse flow is supercritical, while for $N_o/f \gg 1$ it is subcritical.

CHAPTER 3

THE SLOPING FLAT BOTTOM CASE

For a sloping flat bottom it is more convenient to set up the coordinate system (x, y, z) with the z-axis perpendicular to the sea bottom, the so-called bottom coordinate system, in place of the coordinate system (x', y', z') in which the z'-axis is vertical (Fig. 3.1). It is assumed that the bottom slope β is small, the velocity V_g of the mean flow in the interior of the ocean is in the y-direction parallel to the isobaths, and $\rho_o = \rho_o(z')$, so that the density gradient in the interior is solely vertical and constant. Clearly,

$$x' = x\cos\beta - z\sin\beta \tag{3.1}$$

$$y' = y \tag{3.2}$$

$$z' = x\sin\beta + z\cos\beta \tag{3.3}$$

and

$$\frac{\partial \rho_o}{\partial z'} = 0.$$

Thus

$$\rho_{oz} = \beta\rho_{oz} \tag{3.4}$$

when β is small.

3.1. Momentum Equations

The same assumptions are made here as in Chapter 2 for a horizontal bottom. It can then be shown that in the bottom coordinate system the momentum equations in the interior of the ocean are

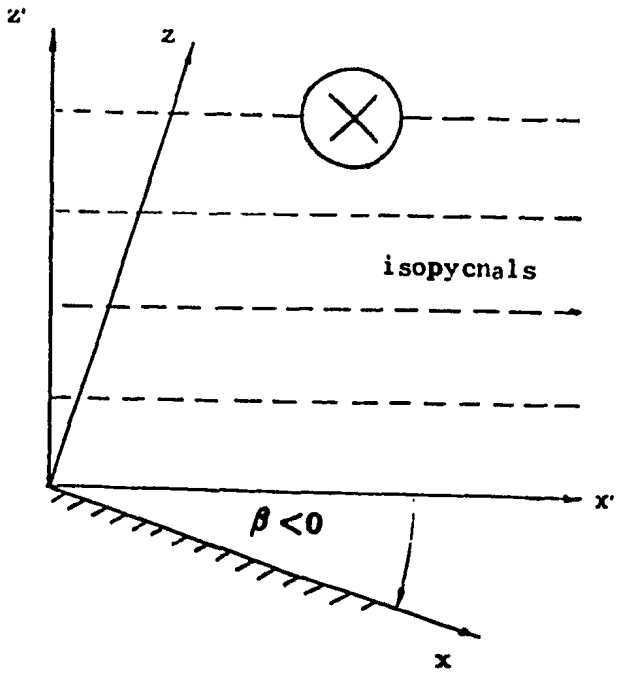

Figure 3.1. A sketch of a sloping flat bottom with horizontal isopycnals. The mean flow in the interior is directed into the page, as indicated by the symbol ⊗.

$$-fV_g = -\frac{1}{\rho_o(x,z)}\frac{\partial P_o}{\partial x} - g\beta \tag{3.5}$$

$$0 = -\frac{1}{\rho_o}\frac{\partial P_o}{\partial z} - g. \tag{3.6}$$

Based on the observations made by Van Leer and Ross (1979), Weatherly and Van Leer (1977), Bird et al. (1982), Armi (1978), and Dewey (1987). the density in the bottom boundary layer on either a sloping sea door or a horizontal flat sea floor is quite uniform. Therefore it is assumed that the density ρ' is independent of z during the growth of the layer because of mixing. Since all quantities are independent of y,

$$\rho' = \rho'(x, t). \tag{3.7}$$

Let

$$\rho' = [\rho_o(x,z) + \rho''(z,t)]_i + \epsilon(t). \tag{3.8}$$

In Eq. (3.8) the density ρ' in the mixed layer has been separated into two parts: the first part $[\rho_o(x,z) + \rho'']$ is caused by local mixing in the z-direction; the second part $\epsilon(t)$ is the advective contribution due to Ekman transport.

It is important to note that in this problem both N_o and V_g are independent of x. It is therefore reasonable to expect that the mixed layer thickness will also be independent of x at any instant of time. In particular during initial growth before ϵ becomes appreciable, the difference in density across the interface between the mixed layer and the overlying fluid should then also be independent of x. This further implies that $\bar{w}$ should be independent of x, and hence at later times that ϵ will remain independent of x.

As in the case of a horizontal flat bottom, at any time the first part of Eq. (3.8) should be equal to the density at $z = \frac{h}{2}$ before mixed layer formation, i. e.

$$\rho_o(x, z) + \rho''(x, t) = \rho_o(x, \frac{h}{2}) = \rho_o(x, 0) + \rho_{oz}\frac{h}{2} \tag{3.9}$$

since

$$\rho_o(x, z) = \rho_{oz}z + \rho_o(x, 0) = \rho_o(x, h) - \rho_z(h - z). \tag{3.10}$$

Therefore

$$\rho' = \rho_o(x, \frac{h}{2}) + \epsilon(t) = \rho_o(x, 0) + \rho_{oz}\frac{h}{2} + \epsilon(t). \tag{3.11}$$

From Eqs. (3.9) and (3.10)

$$\rho'' = \rho_{oz}(\frac{h}{2} - z). \tag{3.12}$$

Obviously

$$\int_0^h \rho'' dz = 0. \tag{3.13}$$

From Eq. (3.8) and the hydrostatic condition, the pressure P' in the boundary layer can be shown to be of the form

$$P' = P_o(x, z) + P''(x, t) \tag{3.14}$$

where P'' represents the perturbation to the geostrophic pressure field induced by mixing and advection. After making use of Eqs. (3.5)-(3.6), (3.8), and (3.13)-(3.14), and the assumptions made in Chapter 2 for deriving the momentum equations, it can be shown that the momentum equations in the boundary layer above a sloping bottom are

$$\frac{\partial u}{\partial t} - fv = -\frac{\rho''}{\rho_o}g\beta - \frac{\epsilon g\beta}{\rho_o} + \frac{1}{\rho_o}\frac{\partial \tau^x}{\partial z} \tag{3.15}$$

$$\frac{\partial v}{\partial t} + fu = \frac{1}{\rho_o}\frac{\partial \tau^y}{\partial z} \tag{3.16}$$

$$0 = -\frac{\partial P''}{\partial z} - g\rho'' - \epsilon g. \tag{3.17}$$

of which Eqs. (3.15) and (3.16) are the same equations as used by Weatherly and Martin (1978).

3.2. Mass and Volume Conservation.

The continuity equation is the same as Eq. (2.3). Equations (2.4)-(2.6) are also valid for the sloping bottom case because both h and $\bar{u}$ are constant in the down-slope direction as discussed previously.

The mass conservation equation is

$$\frac{\partial \rho'}{\partial t} + \frac{\partial}{\partial z}(\rho' u) + \frac{\partial}{\partial z}(\rho' w) = -\frac{\partial}{\partial z}<\hat{\rho}\hat{w}>, \tag{3.18}$$

where the turbulent mass flux is assumed to vary mainly in the direction perpendicular to the bottom. The turbulent mass flux gradients in the x and y directions are ignored, because the scale of the layer in the direction perpendicular to the bottom is much smaller than that in the direction parallel to the bottom. Substituting Eqs. (3.7) and (2.3) into Eq. (3.18) yields

$$\frac{\partial \rho'}{\partial t} + u\frac{\partial \rho'}{\partial x} = -\frac{\partial}{\partial z}<\hat{\rho}\hat{w}> \tag{3.19}$$

where, in contrast to the horizontal bottom case, a second term appears on the left-hand side due to the advection of mass.

3.3. Vertically-averaged Equations

Now integrating Eqs. (3.15) and (3.16) in the z-direction yields

$$\frac{\partial}{\partial t}(\bar{u}h) - f\bar{v}h = -\frac{1}{\rho_o}\tau_b{}^x + \frac{1}{\rho_o}\tau_i{}^x + u(h)h_t - \beta\frac{g}{\rho_o}\epsilon h \tag{3.20}$$

$$\frac{\partial}{\partial t}(\bar{v}h) + f\bar{u}h = -\frac{1}{\rho_o}\tau_b{}^y + \frac{1}{\rho_o}\tau_i{}^y + v(h)h_t . \tag{3.21}$$

Again by making use of the assumption Eq. (2.9) the momentum equations (3.20) and (3.21) become

$$\frac{\partial}{\partial t}(\bar{u}h) - f\bar{v}h = -\frac{1}{\rho_o}\tau_b{}^x - \beta\frac{g}{\rho_o}\epsilon h \tag{3.22}$$

$$\frac{\partial}{\partial t}(\bar{v}h) + f\bar{u}h = -\frac{1}{\rho_o}\tau_b{}^y \tag{3.23}$$

Integrating the mass conservation equation (3.19) yields

$$h\frac{\partial\rho'}{\partial t} + h\bar{u}\frac{\partial\rho'}{\partial x} = -<\hat{\rho}\hat{w}>|_{z=h} . \tag{3.24}$$

The turbulent mass flux at the upper interface can be written in terms of an entrainment velocity:

$$-<\hat{\rho}\hat{w}>|_{z=h} = [\rho' - \rho_o(x,h)]\, w_e . \tag{3.25}$$

This relation was also used by Geisler and Kraus (1969). Equation (3.11) can be written in two forms:

$$\rho' = \rho_o(x,0) + \rho_{oz}\frac{h}{2} + \epsilon(t) = \rho_o(x,h) - \rho_{oz}\frac{h}{2} + \epsilon(t) \tag{3.26}$$

Therefore

$$\frac{\partial\rho'}{\partial t} = \frac{\rho_{oz}}{2}\frac{\partial h}{\partial t} + \frac{\partial\epsilon}{\partial t}. \tag{3.27}$$

From Eqs. (3.8) and (3.4) it is seen that

$$\frac{\partial \rho'}{\partial z} = \frac{\partial \rho_o}{\partial z} = \beta \rho_{oz}. \tag{3.28}$$

Substituting Eqs. (2.6), (3.25), (3.26), (3.27) and (3.28) into Eq. (3.24) yields

$$\frac{g}{\rho_o}(h\epsilon)_t = \beta h \bar{u} N_o^2. \tag{3.29}$$

3.4. Energy Equations

Now the energy equation is derived below. In the bottom coordinate system the component forms of the momentum equations are

$$\rho_o \frac{\partial u}{\partial t} + \rho_o \frac{\partial \hat{u}}{\partial t} + \rho_o (u + \hat{u}) \frac{\partial (u + \hat{u})}{\partial x} + \rho_o (v + V_g + \hat{v}) \frac{\partial (u + \hat{u})}{\partial y}$$
$$+ \rho_o (W + \hat{w}) \frac{\partial (u + \hat{u})}{\partial z} = -\frac{\partial P'}{\partial x} - \frac{\partial \hat{p}}{\partial x} - (\rho' + \hat{\rho}) g \beta + \mu \nabla^2 u + \mu \nabla^2 \hat{u}$$
$$- \rho_o (2\vec{\Omega} \times \vec{u})_x \tag{3.30}$$

$$\rho_o \frac{\partial (v + V_g)}{\partial t} + \rho_o \frac{\partial \hat{v}}{\partial t} + \rho_o (u + \hat{u}) \frac{\partial (v + V_g + \hat{v})}{\partial x}$$
$$+ \rho_o (v + V_g + \hat{v}) \frac{\partial (v + V_g + \hat{v})}{\partial y} + \rho_o (W + \hat{w}) \frac{\partial (v + V_g + \hat{v})}{\partial z}$$
$$= -\frac{\partial P'}{\partial y} - \frac{\partial \hat{p}}{\partial y} + \mu \nabla^2 (v + V_g) + \mu \nabla^2 \hat{v} - \rho_o (2\vec{\Omega} \times \vec{u})_y \tag{3.31}$$

$$\rho_o \frac{\partial W}{\partial t} + \rho_o \frac{\partial \hat{w}}{\partial t} + \rho_o (U + \hat{u}) \frac{\partial (W + \hat{w})}{\partial x} + \rho_o (v + V_g + \hat{v}) \frac{\partial (W + \hat{w})}{\partial y}$$
$$+ \rho_o (W + \hat{w}) \frac{\partial (W + \hat{w})}{\partial z} = -\frac{\partial P'}{\partial z} - \frac{\partial \hat{p}}{\partial z} - (\rho' + \hat{\rho}) g + \mu \nabla^2 w$$
$$+ \mu \nabla^2 \hat{w} - \rho_o (2\vec{\Omega} \times \vec{u})_z. \tag{3.32}$$

The dot product of the momentum equation with $\vec{U}$ and time averaging produces (Appendix 1)

$$\frac{\rho_o}{2} \frac{\partial}{\partial t} (u^2 + (v + V_g)^2) = -uP'_x - \rho' g \beta u - \rho_o u \frac{\partial <\hat{u}\hat{w}>}{\partial z}$$
$$- \rho_o (v + V_g) \frac{\partial <\hat{v}\hat{w}>}{\partial z}, \tag{3.33}$$

where as before the viscous terms have been ignored because the Reynolds number is large. Taking the dot product of the momentum equation with $\vec{u}$ and time averaging yields

$$\frac{\rho_o}{2}\frac{\partial<q^2>}{\partial t} + \frac{\rho_o}{2}\frac{\partial}{\partial z}<\hat{w}q^2> = -\frac{\partial}{\partial z}<\hat{w}\hat{p}> - \rho_o<\hat{u}\hat{w}>\frac{\partial u}{\partial z}$$
$$+ \mu\frac{\partial}{\partial z}\left[<\hat{u}(\frac{\partial\hat{u}}{\partial z} + \frac{\partial\hat{w}}{\partial z})> + <\hat{v}(\frac{\partial\hat{v}}{\partial z} + \frac{\partial\hat{w}}{\partial\hat{y}})> + 2<\hat{w}\frac{\partial\hat{w}}{\partial z}>\right]$$
$$- \rho_o<\hat{v}\hat{w}>\frac{\partial(v + V_g)}{\partial z} - <\hat{w}\hat{\rho}>g - \varsigma, \qquad (3.34)$$

where ς is the dissipation term (see Appendix 1) and $q^2 = \hat{u}^2 + \hat{v}^2 + \hat{w}^2$. In Eqs. (3.33) and (3.34) the Boussinesq approximation, $W = 0$, the assumptions $\frac{\partial}{\partial x} \ll \frac{\partial}{\partial z}$ and $\frac{\partial}{\partial y} \ll \frac{\partial}{\partial z}$ have been used. The term $<\hat{\rho}\hat{u}g\beta>$ (assuming it to be much less than $<\hat{\rho}\hat{w}g>$) and the advection of kinetic energy parallel to the bottom have also been ignored. Adding Eq. (3.34) to Eq. (3.33) yields

$$\frac{\rho_o}{2}\frac{\partial}{\partial t}(u^2 + (v + V_g)^2 + <q^2>) + \frac{\rho_o}{2}\frac{\partial}{\partial z}<\hat{w}q^2> + \frac{\partial}{\partial z}<\hat{w}\hat{p}> = -uP'_x$$
$$- \rho' g\beta u + \mu\frac{\partial}{\partial z}\left[<\hat{u}(\frac{\partial\hat{u}}{\partial z} + \frac{\partial\hat{w}}{\partial z})> + <\hat{v}(\frac{\partial\hat{v}}{\partial z} + \frac{\partial\hat{w}}{\partial\hat{y}})> + 2<\hat{w}\frac{\partial\hat{w}}{\partial z}>\right]$$
$$- \rho_o\frac{\partial}{\partial z}[u<\hat{u}\hat{w}> + (v + V_g)<\hat{v}\hat{w}>] - <\hat{w}\hat{\rho}>g - \varsigma. \qquad (3.35)$$

3.5. Vertically-Integrated Energy Equation

It is assumed that Eq. (2.18) is still valid and that $[2\mu<\hat{u}\hat{s}_{xy} + \hat{v}\hat{s}_{yz} + \hat{w}\hat{s}_{xz}> - (\frac{\rho_o}{2}<\hat{w}q^2> + <\hat{p}\hat{w}>)]$ at the bottom and the sea surface can be ignored. By using these two assumptions the integral of Eq. (3.35) from the bottom to the sea surface becomes

$$\frac{\rho_o}{2}\int_0^h \frac{\partial}{\partial t}[u^2 + (v + V_g)^2]dz = -\int_0^h u\frac{\partial P'}{\partial z}dz - \bar{u}\tau_b{}^x - (\bar{v} + V_g)\tau_b{}^y$$

$$- \rho' g \beta \bar{u} h - \int_0^h <\hat{\rho}\hat{w}> g dz \tag{3.36}$$

where $\tau_b{}^x$ and $\tau_b{}^y$ come from Eq. (2.18). It is noticed that the last term but one in Eq. (3.36) is the time rate of change of potential energy due to a vertical displacement when a column of water moves along the slope, and the last term is the time rate of change of potential energy due to mixing. Therefore if these two terms are moved to the left hand side, Eq. (3.36) indicates that the sum of the time rates of change of kinetic and potential energy equals the rate of working by the transverse pressure gradient less the power lost to bottom friction, as in Eq. (2.19) for the horizontal bottom case.

Substituting Eqs. (3.27), (3.28) and (2.20a) into Eq. (3.19) and integrating the resulting equation from 0 to z yields

$$- <\hat{\rho}\hat{w}>|_z = \frac{\rho_{oz}}{2}\frac{\partial h}{\partial t}z + \epsilon_t z + \bar{u}\beta\rho_{oz}z + [\int_0^z \Delta u dz']\beta\rho_{oz}. \tag{3.37}$$

From Eq. (3.29) it is seen that

$$g h \epsilon_t = \rho_o \beta h \bar{u} N_o{}^2 - g \epsilon h_t. \tag{3.38}$$

Using Eq. (3.38) multiplying Eq. (3.37) by g and then integrating yields

$$-\int_0^h <\hat{\rho}\hat{w}> g dz = -[\frac{1}{2}N_o{}^2 h^2 + \frac{g\epsilon h}{\rho_o}]\frac{\rho_o h_t}{2} + \beta g \rho_{oz}\int_0^h [\int_0^z \Delta u dz']dz. \tag{3.39}$$

Substituting Eq. (3.39) into Eq. (3.36) yields

$$\frac{\rho_o}{2}\int_0^h \frac{\partial}{\partial t}[u^2 + (v + V_g)^2]dz = -\bar{u}\tau_b{}^x - (\bar{v} + V_g)\tau_b{}^y - \int_0^h u\frac{\partial P'}{\partial z}dz - \rho' g \beta \bar{u} h$$

$$-\left[\frac{1}{2}N_o^2h^2+\frac{g\epsilon h}{\rho_o}\right]\frac{\rho_o h_t}{2}+\beta g\rho_{oz}\int_0^h\left[\int_0^z\Delta u\,dz'\right]dz. \tag{3.40}$$

As in Chapter 2 the integral on the left-hand side is

$$\int_0^h\frac{\partial}{\partial t}[u^2+(v+V_g)^2]dz=[\bar{u}^2+\bar{v}^2+2\bar{v}V_g]h_t$$

$$+2h\left[\bar{u}\frac{\partial\bar{u}}{\partial t}+\bar{v}\frac{\partial\bar{v}}{\partial t}+V_g\frac{\partial\bar{v}}{\partial t}\right]+\frac{\partial}{\partial t}\int_0^h[(\Delta u)^2+(\Delta v)^2]dz. \tag{3.41}$$

Using Eqs. (2.20a), (3.10), (3.5) and (3.11) it can be deduced that

$$-\int_0^h u\frac{\partial P'}{\partial x}dz=-\bar{u}f V_g h\rho_o+\rho_o(x,0)\bar{u}g\beta h+\frac{1}{2}\bar{u}\rho_{oz}g\beta h^2$$

$$+\int_0^h\rho_{oz}\Delta u\;zg\beta dz. \tag{3.42}$$

Substituting Eqs. (3.11), (3.41) and (3.42) into Eq. (3.40), and using Eqs. (3.22) and (3.23) to eliminate the bottom stresses yields

$$\left[\frac{N_o^2h^2}{2}+\frac{gh\epsilon}{\rho_o}-(\bar{u}^2+\bar{v}^2)\right]h_t=-\frac{\partial}{\partial t}\int_0^h[(\Delta u)^2+(\Delta v)^2]dz$$

$$+2N_o^2\beta\left\{\int_0^h\left[\Delta uz+\int_0^z\Delta u dz'\right]dz\right\}. \tag{3.43}$$

The integral multiplied by $2N_o^2\beta$ is identically zero, as can be shown by integrating either term in the curly brackets by parts.

By using Eqs. (2.22a) and (2.22b) Eq. (3.43) reduces to

$$\frac{N_o^2h^2}{2}+\frac{gh\epsilon}{\rho_o}-(\bar{u}^2+\bar{v}^2)+\alpha' u_*^2=0. \tag{3.44}$$

Note that here α' may also depend on the bottom slope.

Substituting Eq. (3.26) into Eq. (2.25) yields the overall Richardson number:

$$R_o = \frac{gh(\rho' - \rho_o(z,h))}{\rho_o(\bar{u}^2 + \bar{v}^2)} = \frac{\frac{gh\epsilon}{\rho_o} + \frac{N_o^2 h^2}{2}}{\bar{u}^2 + \bar{v}^2}. \tag{3.45}$$

Therefore from (3.44), when $\alpha' = 0$ the overall Richardson number is again equal to one during growth.

3.6. Summary of Sloping Bottom Equations

The governing equations for a sloping bottom are therefore:

$$\frac{\partial(h\bar{u})}{\partial t} - fh\bar{v} = -\frac{1}{\rho_o}\tau_b{}^x - \beta\frac{g}{\rho_o}\epsilon h \tag{3.46}$$

$$\frac{\partial(\bar{v}h)}{\partial t} + f\bar{u}h = -\frac{1}{\rho_o}\tau_b{}^y \tag{3.47}$$

$$\frac{g}{\rho_o}(h\epsilon)_t = \beta h\bar{u}N_o{}^2 \tag{3.48}$$

$$\alpha' u_*{}^2 - (\bar{u}^2 + \bar{v}^2) + \frac{gh\epsilon}{\rho_o} + \frac{N_o{}^2 h^2}{2} = 0. \tag{3.49}$$

which are respectively Eqs. (3.22), (3.23), (3.29) and (3.44). They are to be compared with their counterparts for the horizontal bottom case: (3.46) and (3.47) with (2.7) and (2.8); (3.48) has no counterpart since ϵ is zero when the sea bed is horizontal; and (3.49) with (2.23a). It can be seen that the only differences are the terms involving β and ϵ.

CHAPTER 4

NUMERICAL SOLUTIONS FOR HORIZONTAL AND INCLINED BOTTOM CASE

The solutions for mixed layer development are going to be presented as a function of time over both horizontal and sloping flat bottoms. The governing equations (3.46)-(3.49) must be solved numerically. First Eq. (2.35) is used to eliminate the bottom stress on the right-hand side of Eqs. (3.46) and (3.47) and then h and $\frac{\partial h}{\partial t}$ can be obtained from Eq. (3.49). Eliminating $\frac{\partial h}{\partial t}$ from Eqs. (3.46)-(3.48) yields

$$[h + \frac{2\bar{u}^2}{\sqrt{D}}]\frac{\partial \bar{u}}{\partial t} + \frac{2\bar{u}\bar{v}}{\sqrt{D}}\frac{\partial \bar{v}}{\partial t} + (\frac{g^2\epsilon}{N_o^2\rho_o^2\sqrt{D}} - \frac{g}{N_o^2\rho_o})\bar{u}\frac{\partial \epsilon}{\partial t}$$

$$= f\bar{v}h - C_d\bar{U}\bar{u} - \frac{\beta g}{\rho_o}h\epsilon \tag{4.1}$$

$$\frac{1}{\sqrt{D}}2\bar{u}\bar{v}\frac{\partial \bar{u}}{\partial t} + [h + \frac{2\bar{v}^2}{\sqrt{D}}]\frac{\partial \bar{v}}{\partial t} + (\frac{g^2\epsilon}{N_o^2\rho_o^2\sqrt{D}} - \frac{g}{N_o^2\rho_o})\bar{v}\frac{\partial \epsilon}{\partial t}$$

$$= -f\bar{u}h - C_d\bar{U}(\bar{v} + V_g) \tag{4.2}$$

$$[\frac{2g\epsilon\bar{u}}{\rho_o\sqrt{D}}]\frac{\partial \bar{u}}{\partial t} + \frac{2g\bar{v}\epsilon}{\rho_o\sqrt{D}}\frac{\partial \bar{v}}{\partial t} + (\frac{g^2\epsilon^2}{N_o^2\rho_o^2\sqrt{D}} - \frac{g\epsilon}{N_o^2\rho_o} + h)\frac{g}{\rho_o}\frac{\partial \epsilon}{\partial t}$$

$$= \beta N_o^2 h\bar{u} \tag{4.3}$$

where

$$D = \frac{g^2\epsilon^2}{\rho_o^2} + 2N_o^2[\bar{u}^2 + \bar{v}^2 - \alpha' u_*^2], \tag{4.4a}$$

and

$$h = -\frac{g\epsilon}{\rho_o N_o^2} + \frac{\sqrt{D}}{N_o^2}. \tag{4.4b}$$

Using the slab model Pollard et al. (1973) found a solution for the oceanic surface mixed layer thickness which tended to oscillate with time. Since a decrease in mixed layer thickness implies that the water is "unmixing", such oscillations can, according to Pollard et al. (1973) and Thompson (1973), not be real and they therefore kept the thickness h constant after it reached its maximum value. After the thickness h reaches its maximum value, the governing equations therefore become

$$h\frac{\partial \bar{u}}{\partial t} = f\bar{v}h - C_d\bar{U}\bar{u} - \frac{\beta g}{\rho_o}h\epsilon \tag{4.5}$$

$$h\frac{\partial \bar{v}}{\partial t} = -f\bar{u}h - C_d\bar{U}(\bar{v} + V_g) \tag{4.6}$$

$$\frac{\partial \epsilon}{\partial t} = \frac{\rho_o}{g}\beta N_o^2\bar{u}. \tag{4.7}$$

The initial conditions at $t = 0$ are:

$$h = \epsilon = \bar{u} = 0; \tag{4.8a}$$

but $\bar{v}$ should satisfy the nonslip condition:

$$\bar{v} = -V_g. \tag{4.8b}$$

However, Phillips et al. (1986) and Garrett (1990) show that a bidirectional shear flow induced by the buoyancy force can occur and result in restratification within a boundary layer on a sloping bottom. In this sense the thickness of bottom mixed layer may decrease and "unmixing" is possible. Therefore both cases of "unmixing" and "not unmixing" are presented and discussed in this thesis.

It is noticed that when substituting the initial conditions (4.8a) and (4.8b) into Eq. (3.49) it is found that this equation can not be satisfied except by

initially setting $V_g = 0$. This means either that the geostrophic velocity as a forcing term must start from zero or that the no-slip condition cannot be satisfied initially. But when $V_g = 0$ only the trivial solution $h = 0$ is obtained. Therefore the geostrophic velocity must start from a small value even though the no-slip condition cannot be satisfied at time zero. Thompson (1973) had the same problem. He used the overall Richardson number equal to one to close the set of governing equations. But from the no-slip initial conditions the overall Richardson number is zero except when $V_g = 0$. This indicates that $t = 0$ with a small value of the geostrophic velocity is a singular point of the governing equations. Fortunately this singular point doesn't affect the solutions very much. For most runs the solutions are stable with respect to the initial value of V_g, especially for strong stratification.

An additional problem results when V_g is allowed to increase rapidly to its steady value. This causes the thickness to overshoot and then oscillate at the inertial frequency, with unmixing problems as a result. For surface mixed layer problems the forcing may occur suddenly, due to a storm for example, and these inertial oscillations should produce additional mixing. Hence Pollard et al. (1973) used the maximum thickness during the first oscillation as their prediction of the surface mixed layer thickness. But the bottom mixed layer problem considered here concerns the equilibrium thickness due to steady geostrophic flow, for which the additional mixing through inertial oscillations generated by sudden start-up would result in overestimation of the thickness. This is why Weatherly and

Martin (1978) and Bird et al. (1982) used a ramped geostrophic velocity to suppress the inertial oscillations. Several different ramp functions which helped to diminish the inertial oscillations were tried here. They are

$$V_g = \begin{cases} 15t/T_g \text{ cm/s} & t < T_g \\ 15 \text{ cm/s} & t \geq T_g \end{cases} \tag{4.9}$$

which was used also by Weatherly and Martin (1978) with $T_g = 48$ h, and

$$V_g = 15\,[1 - e^{-(t/T_g)^2}] \text{ cm/s}, \tag{4.10}$$

$$V_g = \begin{cases} -15t\,(t - 2\,T_g)/T_g^2 \text{ cm/s} & t < T_g \\ 15 \text{ cm/s} & t \geq T_g, \end{cases} \tag{4.11}$$

where T_g is here respectively taken to be 48 and 96 hours. The third ramp is continuous at $t = 0$ and T_g, and its first derivative is continuous at $t = T_g$.

During the ramp period the friction velocity varies with the geostrophic velocity and extra terms will appear in the energy equation and momentum equation caused by the variation of V_g with time. Numerical experiments were carried out with and without these additional terms, and showed that their effect is small. The reason for this is that, for the ramp periods used, the thickness responds on a much shorter time scale than the time scale at which V_g is changing. This allows us to use Eq. (3.49). The term $\alpha' u_*^2$ in Eq. (4.48) is therefore kept constant during growth, and set equal to the value corresponding to the fully developed mixed layer. That is, the value of α' is taken to be either 0.59 or 6.3 and the value of u_* is calculated for a given bottom drag coefficient from Eq.

(2.40) using $V_g = 15\ cm/s$.

The program used to solve Equations (4.1)-(4.3) is based on the DGEAR routine in the International Mathematics Subroutine Library (IMSL). The DGEAR routine is a first order ordinary differential equation solver. It requires a subroutine provided by the user to determine the first order derivatives. For the problem discussed here the first derivatives can be obtained from Eqs. (4.1) to (4.3) easily as explicit functions of $\bar{u}$, $\bar{v}$ and ϵ (note that h is a function of $\bar{u}$, $\bar{v}$ and ϵ based on Eq. 3.49) by computing determinants. Then the Adams method is used with functional iteration by choosing two parameter values in the DGEAR routine (see IMSL user's manual, Edition 9.2, 1984, Vol. 1, page: DGEAR-2 and 3). The DGEAR routine worked very well for all the numerical experiments. The time step used was in the range 0.1–0.001 second. The error bound was 10^{-4}. The sampling interval for most runs was one hour. A few runs were sampled at intervals equal to 30 seconds, 8 minutes and 20 minutes. No detectable differences were found. The numerical results were also very stable for the different time steps.

4.1. Horizontal Flat Bottom ($\beta = 0$)

Much of the discussion of the results is related to observations made on the Western Florida Shelf by Weatherly and Van Leer (1977). The parameter values typical of these observations are: $f = 0.63\times10^{-4}/s$, $V_g = 15$ cm/s, and $N_o = 1.28\times10^{-2}/s$. This case was also solved by Weatherly and Martin (1978)

using the Level II turbulent closure model.

In the horizontal bottom case only Eqs. (4.1) to (4.3) were solved. "Unmixing" was not a serious problem so Eqs. (4.5) to (4.7) were not used. Typical parameter values and results are presented in Table 4.1. The range of $\frac{N_o}{f}$ given in this Table is large, from 0.875 to 203. The purpose of presenting these results is to check the sensitivity to particular parameter values and for later comparisons. The time series of thickness, speed and veering angle for a typical case are given in Fig. 4.1 which shows that the flow approaches a steady state very quickly after V_g reaches its final value. A small amount of inertial overshoot does occur especially in the thickness (i. e. the water is allowed to unmix here). This causes some error. For example when the ramp function (4.9) is used as in Figure 4.1, the flow at $t = 48$ hours is within a relative error of 5 % of the final steady state. After the overshoot there appear small oscillations but these quickly decay. Oscillations with a relative amplitude error larger than $10^{-2}\%$ disappear in a few hours after the geostrophic velocity reaches a constant value.

The drag coefficient has a large effect on the thickness of the mixed layer and on the veering angle. This can be seen by examining Table 4.1. For example, using $\alpha' = 6.3$ for the observed case ($N_o = 1.28 \times 10^{-2}$ /s, $f = 0.63 \times 10^{-4}$ /s, $V_g = 15$ cm/s, Weatherly and Van Leer, 1977), the thickness is about 7.2 meters (Fig. 4.1) and the Ekman veering angle is -26.5 degrees if $C_d = 0.17 \times 10^{-3}$. In contrast, the thickness is 9.9 meters and the veering angle is -37.5 degrees if

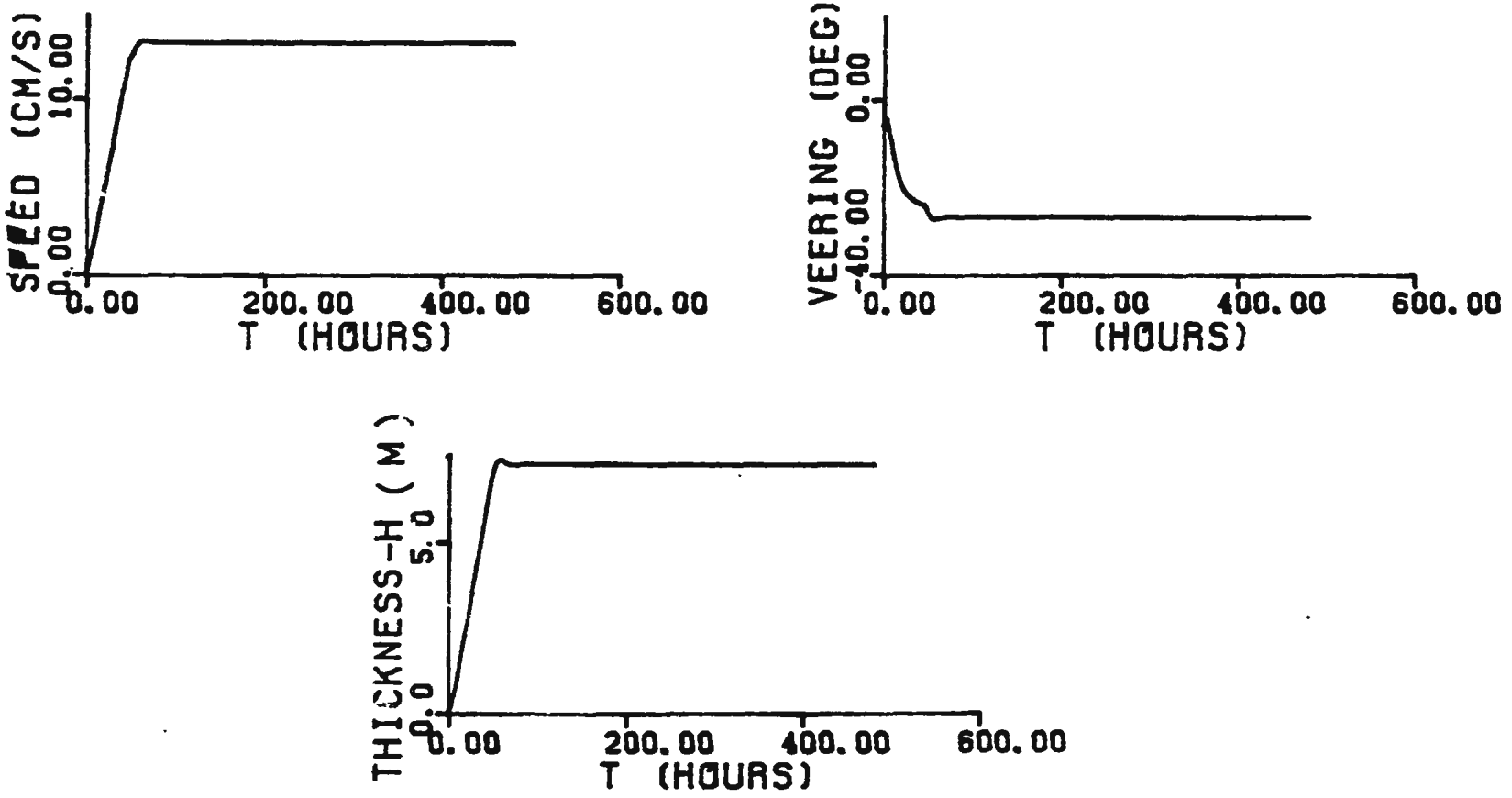

Figure 4.1. The variation of the thickness, speed, and veering angle with time during the growth of the bottom boundary layer on a horizontal flat bottom. The parameters are: $\alpha' = 6.3$, $V_g = 15$ cm/s, $Cd = 0.17\times10^{-2}$, $No = 1.28\times10^{-2}$/s and $f = 0.63\times10^{-4}$/s. Ramp function (4.9) was used.

run		145	174	117	112	197	382	383
V_g cm/s		15	15	15	30	15	18.92	18.92
$N_o \times 10^{-4}$ /s		128	128	64	7	7	0.7	0.7
N_o/f		203	203	102	11	11	0.88	0.88
α'		6.3	6.3	0.59	0.59	0.59	6.3	0.59
$C_f \times 10^{-3}$		1.7	4.	1.7	1.7	1.7	1.6	1.6
numerical	h (m)	7.2	9.9	10.9	68.1	34.1	37.3	95.5
	α (deg)	-26.5	-37.5	-19.3	-6.7	-6.7	-5.8	-2.3
	$\bar{u}$ (cm/s)	-6.0	-7.2	-4.7	-3.5	-1.7	-1.9	-0.75
	$\bar{v}_1$ (cm/s)	12.0	9.4	13.4	29.7	14.8	18.7	18.9
analytic	h (m)	7.3	10.0	10.9	68.1	34.1	37.8	92.9
	α (deg)	-26.3	-37.2	-19.3	-6.7	-6.7	-5.8	-2.3
	u (cm/s)	-6.0	-7.2	-4.7	-3.5	-1.7	-1.9	-0.77
	$\bar{v}_1$ (cm/s)	12.1	9.5	13.4	29.7	[illegible]8	18.7	18.7

Table 4.1. The comparisons between the analytic solutions for steady flow and the asymptotic numerical results for unsteady flow over a horizontal flat bottom. In the table $\bar{v}_1 = \bar{v} + V_g$ is y-component of averaged velocity in the layer. The Coriolis parameter $f = 0.63 \times 10^{-4}$ for runs 145, 174, 117, 112 and 197, while $f = 0.8 \times 10^{-4}$ for runs 382 and 383. Ramp function (4.9) was used.

$C_d = 4\times10^{-3}$. The latter results are more consistent with the observed values: $h = 6$ to 11 meters and Ekman veering $\alpha = -30$ to -75 degrees.

Again when $\frac{N_o}{f}$ is small the numerical results show that the choice of α' is important. This is illustrated by Runs 382 and 383 in Table 4.1. The difference of thickness between $\alpha' = 0.59$ and $\alpha' = 6.3$ is about three times which is attributed to different definitions of thickness as discussed before. Also the veering angles and the transverse velocities are quite different.

The comparisons between the analytic solutions for h, α, $\bar{u}$ and $\bar{v}$, Eqs. (2.29), (2.36), (2.38) and (2.39), for steady flow and the steady-state results from the numerical solutions using the ramp function (4.9) are also given in Table 4.1. Because for a horizontal flat bottom the numerical solutions reach a steady state quickly, all numerical results presented in Table 4.1 are the equilibrium values. Both $\alpha' = 6.3$ and 0.59 are also used. It can be seen that the numerical results are almost identical to the analytic values. This supports the assumption that α' only depends on $\frac{N_o}{f}$ for the horizontal bottom case, and also shows that the ramp function doesn't affect the application of the assumption.

Inertial oscillations do appear at $t = T_f$ for some values of the Brunt-Vaisala frequency, drag coefficient, and Coriolis parameter for certain ramp functions. If the water is not allowed to unmix when overshoot occurs, the thickness is then larger than that obtained from the analytic solution. However the differences are small. Furthermore, it was found that the overshoot and the

inertial oscillations could be eliminated by choosing ramp functions of the form (4.10) or (4.11), and T_g sufficiently long. This suggests that the overshoot phenomenon is an artifact caused by the ramp function.

4.2. Sloping Flat Bottom

4.2.1. Summary of Weatherly and Van Leer's observations

The observations discussed here were made by Weatherly and Van Leer (1977) on the western Florida Continental Shelf between 3 and 8 July 1976. The mooring was located near the shelf break. From the topography (see Fig. 4.2 replotted here from Fig. 3 in Weatherly and Martin, 1978) the bottom slope varies from 0.26×10^{-3} to 2.4×10^{-3}. Figure 4.2 also indicates that the isotherms are approximately parallel to the isopycnals. The water depth at the location was about 101 m. The profiles of velocity, temperature and conductivity (Fig. 4.3) were made by cyclosonde (Van Leer et al., 1974) and were sampled at intervals of 2.5 m from 3 m above the bottom to 13 m below the water surface. During the observations the interior velocity was northward for the first 48 hours. From 48 h to 72 h it shifted to westward, and then became southward afterwards.

When the interior flow was northward, shallow water was to the right and the transverse flow in the boundary layer therefore caused downwelling of warmer water. Therefore hereafter the northward interior flow is often referred to as the downwelling case. When the interior flow was southward, shallow water was to the left therefore upwelling of colder water occurred. The southward interior flow is often referred as the upwelling case.

The temperature time series recorded by cyclesonde at fixed depths are reproduced in Fig. 4.4. From the profiles (see Fig. 4.3) and temperature time

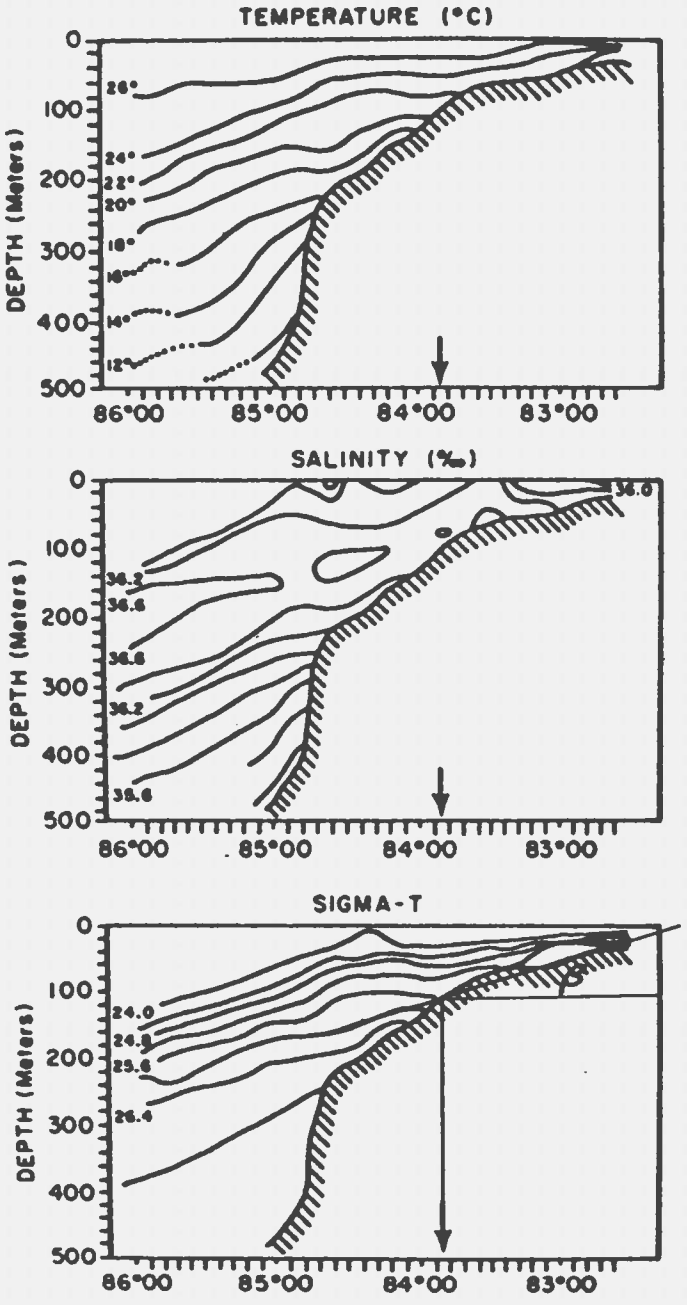

Figure 4.2. Temperature, salinity and σ_t transect along 26° N on 2 June 1972. The site of the observation (arrow) is about 100 m depth and near a shelf break point where the bottom slope changed from 0.26×10^{-3} to 2.4×10^{-3}. This Figure is copied from Fig. 3 of Weatherly and Martin (1978).

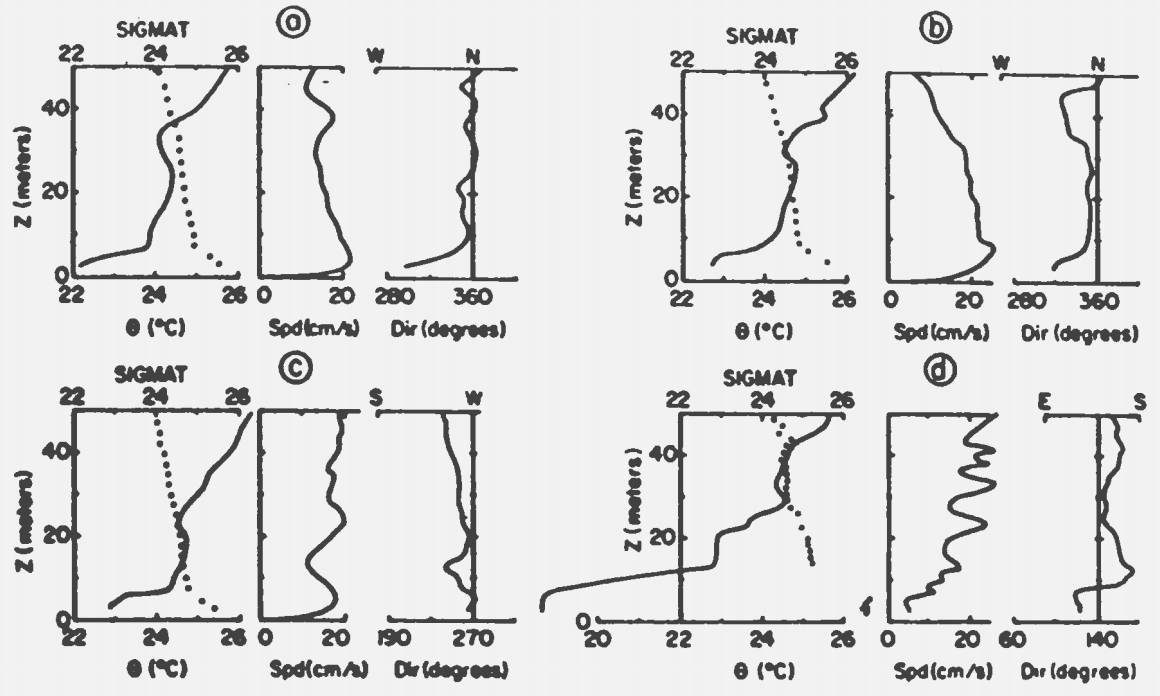

Figure 4.3. Representative temperature, speed and current direction profiles taken from data reported in Weatherly and Van Leer (1977). Profiles (a) and (b) correspond to northward interior flow. Profiles (c) were taken when the interior flow was westward. Profiles (d) correspond to southward interior flow. Dotted curves are σ_t profiles. Note that for $z > 10$ m $\frac{\partial \sigma_t}{\partial z}$ is nearly constant. This Figure is taken from Fig. 1 of Weatherly and Martin (1978).

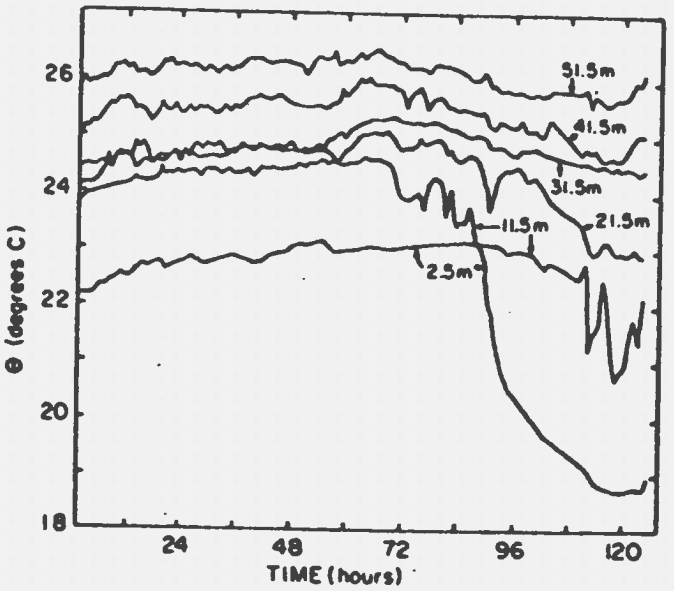

Figure 4.4. Observed temperature time series at various heights above the sea floor at the location 26°0'N, 83°49'W on the western Florida Continental Shelf. This Figure is copied from Fig. 2 of Weatherly and Martin (1978).

series Weatherly and Van Leer (1977) deduced that when the interior flow was northward, the thickness of the bottom boundary layer was 6 m, the average (with respect to time) veering angle between the interior flow and the flow near the sea-floor was -30 degrees, and the temperature in the mixed layer increased slowly with time (see Fig. 4.4). During southward flow the thickness was 11 m, the average veering angle was -75 degrees, and the temperature decreased rapidly with time. In both cases, most of the veering occurred in the region of maximum temperature gradient at the top of the mixed layer, so that the veering angle was nearly constant within the mixed layer itself.

4.2.2. Weatherly and Martin's numerical results

Weatherly and Martin (1978) simulated the above observations using the Level II turbulent closure model. They assumed that the isotherms were horizontal (no thermal wind), that in the interior the flow was geostrophic and parallel to the isobaths, that the stratification in the interior was constant and all deviations in the bottom boundary layer from the interior quantities varied only with distance normal to the bottom and with time. During northward flow the bottom slope was defined to be positive and chosen as 0.26×10^{-3}, since the transverse flow at the mooring site was coming from the less steeply sloping region to the east of the mooring (Fig. 4.2). During the southward interior flow the bottom slope is negative and chosen to be -2.4×10^{-3}, since the transverse flow was then coming from the more steeply sloping region to the west of the mooring (Fig. 4.2). The

temperature time series and temperature profiles obtained are reproduced here in Fig. 4 5 for both the downwelling case ($\beta = 0.26\times10^{-3}$) and the upwelling case ($\beta = -2.4\times10^{-3}$).

The results show that the temperature in the mixed layer decreases with time for the upwelling case, and increases with time for the downwelling case. For the upwelling case the thickness reached a nearly constant value of about 5 m (see Fig. 4.5) but other quantities like veering angle and temperature varied with time. At Day 4 ($t = 96$ h) the temperature in the mixed layer was 21° C, the vertically averaged speed was about 4.5 cm/s, the total veering angle was - 28 degrees, the vertically averaged (over the depth of the mixed layer) veering angle was estimated from Fig. 10 in their paper to be - 16 degrees and the thickness was about 5 m.

For the downwelling case the computed thickness and the temperature increased with time (see Fig. 4.5). At day 4 the temperature was 22.5° C, the total veering angle was about -23 degrees, the vertically averaged veering angle was estimated to be -19 degrees, and the thickness was about 10 m.

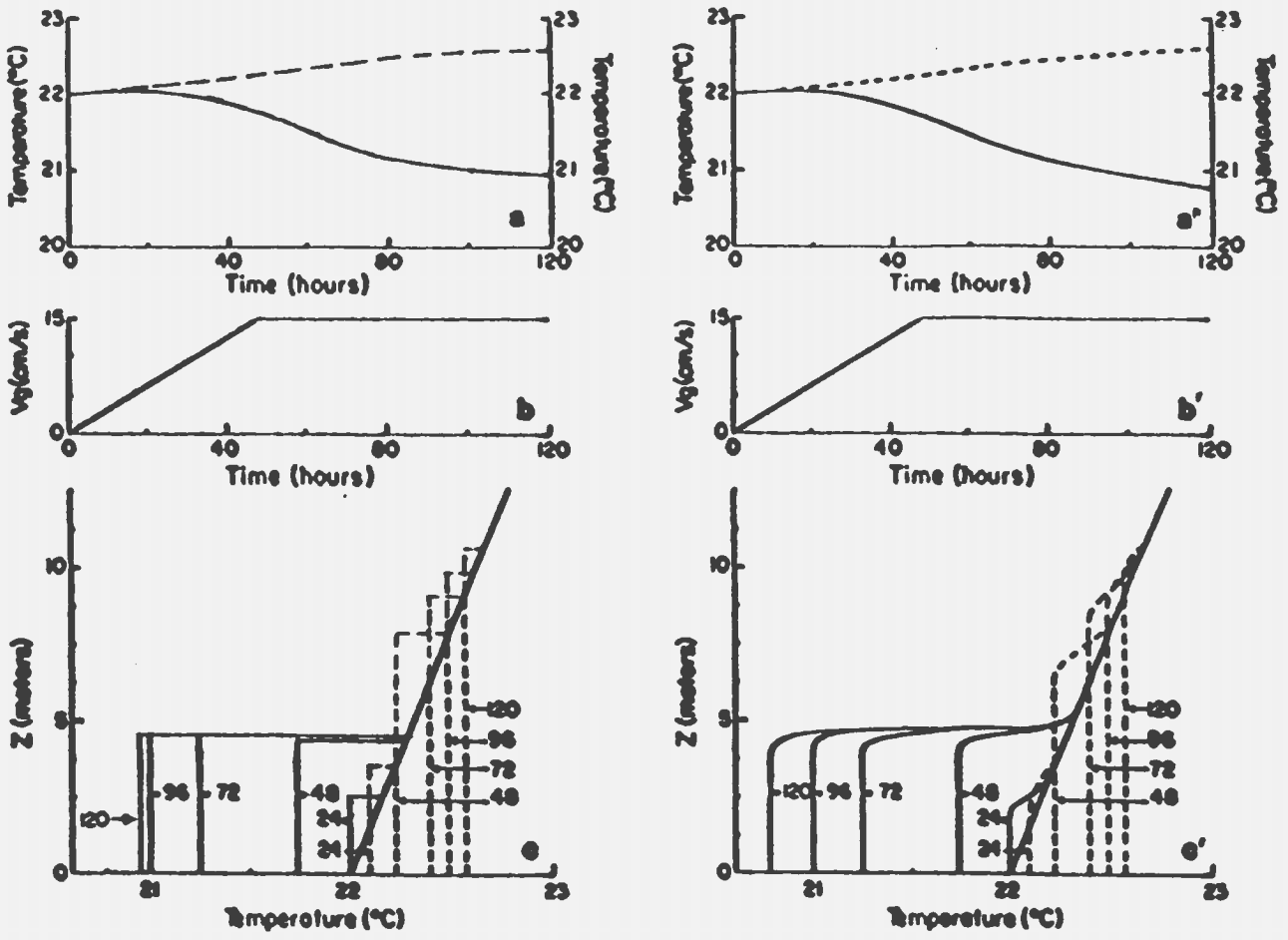

Figure 4.5. Time series (a) of the temperature of the bottom mixed layer as a function of time for α'=0.59 and V_g as indicated in (b), temperature profiles (c) at times 0, 24, 48, 72, 96 and 120 hours, and solid curves are for the case $\beta = -2.4\times10^{-3}$ and the dashed curves are for the case $\beta = 0.26\times10^{-3}$. ($a'$), ($b'$) and ($c'$) are Weatherly and Martin's results (1978)

4.2.3. Vertically-integrated model results

In order to compare this model with the Level II turbulent closure model and the observations on the western Florida Continental Shelf, the same parameter values are used here including bottom slope β: 2.6×10^{-4} and -2.4×10^{-3}, corresponding to the downwelling and the upwelling cases respectively. $f = 0.63\times10^{-4}$/s and $N_o = 1.28\times10^{-2}$/s (corresponding to the initial temperature gradient $S = \frac{dT_i}{dz} = 7\times10^{-4}$° C/cm used by Weatherly and Martin). It is assumed that the dependence of α' on the bottom slope can be omitted so that the term $\alpha' u_*^2$ in Eq. (4.4a) is again constant during growth, and equal to the value corresponding to the fully developed mixed layer. This is justified because $\frac{N_o}{f}$ is large (203) for the case considered, and therefore the results are not expected to depend strongly on the value of α'. Thus, the value of α' is taken to be either 0.59 or 6.3 as for the horizontal flat bottom case, and the value of u_* is calculated from Eq. (2.40) for a given bottom drag coefficient and $V_g = 15$ cm/s. Equations (4.1) to (4.3) are then solved with ramp function (4.9).

The values of density given by the solutions for Eqs. (4.1) to (4.7) must be converted to temperature in order to make comparisons with Weatherly and Martin's results (1978), since they took density to be a function of temperature alone. The thermal expansion coefficient ξ is

$$\xi = -\frac{1}{\rho}\frac{d\rho}{dT}. \tag{4.12}$$

Therefore it can be written that

$$N_0^2 = -\frac{g}{\rho}\frac{d\rho}{dz} = g\xi\frac{dT_i}{dz} = gS\xi. \tag{4.13}$$

Using Weatherly and Martin's values of S and N_0 (see above), this gives $\xi = 2.39\times10^{-4}/C$, which is comparable to tabulated values (see for example Gill, 1982, p. 603). Using this value of ξ, the time series of temperature can be obtained from Eqs. (4. 12) and (3. 11). That is,

$$\xi(T' - T_0(z, 0)) = \frac{N_0^2}{2g}h - \frac{\epsilon}{\rho_0} \tag{4.14}$$

The computed time series of temperature in the bottom mixed layer, and the computed temperature profiles are given in Fig. 4.5, together with those obtained by Weatherly and Martin. Fig. 4.5 shows good agreement between the two models. This implies that the dependence of α' on bottom slope β can be ignored. The results for the downwelling case and the upwelling case are discussed separately below.

4.2.3a. Downwelling case

As pointed out in Section 4.2.2 during northward flow the bottom slope is positive (shallow water is on the right) and downwelling occurs. The results given in Figs. 4.5 and 4.6 show that the thickness continues to increase with time after

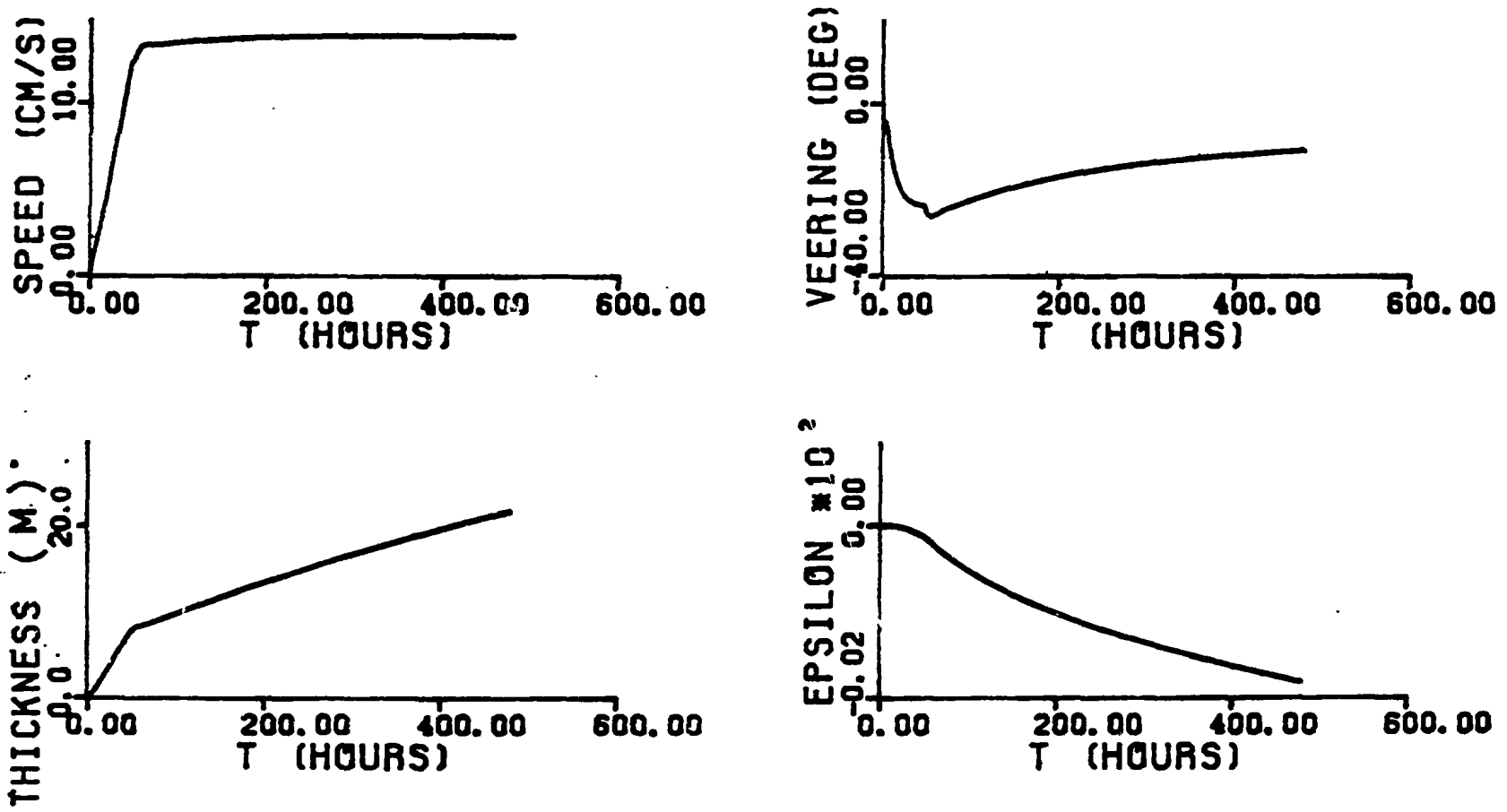

Figure 4.6. The variation of the thickness, speed, veering angle, and ϵ for the downwelling case ($\beta = 0.26\times10^{-3}$) during the growth of the bottom boundary layer on a sloping flat bottom. The parameters are: $\alpha' = 0.59$, $V_g = 15$ cm/s, $C_d = 0.19\times10^{-2}$, $N_o = 1.28\times10^{-2}$/s. The ramp function is (4.9). The units of EPSILON are g/cm^3.

the geostrophic velocity reaches a constant value. The computed thickness time series is also given in Fig. 4.5. The thickness time series is very comparable to that obtained from the Level II turbulent closure model.

The advective density anomaly ϵ is negative and small during the ramp period, but increases in magnitude as time progresses. Similar behavior is evident in the temperature time series in Figs. 4.5 a and a' for both models.

The speed in the mixed layer is 12.4 cm/s at t=48 hours then increases slowly and approaches a constant value of 14 cm/s. The Ekman veering increases to a maximum -26.4 degrees then decreases slowly.

For the downwelling case there is no overshoot and no inertial oscillations appear in the numerical results, probably because the thickness still increases with time after the geostrophic velocity reaches a constant value.

Because results were given at $t = 96$ h by Weatherly and Martin (1978), for comparison results at the same time obtained from the vertically integrated model are presented. These, together with the Level II model results and observed data are listed in Table 4.2. The values of veering angle and speed from the Level II model presented in Table 4.2 have been vertically averaged in order to make direct comparisons with those obtained from the vertically integrated model. The observed temperature values in Table 4.2 are estimated from Fig. 4.4, corresponding respectively to the values at the end of northward interior flow and at the end of southward interior flow. The observed speed is the vertically

averaged value estimated from Fig. 4.3. Table 4.2 shows that the vertically integrated model results are very close to those computed from the Level II turbulent closure model.

model	Vertically Integrated		Level II Turbulent Closure		model	Observation	
case	downwelling	upwelling	downwelling	upwelling	case	downwelling	upwelling
h (m)	9.8	4.6	10	5	h (m)	6.0	11.0
T (°C)	22.56	20.97	22.5	21	T (°C)	22.80	18.90
α (degrees)	-23.5	-14.3	-19	-16	α (degrees)	-30.0	-75.0
$\bar{U}$ (cm/s)	13.6	4.7	13.5	4.5	$\bar{U}$ (cm/s)	20.0	4.6

Table 4.2. The values of thickness h, temperature T, (vertically averaged) veering angle α and speed $\bar{U}$ at time $t = 96$ h in the mixed layer obtained from the vertically integrated model and the values of the same parameters obtained by Weatherly and Martin (1978) using the Level II turbulent closure model. The observed temperature values are estimated from Fig. 4.4, corresponding respectively to the values by the end of northward interior flow and by the end of southward interior flow. The observed speed is the vertically averaged value estimated from Fig. 4.3. The observed veering angle is the time-averaged angle between the interior flow and the flow near the sea-floor.

4.2.3b. Upwelling case

Figures 4.7 and 4.8 show the time series of thickness, density anomaly, speed and veering angle for the upwelling case (southward interior flow, $\beta = -2.4\times10^{-3}$). "Unmixing" was a problem for this case, as can be seen from Fig. 4.7. Inertial oscillations can also be seen to be present, particularly in the veering angle results. The results when "unmixing" is inhibited are shown in Fig. 4.8. The differences between Figs. 4.7 and 4.8 are small at times either less than or much greater than the ramp time of 48 h. From Figure 4.8 it can be seen that the thickness reached its maximum value of about 4.6 m at 50 hours. The thickness is also presented as a function of time in Fig. 4.5, which shows that the thicknesses are basically the same as those obtained from the Level II turbulent closure model.

The advective density anomaly ϵ is positive and increases with time, since deeper and colder water is advected up the slope. The temperature time series and temperature profiles as a function of time are given in Fig. 4.5, which shows that the temperatures and mixed layer thicknesses obtained from both the vertically integrated model and the Level II turbulent closure model are comparable.

The speed increases to a maximum value of 9.2 cm/s then decreases monotonically. The maximum veering angle is - 29.3 degrees.

For more direct comparison with the Level II turbulent closure model, again the results at $t = 96$ h (Table 4.2) are presented. It is seen that the two models

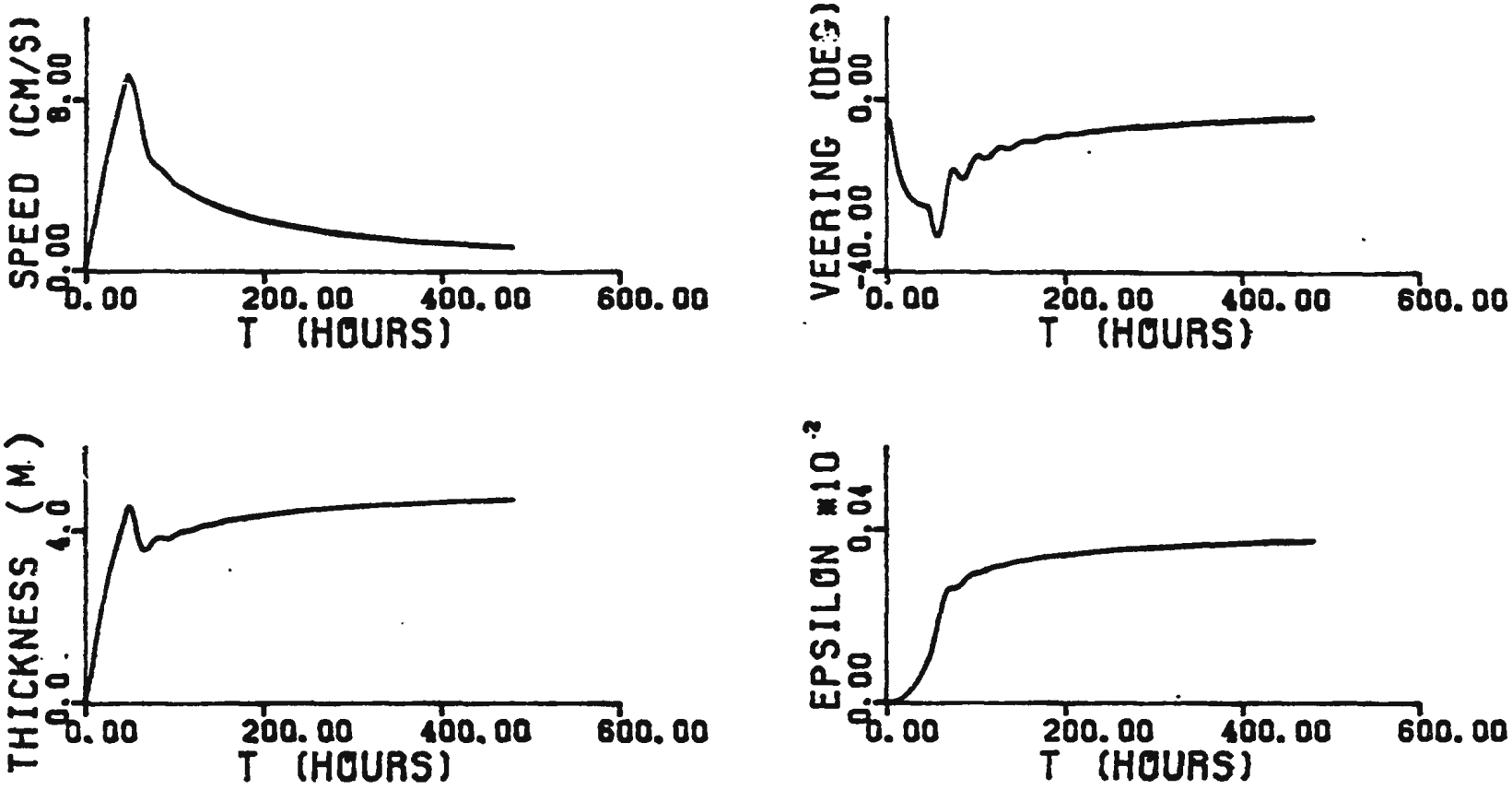

Figure 4.7. The variation of the thickness, speed, veering angle, and ϵ with time for the upwelling case ($\beta = -2.4\times10^{-3}$) during the growth of the bottom boundary layer on a sloping flat bottom. The parameters are: $\alpha' = 0.59$, $V_g = 15$ cm/s, $C_d = 0.19\times10^{-2}$, $N_o = 1.28\times10^{-2}$/s. The thickness is allowed to decrease: that is, "unmixing" is not inhibited. Ramp function is (4.9) The units of EPSILON are g/cm^3.

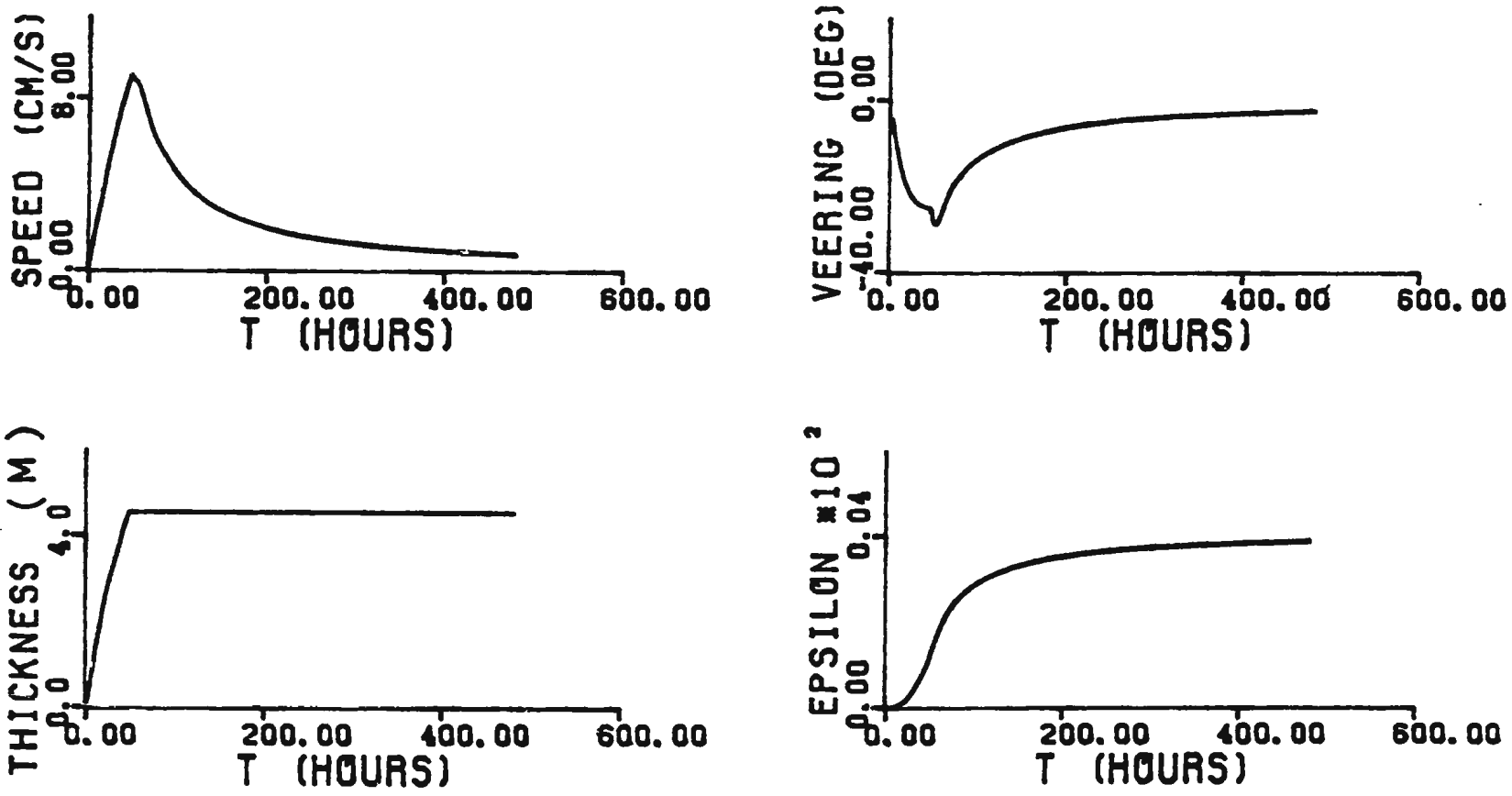

Figure 4.8. The variation of the thickness, speed, veering angle, and ϵ with time for the upwelling case ($\beta = -2.4\times10^{-3}$) during the growth of the bottom boundary layer on a sloping flat bottom. The parameters are: $\alpha' = 0.59$, $V_g = 15$ cm/s, $C_d = 0.19\times10^{-2}$, $N_o = 1.28\times10^{-2}$/s. The decrease of thickness is not allowed: that is, "unmixing" is inhibited. The ramp function is (4.9). The units of EPSILON are g/cm^3.

yield very similar results.

When the thickness is permitted to decrease (Fig. 4.7) the thickness reaches about 4.6 m and then drops to about 3.5 m. After that the thickness gradually approaches an almost constant value of 4.7 m which is nearly the same as that obtained by Weatherly and Martin (1978). The amplitude of the overshoot and subsequent inertial oscillations are much larger for a sloping bottom in the upwelling case than for either the downwelling case or for a horizontal flat bottom. However, when different ramp functions Eqs. (4.10) and (4.11) with $T_f \geq 48$ (Eq. 4.10 is better than Eq. 4.11) are used it is found that the overshoot and the inertial oscillations can be largely eliminated.

4.2.4. Comparisons with Observations

From Figs. 4.4 and 4.5 it can be seen that when the interior flow was northward (time $\leq$ 48 hours), temperature time series obtained from both the vertically integrated model and the Level II turbulent closure model are basically consistent with the observations made by Weatherly and Van Leer (1977). The temperature increases slowly with time. When the interior flow was southward (time $\geq$ 72 hours) the temperature time series from both models again have the same tendency as the observations: that is, the temperature decreases with time. However, the observed cooling rate is much larger than predicted.

The thicknesses computed from both models are about the same and are in the same range as the observed values (Table 4.2). But there are two

discrepancies. One is that for the downwelling case the observed thickness remains constant at 6 m while the computed thickness increases with time. Within 5 days the computed value can reach 10 m (Fig. 4.5). The other is that the predicted thickness (about 5 m) for the upwelling case is less than the predicted thickness (about 10 m) for the downwelling case, whereas the opposite is true for the observations: the observed thickness is 11 meters for the upwelling case, and 6 m for the downwelling case.

The computed veering angles from both models are smaller than those observed, especially for the upwelling case (Table 4.2). Furthermore, comparing Figure 4.6 with either Figure 4.7 or 4.8 shows that at times greater than the ramp period the predicted veering for the downwelling case is substantially greater than that for the upwelling case. As with the thicknesses, this is the opposite of the observations. Therefore even the fact that the model results represent a vertical average, while the observed values are the difference between the direction of the interior flow and that near the bottom, is unlikely to fully account for the discrepancy.

There are several possible causes of the discrepancies between the numerical results obtained here and by Weatherly and Martin (1978), and the observations reported by Weatherly and Van Leer (1977). The first is that both models ignore the possible effects of thermal wind. From Fig. 4.3 it can be seen that the vertical shear in the interior was negative during northward flow (downwelling case). When the thickness of the mixed layer increases the geostrophic velocity at the

interface would therefore decrease under these conditions. Therefore the kinetic energy of water entrained into the mixed layer would also decrease, which should lead to diminished energy available for mixing and retard the growth of the mixed layer. For southward flow on the other hand, because the vertical shear in the interior was positive (Fig. 4.3), the velocity at the interface would increase during growth, potentially leading to greater thicknesses. The effects of including thermal wind on the vertically-integrated model results are presented in Chapter 5.

A second possibility is that the calculations ignore the actual history of mixed layer development. For example, when the interior flow reverses to the southward direction a bottom mixed layer already exists, unlike the initial conditions assumed in the numerical computations ($h = 0$). Furthermore in the observations the interior flow was westward for 24 hours before shifting to southward flow. The westward interior flow must have induced upwelling near the coast, and may have contributed to the higher observed cooling rate.

4.2.5. Asymptotic Solutions for Steady Flow over a Sloping Bottom

The principal results of the 5-day simulations obtained above show that the temperature of bottom boundary layer can increase (corresponding to downwelling case) or decrease (upwelling case). But the recent work by Rhines and MacCready (1989) shows that when the development time of the bottom boundary layer is larger than a time scale given by $2f\,(N_o \sin\beta)^{-2}$ the buoyancy force can reach a balance with the driving pressure gradient force. After this time upwelling or downwelling ceases and the Ekman flux is extinguished. However, it should be noted that this time scale is independent of the sign of the bottom slope, in apparent contradiction with the results in Figure 4.5.

Phillips (1986), Thorpe (1987) and Garrett (1990) presented a different picture of flow on a sloping bottom. When the flow within the bottom boundary layer becomes steady a bidirectional secondary flow forms parallel to the bottom in the $x-z$ plane. Therefore it is interesting to investigate the steady flow in terms of the vertically integrated model.

For steady flow the time-dependent terms are dropped and the governing equations (3.46)-(3.49) become

$$-fh\bar{v} = \frac{-1}{\rho_o}\tau_b{}^x - \frac{\beta g \epsilon}{\rho_o} \tag{4.15}$$

$$fh\bar{u} = -\frac{1}{\rho_o}\tau_b{}^y \tag{4.16}$$

$$\beta h\bar{u}N_o{}^2 = 0 \tag{4.17}$$

$$\alpha' u_*{}^2 - (\bar{u}^2 + \bar{v}^2) + \frac{gh\epsilon}{\rho_o} + \frac{N_o{}^2 h^2}{2} = 0. \tag{4.18}$$

From Eq. (4.17) it is deduced that

$$\bar{u} = 0. \tag{4.19}$$

That is the Ekman flux is extinguished as demonstrated by Rhine and MacCready (1989) in their experiment. The bottom boundary layer becomes arrested.

By using a quadratic drag law Eq. (4.16) results in

$$\bar{v} = V_g \tag{4.20}$$

which can also be obtained from the equation used by Rhines and MacCready (1989). Substituting Eqs. (4.19) and (4.20) into Eq. (4.15) yields

$$-f V_g = \frac{\beta g \epsilon}{\rho_o}. \tag{4.21}$$

From the geostrophic balance equation (3.5), therefore,

$$\frac{\beta g \epsilon}{\rho_o} = -\frac{1}{\rho_o}\frac{\partial P_o}{\partial z} - g\beta. \tag{4.22}$$

The driving force in the boundary layer in the z-direction is

$$-\frac{\partial P'}{\partial z} - \rho' g \beta = -\frac{\partial P_o}{\partial z} - \rho' g \beta \tag{4.23}$$

where Eq. (3.14) has been used. Substituting Eq. (4.22) and using Eq. (3.8) we therefore have

$$-\frac{\partial P'}{\partial z} - \rho' g \beta = -\rho'' g \beta. \tag{4.24}$$

The driving force is, according to Eq. (4.24), equal to the buoyancy force only caused by the local mixing which locally is not zero and varies with height above bottom (Eq. 3.12). But the vertical integral of Eq. (4.24) over the mixed layer thickness shows that the vertically integrated pressure gradient is balanced by

vertically integrated gravity. This result is different from the pressure gradient being balanced by gravity, given by Rhines and MacCready (1989). Eq. (4.24) also shows that for the upwelling case ($\beta < 0$) the driving force in the upper half of the bottom mixed layer is always larger than zero, since $\rho'' > 0$ for $z > h/2$: that is, the driving force always tries to drive fluid down slope, while the driving force in the lower half of bottom mixed layer is always less than zero, since $\rho'' < 0$ for $z < h/2$, and tries to drive fluid up slope. For the downwelling case ($\beta > 0$) the driving force in the upper half of bottom mixed layer is always less than zero due to $\rho'' > 0$ and also tends to drive fluid down slope while in the lower half the driving force also tries to drive fluid up slope. Therefore the driving force in the bottom mixed layer should produce a secondary circulation within the boundary layer, which tends to restore the stratification, as shown by Phillips et al. (1986) and Garrett (1990).

From Eqs. (4.18) and Eq. (4.21) the asymptotic solutions for h, and ϵ, are:

$$h = \frac{-\frac{fV_g}{\beta} + \sqrt{\frac{(fV_g)^2}{\beta^2} - 2N_o^2(\alpha' u_*^2 - V_g^2)}}{N_o^2} \tag{4.23}$$

and

$$\epsilon = -\frac{\rho_o f}{\beta g} V_g . \tag{4.24}$$

For the observations made on the western Florida Continental Shelf by Weatherly and Van Leer (1977) the calculated values of h and ϵ based on Eqs. (4.23) and (4.24) are: $h = 5.17$ m and $\epsilon = 0.41 \times 10^{-3}$ g/cm^{-3} for the upwelling case

($\beta = -2.4\times10^{-3}$), and $h = 440$ m and $\epsilon = -3.7\times10^{-3}$ g/cm^{-3} for the downwelling case ($\beta = 0.26\times10^{-3}$). As shown in Figs 4.9 and 4.10, these results are consistent with the numerical solutions for sufficiently long mixed layer development times after the ramp period. Fig. 4.9 presents the time series of h, ϵ, speed and veering angle for 4800 h (200 d) obtained from the numerical results for the upwelling case. The thickness h has reached 5.1 m and $\epsilon = 4.07\times10^{-4}$ g/cm^{-3}. The vertically averaged veering angle and the speed tend to zero and the bottom boundary layer becomes arrested. Fig. 4.10 presents the time series of h, ϵ, speed and veering angle for the downwelling case. After almost 217 years the thickness h is still approaching a nearly constant value of about 390 m. The vertically averaged veering angle and the speed are still tending to zero but the bottom boundary layer has not yet been completely arrested. The reality of results for the downwelling case is doubtful because after so many years the flow of the ocean would have changed its type long before.

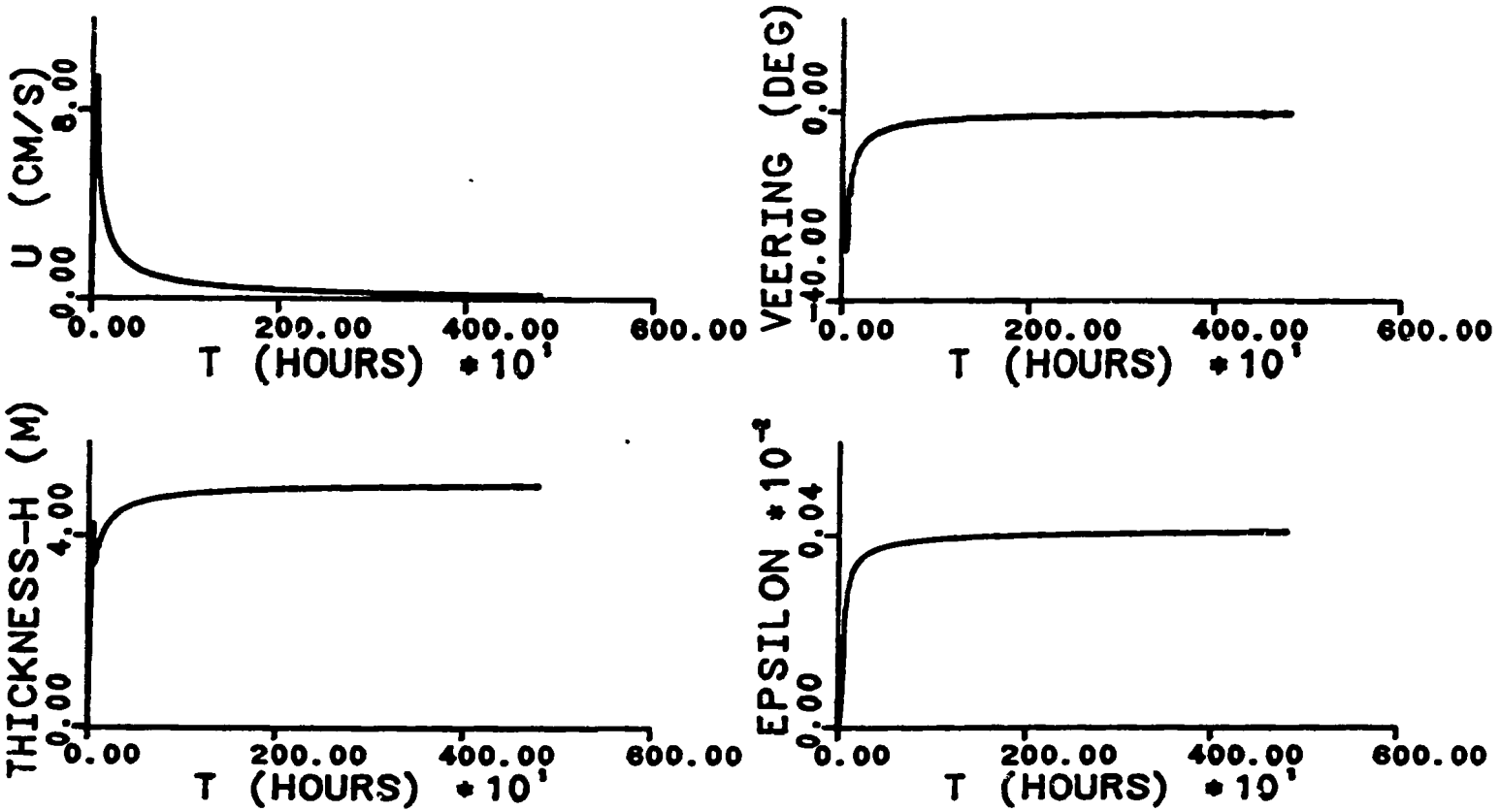

Figure 4.9. The time series of the thickness, speed, veering angle and ϵ for the upwelling case. All parameters and units are the same as in Fig. 4.7. The time duration is 4800 H.

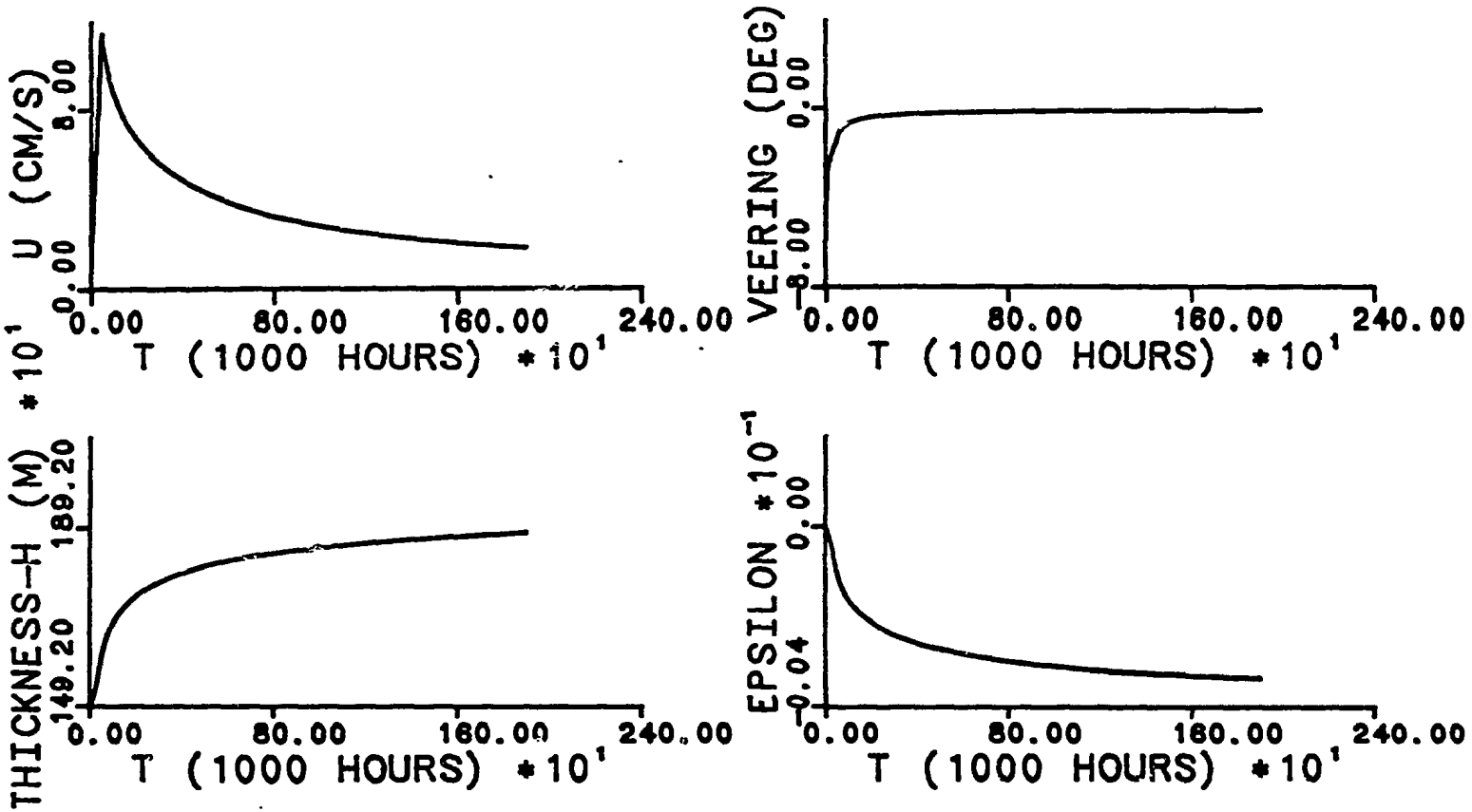

Figure 4.10. The time series of the thickness, speed, veering angle and ϵ for the downwelling case. All parameters and units are the same as in Fig. 4.6. The time duration is 216.7 years.

CHAPTER 5

EFFECTS OF THERMAL WIND ON BOTTOM MIXED LAYER GROWTH

When thermal wind effects were ignored in Chapter 4, the 5-day's simulation results obtained from both the vertically integrated model and the Mellor-Yamada Level II turbulent closure model showed that the thickness continued to increase with time for the downwelling case. This was shown to be inconsistent with the observations on the western Florida Continental Shelf during northward flow. As discussed before, the negative vertical shear of V_g in the interior (Figs. 4.3 a and b) might be expected to limit mixed layer growth. In this Chapter this aspect of the problem is examined.

The importance of the thermal wind to bottom boundary layer dynamics has been demonstrated by Yamada and Mellor (1975). They used their Level III turbulent closure model to simulate atmospheric data from Wangara (Clarke et al., 1971). Their sensitivity studies showed that the thermal wind was essential to explain the mixed layer growth observed at Wangara. Manins (1982) compared results from a slab model to the Wangara data. When the geostrophic wind was weak he assumed, as in the so-called 'encroachment' model of Carson and Smith (1974), that mixing was driven by convection due to surface heating. But when the geostrophic wind is strong the 'encroachment' assumption is no longer applicable. Manins therefore used the turbulent kinetic energy equation derived by

Mahrt and Lenschow (1976). They assumed that there exists both a temperature jump and a velocity jump at the top of the mixed layer, with linear changes in the thin jump region. Manins assumed that the whole mixed layer was uniform and moved like a slab, and set up a closure model which he called the Froude Dynamics Model. This model gave additional mixed layer growth when the geostrophic wind was strong. For both strong and weak geostrophic wind cases the results reconfirmed the importance of the thermal wind for predicting mixed layer height and vector wind in the mixed layer during the Wangara experiment.

At Wangara the stratification was very strong ($N_o \sim 7\times10^{-2}$ /s, $f \sim 10^{-4}$ /s and thus $\frac{N_o}{f} \sim 700$), and slab models can therefore be expected to be appropriate. But as shown in Chapter 2 when N_o / f is not large the slab model is no longer valid, and the variation of velocity with the height must be taken into account. The advantages of the vertically averaged model, when comparing with the slab model used by Manins (1982), are that the vertical distribution of velocity is included, and it need not be assumed that there is a velocity jump with linear distribution within the thin jump region. Note as well that convection due to surface heating does not play a role here.

5.1. Governing Equations.

The density in the interior is assumed to vary in both the horizontal and the vertical directions. That is, $\frac{\partial \rho_o}{\partial x'} = C_1 \neq 0$ and $\frac{\partial \rho_o}{\partial z'} = C_2 \neq 0$ where C_1 and C_2 are constants. A sketch showing the flow geometry and density field is given in Fig. 5.1.

The governing equations in the bottom coordinate system, in which the z-axis is perpendicular to the sea floor and the y-direction is the direction of the geostrophic velocity as shown in Fig. 5.1 are (Appendix 2):

$$\frac{\partial(\overline{u}h)}{\partial t} - f\overline{v}h = -\frac{1}{\rho_o}\tau_b{}^x - \frac{\epsilon g h \beta}{\rho_o} \tag{5.1}$$

$$\frac{\partial(\overline{v}h)}{\partial t} + f\overline{u}h = -\frac{1}{\rho_o}\tau_b{}^y \tag{5.2}$$

$$\frac{\partial(h\epsilon)}{\partial t} = -\frac{\tan\beta_1}{g}\rho_o N_o{}^2 \overline{u}h \tag{5.3}$$

$$\alpha' u_*{}^2 - (\overline{u}^2 + \overline{v}^2) + \frac{N_o{}^2 h^2}{2} + \frac{\epsilon g h}{\rho_o} - \frac{2h\alpha' C_d \overline{U} N_o{}^2 \tan\beta_1'}{f}$$

$$- \tan\beta_1' \left[\frac{N_o{}^2 \overline{v}h}{f} + \frac{N_o{}^4 h^2 \tan\beta_1'}{4f^2} \right] = 0, \tag{5.4}$$

where $\overline{U} = \sqrt{\overline{u}^2 + (\overline{v} + \overline{V}_g)^2}$ as before, and where

$$\tan\beta_1 = -\left[\frac{\partial \rho_o}{\partial x} \Big/ \frac{\partial \rho_o}{\partial z} \right] \tag{5.5a}$$

is the isopycnal slope relative to the sea floor, and

$$\tan\beta_1' = -\left[\frac{\partial \rho_o}{\partial x'} \Big/ \frac{\partial \rho_o}{\partial z'} \right] \tag{5.5b}$$

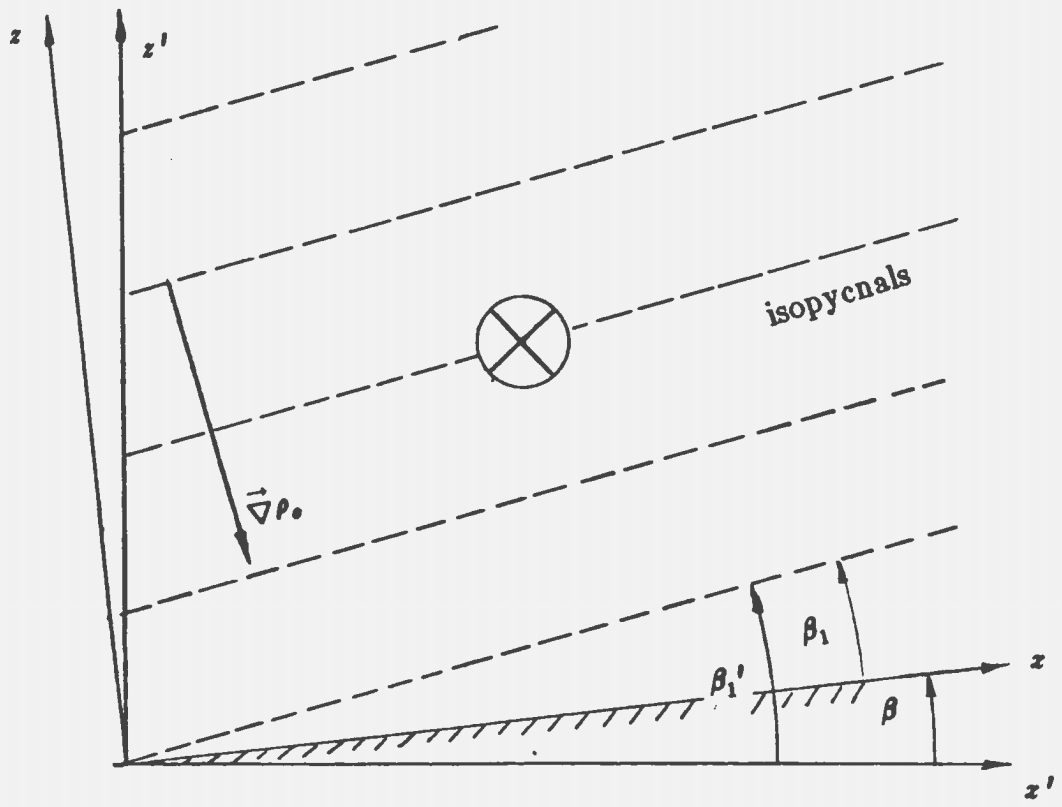

Figure 5.1. A sketch of a sloping bottom with horizontal density gradient.

is the isopycnal slope relative to the horizontal. Note that (see Fig. 5.1)

$$\beta_1' \equiv \beta_1 + \beta. \tag{5.5c}$$

The equations in a bottom coordinate system with geostrophic balance in the interior are (see Appendix 2)

$$-\rho_o f V_g(x, z) = -\frac{\partial P_o}{\partial x} - g\beta\rho_o(x, z) \tag{5.6a}$$

$$0 = \frac{\partial P_o}{\partial y} \tag{5.6b}$$

$$0 = \frac{\partial P_o}{\partial z} + \rho_o(x, z)g \tag{5.6c}$$

where the geostrophic velocity V_g varies only in the vertical direction but, in the bottom coordinate system, V_g is in general a function of both x and z. From Eqs. (5.6a), (5.6c) and (5.5a) the thermal wind relation can be deduced by using scale analysis:

$$VS \equiv \frac{\partial V_g}{\partial z} = -\frac{N_o^2 \tan\beta_1'}{f} \tag{5.7}$$

where VS is the vertical shear of geostrophic velocity. Thus the geostrophic velocity can be expressed as

$$V_g(x, z) = V_g(0, 0) + \beta x VS + z\ VS. \tag{5.8}$$

From the energy condition (5.4) h can be expressed in the form:

$$h = \frac{-B_1 + \sqrt{B_1^2 - 4A_1C_1}}{2A_1} \tag{5.9}$$

(the reasons for choosing the positive square root will be given) where

$$A_1 = \frac{N_o^2}{2}\left[1 - \frac{N_o^2}{2f^2}\tan^2\beta_1'\right] \tag{5.10}$$

$$B_1 = \frac{\epsilon g}{\rho_o} - \frac{N_o^2}{f}\tan\beta_1'(\bar{v} + 2C_g\alpha' U) \tag{5.11}$$

$$C_1 = \alpha' u_e^{\,2} - (\bar{u}^2 + \bar{v}^2). \tag{5.12}$$

Consider the gradient Richardson number in the interior:

$$R_i = \frac{N_o^{\,2}}{VS^2} \tag{5.13}$$

The flow in the interior is required to be stable. When $R_i \geq 1/2$, from Eqs. (5.7) and (5.13) it is seen that

$$\frac{N_o^{\,2}}{f^2}\tan^2\beta_1' \leq 2 \tag{5.14}$$

and therefore that $A_1 \geq 0$.

The reason for choosing the positive square root in Eq. (5.9) is therefore that because A_1 is positive, and C_1 is generally negative, the magnitude of the square root is greater than B_1. Choosing the positive sign ensures that h will be positive.

In the sloping bottom case because the geostrophic velocity depends on x, the along slope coordinate, as shown in Eq. (5.8). Therefore the thickness, and consequently the velocity vector and the advective density anomaly could also be expected to vary with x. But in Appendix 2 it is assumed, provided the bottom slope is small enough, that these quantities were all independent of x (as also assumed by Bird et al., 1982). How small must the bottom slope be? Examining Eq. (5.8) it is seen that the x-dependence may be ignored provided

$$\beta \ll h/x.$$

This is quite a stringent condition. For example if horizontal uniformity over scales of 100 h is required (1 km if $h = 10$ m), then β must be much less than 10^{-2} (0.6 degree).

The governing equations (5.1)-(5.4) were solved numerically in a way similar to that discussed in Chapter 4, with the same initial conditions and using the DGEAR routine in IMSL. That is, by using Eq. (5.9) to solve for h, then substituting h into Eqs. (5.1)-(5.3), these equations can be solved for the variables $\bar{u}$, $\bar{v}$ and ϵ. The same ramp function Eq. (4.9) with $V_g(0, 0)$ replacing 15 cm/s is used. The ramp period T_g is 48 hours, unless stated otherwise.

The results for a horizontal flat bottom and for a sloping flat bottom are presented separately in the next two subsections.

5.2. Results for a Horizontal Flat Bottom

For a horizontal flat bottom when thermal wind effects are included the mass conservation equation and energy equation are different from before. The main distinction is that ϵ is non-zero. The governing equations are Eqs. (5.1)-(5.4) with $\beta_1 = \beta_1'$ (see Appendix 2). It is assumed that $\beta_1' \ll 1$. For a given value of VS, $V_g(0, 0)$ was determined by setting $V_g = 15$ cm/s at $z = 20$ m based on Fig. 4.3. Test runs for the range of N_o from 10^{-3} to 10^{-2} /s, $f = 10^{-4}$ /s and values of VS in the range 10^{-2} to 10^{-4} /s showed no obvious difference for $\alpha' = 0.59$ or 6.3. This implies that the variations of α' are not important and the dependence of α' on $\frac{VS}{f}$ can be ignored when $\frac{N_o}{f}$ is large.

When $\frac{\partial V_g}{\partial z} > 0$, the thickness of the bottom mixed layer always increases with time. As an example, a 5-day's computation results are shown in Fig. 5.2. It was found that the greater the magnitude of the vertical shear, the larger the thickness. The veering angle decreased with increasing magnitude of VS. Therefore the tendency of the thermal wind effect is the same for the vertically-integrated model as obtained by Bird et al. (1982) using Level II turbulent closure. In the northern hemisphere ϵ is always less than zero in this case and increases in magnitude with time, because $\frac{\partial \rho_o}{\partial z} < 0$ and the transverse flow advects less dense water in the negative x-direction. This is therefore similar to the downwelling case for a sloping bottom presented in Chapter 4.

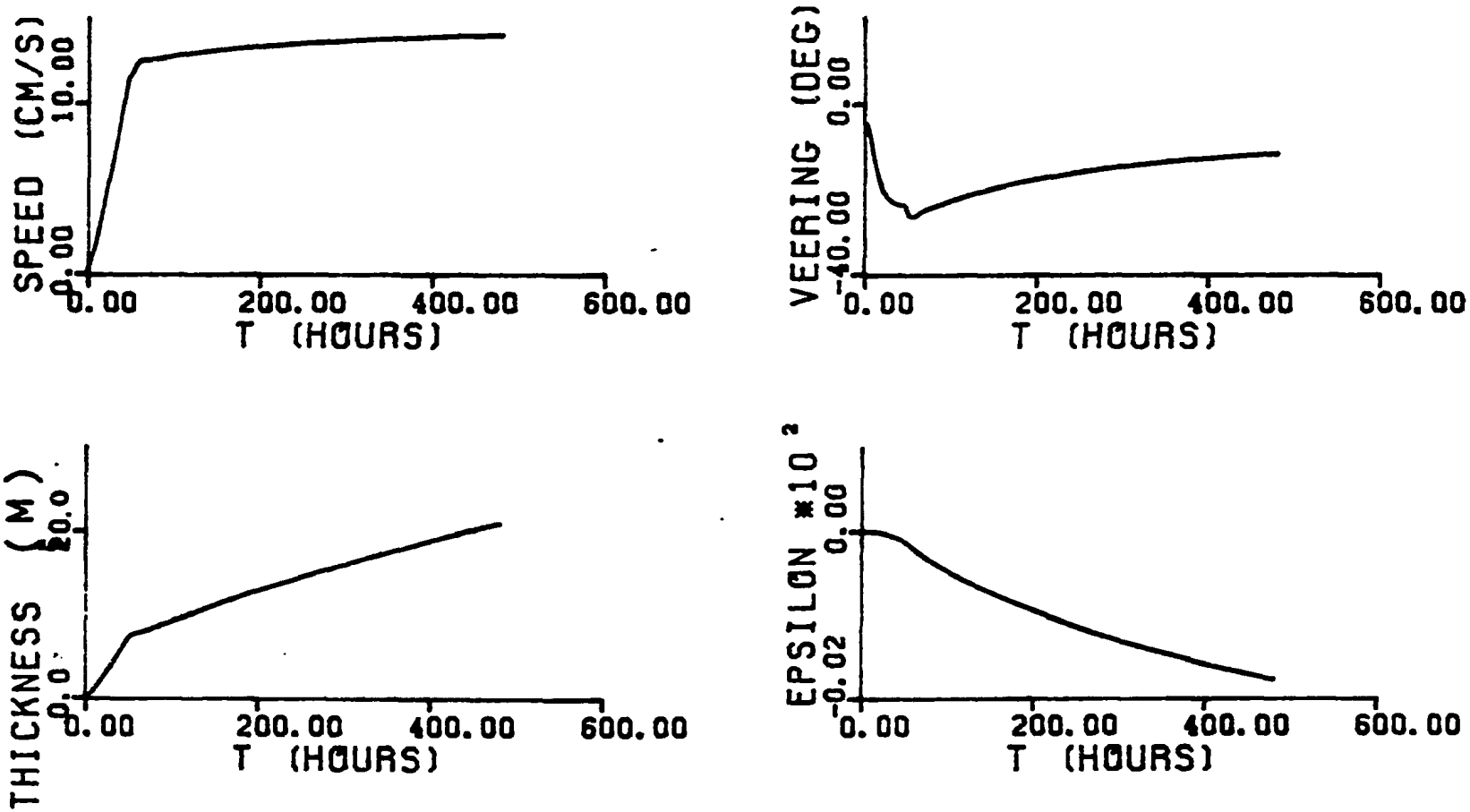

Figure 5.2. The time series of the thickness, speed, veering angle and ϵ (EPSILON) for a horizontal flat bottom with thermal wind (positive shear). The isopycnal slope is -0.26×10^{-3} which corresponds to a vertical shear of 0.68×10^{-4} /s. All other parameters are the same as in Fig. 4.6. The units of EPSILON are g/cm^3.

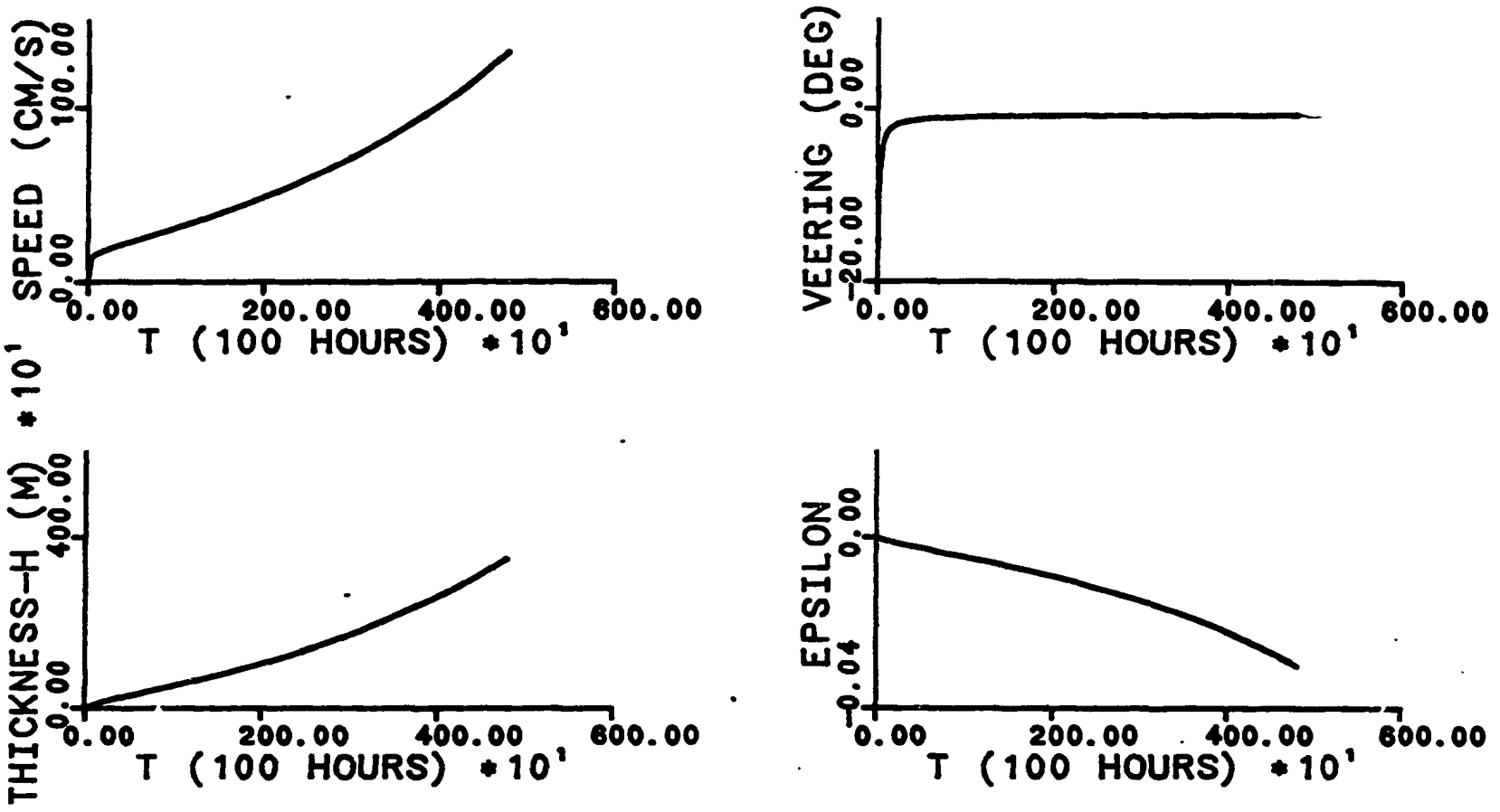

Figure 5.3. The 21.7-year time series of the thickness, speed, veering angle and ϵ (EPSILON) for a horizontal flat bottom with thermal wind (positive shear). The isopycnal slope is -0.26×10^{-3} which corresponds to a vertical shear of 0.68×10^{-3} /s. All other parameters are the same as in Fig. 4.6. The units of EPSILON are g/cm^3.

In order to make comparisons with the sloping bottom case without thermal wind the example given in Fig. 5.2 is for $\beta_1' = -0.26\times10^{-3}$, the negative of the bottom slope used in Fig. 4.6. All other parameters have the same values as in Fig. 4.6. Figure 5.2 shows that the results are almost the same as those in Fig. 4.6. Therefore at the initial stage (5 days) of bottom boundary layer development the horizontal density gradient in this case plays a role similar to that of bottom slope. But for a long period of bottom boundary layer development the effect of thermal wind is different from the effect of bottom slope. The thickness and the vertically averaged speed of the layer always increase with time. This can be seen in Fig. 5.3 for a case of 21.7-year's developing time in which all parameters are same as in Fig. 5.2.

When $\frac{\partial V_g}{\partial z} < 0$ (Fig. 5.4), the isopycnal slope is taken as 2.4×10^{-3}, the negative of the bottom slope used in Fig. 4.7. The 5-day simulation results show that in the northern hemisphere ϵ is always larger than zero because $\frac{\partial \rho_0}{\partial z} > 0$ and the transverse flow advects denser water in the negative x-direction. This corresponds to the upwelling case for a sloping bottom discussed in Chapter 4. Overshoot phenomena appear, as in the upwelling case for a sloping bottom and no thermal wind (Fig. 4.7). However, after the ramp period the thickness decreases continuously with time. This is very different from the corresponding sloping bottom case without thermal wind. The reason for this difference is that for a sloping bottom, when ϵ increases, the restoring force due to the component

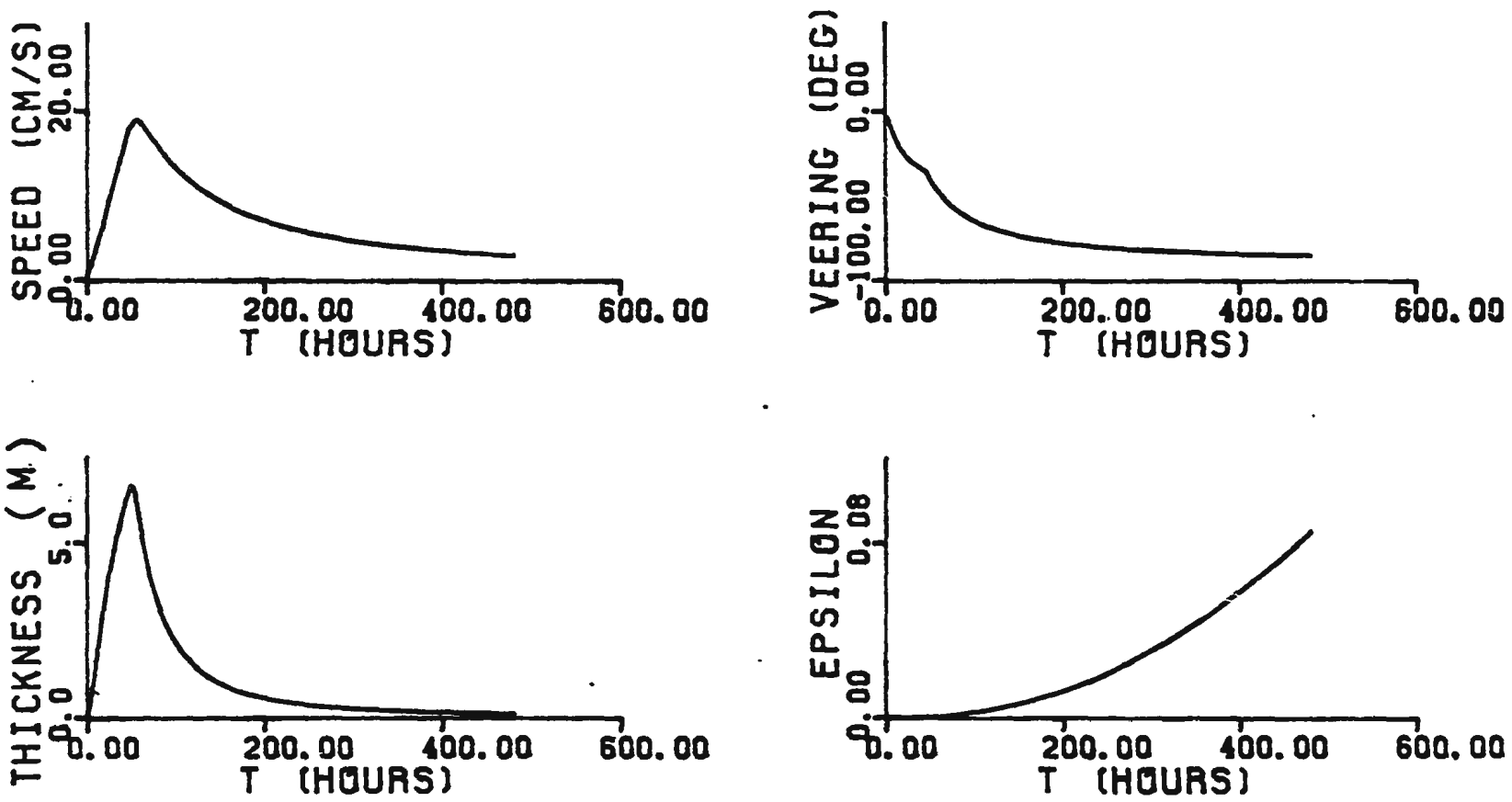

Figure 5.4. The time series of the thickness, speed, veering angle and ϵ (EPSILON) for a horizontal flat bottom with thermal wind (negative shear). The isopycnal slope is 2.4×10^{-3}. All other parameters are the same as in Fig. 4.6. Here the thickness is allowed to decrease. The units of EPSILON are g/cm^3.

of buoyancy parallel to the slope, $\frac{\epsilon g h \beta}{\rho_o}$ (Eqs. 5.1 and 3.46) increases to prevent the further increase of ϵ. For the flat horizontal bottom case with thermal wind, this term is not present (Eq. 5.1, with $\beta = 0$), and ϵ could increase indefinitely. Furthermore, if the thickness didn't decrease the potential energy term $\frac{\epsilon g h}{\rho_o}$ in the energy equation (5.4) caused by advection would increase to infinity. This is unphysical, and this term must have a limit. That is, $h\epsilon$ must have a limit.

Time series of $h\epsilon$, $h\bar{u}$, $h(V_g + \bar{v})$, $V_g + \bar{v}$ and $\bar{u}$ are shown in Fig. 5.5, in which HE stands for the product of $h\epsilon$, HU for $h\bar{u}$ and HV for $h(V_g + \bar{v})$. Fig. 5.5 shows that $h\epsilon$ approaches a constant value, and therefore the thickness must decrease due to the increase of ϵ. The y-component of vertically averaged velocity decreases much faster than the x-component of vertically averaged velocity. Therefore in the asympototic sense it can be assumed that $V_g + \bar{v} = 0$. Then from Eq. (5.2)

$$\frac{\partial h}{\partial t} = \frac{fh}{V_g}\bar{u} < 0$$

is obtained. The equation above shows that the thickness must decrease with time in this limit.

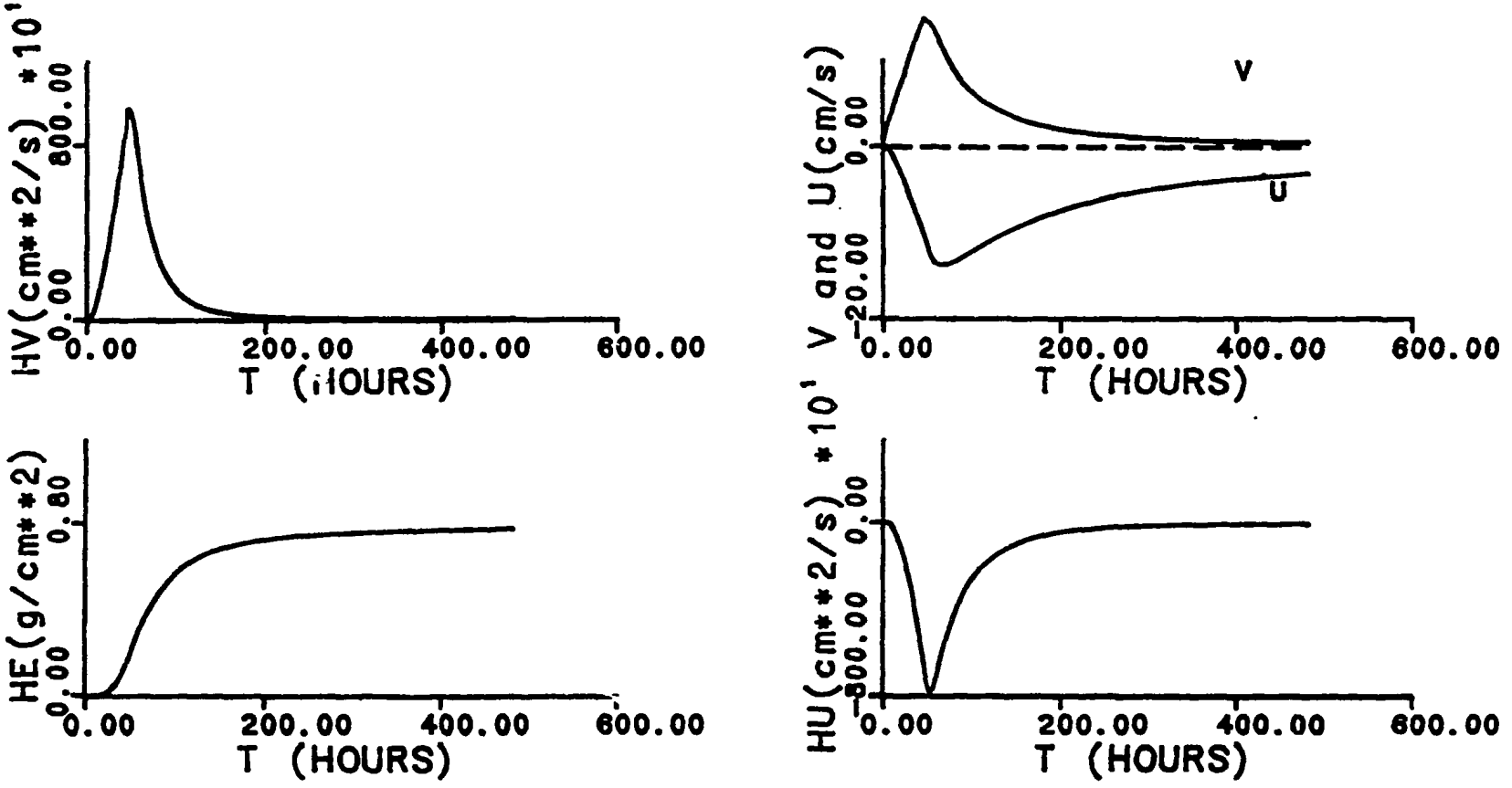

Figure 5.5. The time series of $h\epsilon$, $h\bar{u}$, $h(V_g + \bar{v})$, $V_g + \bar{v}$ and $\bar{u}$. The isopycnal slope is taken as 2.4×10^{-3}. HE stands for the product of $h\epsilon$, HU for $h\bar{u}$, HV for $h(V_g + \bar{v})$, V for the y-component of vertically averaged velocity and U for the x-component of vertically averaged velocity.

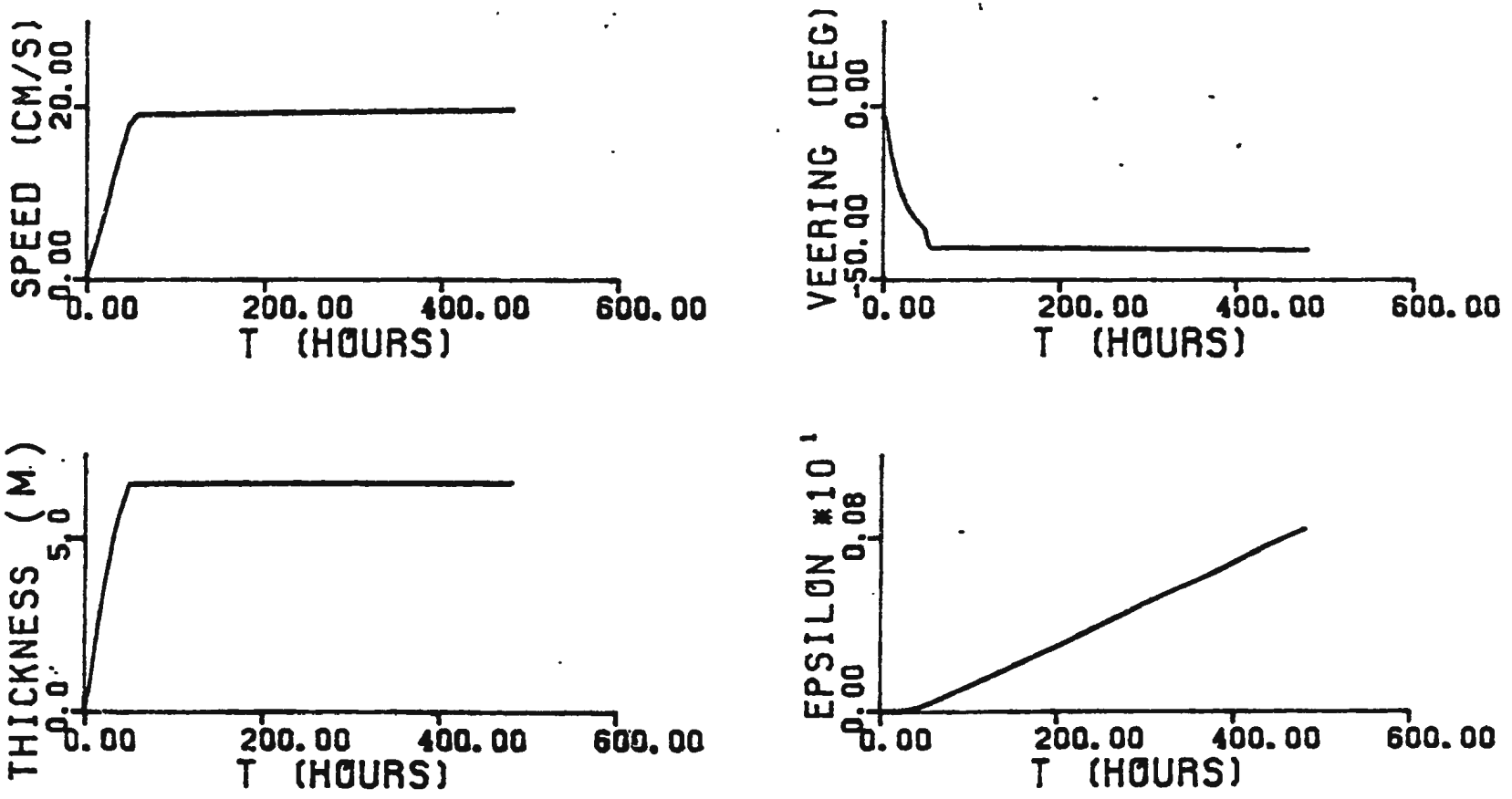

Figure 5.6. The time series of the thickness, speed, veering angle and ϵ (EPSILON) when the unmixing is not allowed for the same case as in Fig. 5.4. The units of EPSILON are g/cm^3.

The results when unmixing is not allowed are shown in Fig. 5.6. Note that in Fig. 5.6 not only is the thickness constant (about 6.7 m), the speed and veering angle are also constant: 19.3 cm/s and –41 degrees respectively. Only the advective density anomaly increases with time but at a much smaller rate (one order of magnitude smaller) than the rate in Fig. 5.4. These are different from the results for the negative bottom slope without thermal wind presented in Fig. 4.8.

Finally, time series of $h\epsilon$, $h\bar{u}$, $h(V_g + \bar{v})$, $V_g + \bar{v}$ and $\bar{u}$ for the first case in this section ($\frac{\partial V_g}{\partial z} > 0$, Fig. 5.2), when the isopycnal slope is taken as -0.26×10^{-3}, are shown in Fig. 5.7. Comparing this figure with Fig. 5.5 the results, when the isopycnal slope is negative, are quite different: the $h(V_g + \bar{v})$ and magnitude of $h\epsilon$ increase with time, and contrary to the case in Fig. 5.5 the magnitude of y-component of vertically averaged velocity increases with time while the magnitude of x-component of vertically averaged velocity decreases with time. The reason for these differences is that when the isopycnal slope is negative the potential energy term $\frac{\epsilon g h}{\rho_o}$ in the energy equation (5.4) always decreases (negative ϵ) so that the thickness can increase as shown in Fig. (5.2). When the thickness increases more kinetic energy is entrained into the mixed layer from the geostrophic flow above and the y-component of vertically averaged velocity of the mixed layer also increases.

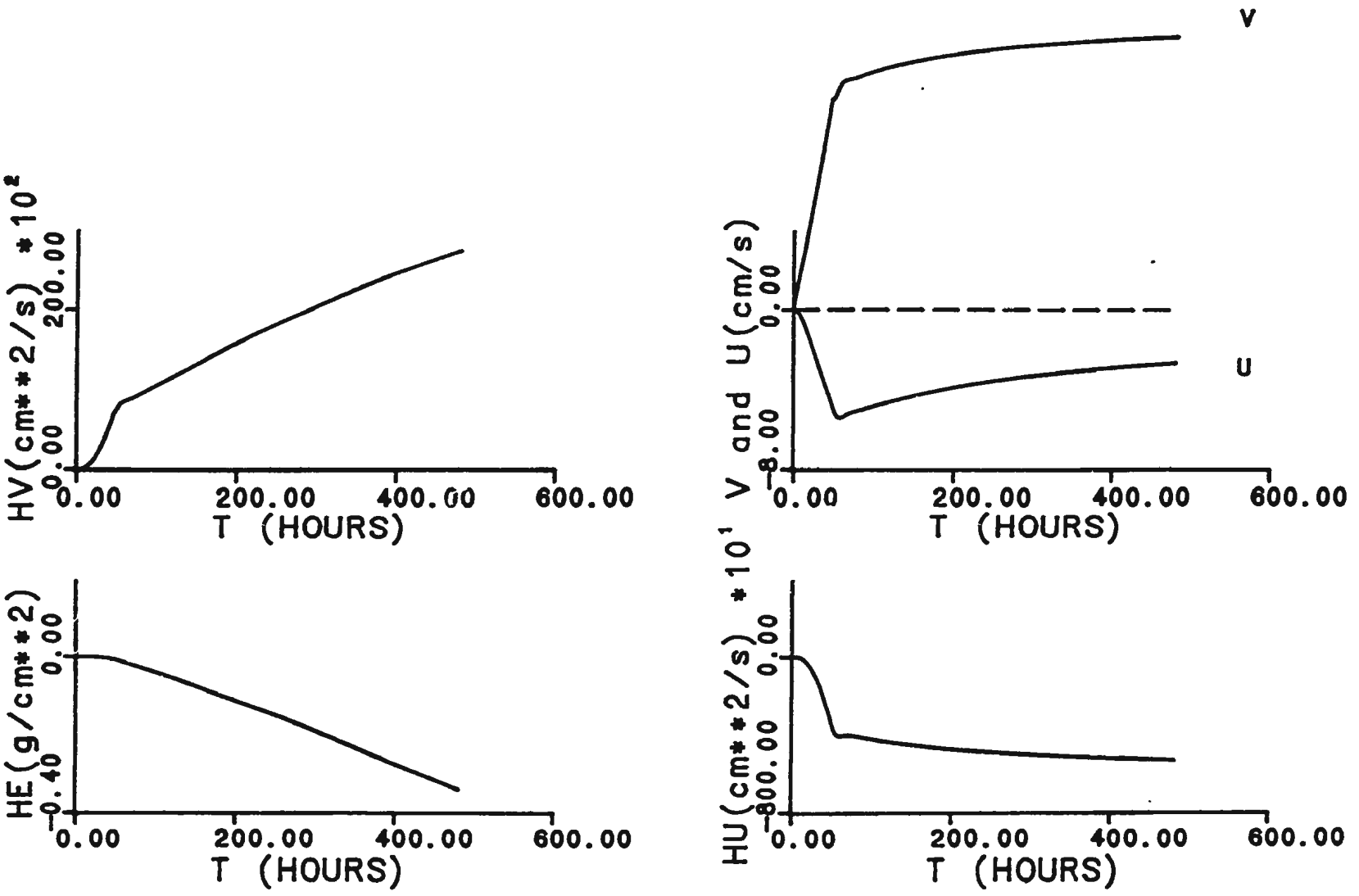

Figure 5.7. The time series of $h\epsilon$, $h\bar{u}$, $h(V_g + \bar{v})$, $V_g + \bar{v}$ and $\bar{u}$. The isopycnal slope is taken as -0.26×10^{-3}. HE stands for the product of $h\epsilon$, HU for $h\bar{u}$, HV for $h(V_g + \bar{v})$, V for the y-component of vertically averaged velocity and U for the x-component of vertically averaged velocity.

5.3. Results for a Sloping Flat Bottom

When comparing the governing equations (3.46)-(3.49) for mixed layer growth over a sloping flat bottom without thermal wind with Eqs. (5.1)-(5.4) including thermal wind, it is found that the differences are in the last two equations: the mass conservation equation and the energy equation. The bottom slope β in the mass conservation equation (3.48) has been replaced by $-\beta_1$, the negative isopycnal slope relative to the bottom (Fig. 5.1) in Eq. (5.3), and there are three extra terms involving the isopycnal slope in the energy equation (5.4). Three special cases are discussed.

5.3.1. Isopycnals parallel to the bottom ($\beta_1 = 0$)

When the isopycnals are parallel to the bottom $\beta_1 = 0$ and Equation (5.3) becomes

$$\frac{\partial(h\epsilon)}{\partial t} = 0 \tag{5.15}$$

which is the same as for a horizontal flat bottom with no thermal wind: that is, $\epsilon = 0$. This was confirmed in numerical experiments. It implies that the thermal wind and bottom slope cancel each other. For example, with $\beta = 0.26\times10^{-3} = \beta_1'$, and the other parameters the same as in Fig. 4.6, results are obtained (Fig. 5.8) which are very similar to those in Fig. 4.1.

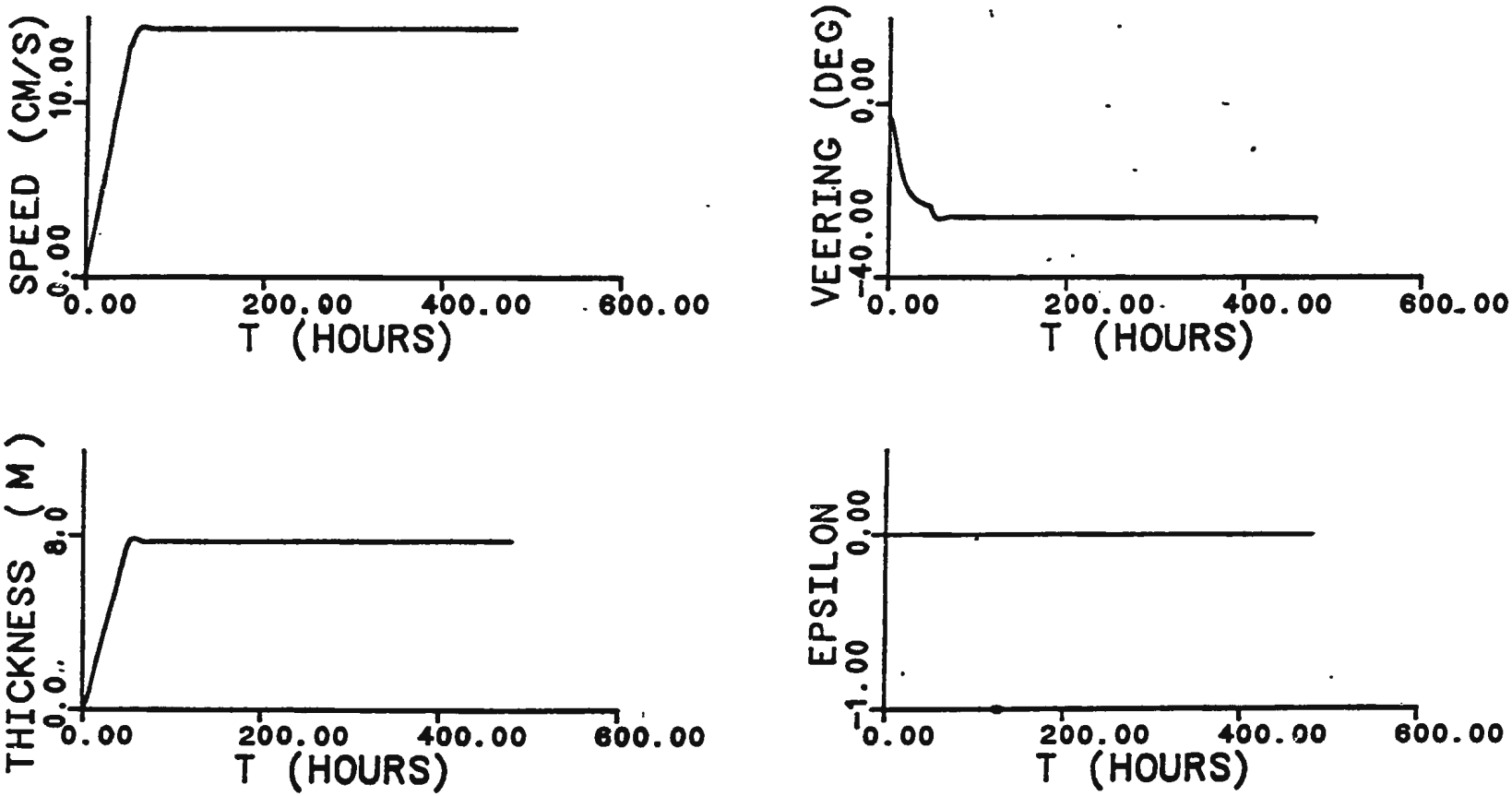

Figure 5.8. The time series of the thickness, speed, veering angle and ϵ (EPSILON) with equal bottom slope and isopycnal slope: $\beta_1' = \beta = 0.26 \times 10^{-3}$. All other parameters are the same as in Fig. 4.6. The units of EPSILON are g/cm^3.

5.3.2. Growth dominated by bottom slope ($\beta >> \beta_1'$)

When $\beta >> \beta_1'$ it is seen from Eq. (5.5c) that

$$-\beta_1 \approx \beta.$$

This implies that the bottom slope dominates the mass conservation equation. From numerical experiments for this case it is found that the two terms involving β_1' in the energy equation did not affect the flow very much, which is not surprising since $\beta_1' << \beta$ and thus $\beta_1' << 1$. Therefore the bottom mixed layer growth has basically the same features as the sloping bottom case without thermal wind.

5.3.3. Growth dominated by thermal wind ($\beta << \beta_1'$)

When $\beta << \beta_1'$, Eq. (5.5c) becomes approximately

$$\beta_1' \approx \beta_1.$$

This implies that the vertical shear dominates the mass conservation equation, and the two terms involving β_1' in the energy equation become important. The bottom slope loses its importance. The numerical experiments showed that the results were very similar to that for a horizontal flat bottom with thermal wind. For example no matter what sign β has the sign of ϵ depends only on the sign of VS.

5.4. Comparisons with Observations and Level II Model Results.

5.4.1. Comparisons with the observations made by Weatherly and Van Leer and Weatherly and Martin's model results

The model results including thermal wind effects are again compared with the observations made by Weatherly and Van Leer (1977) on the western Florida Continental Shelf.

During northward interior flow the value of VS estimated from the velocity profiles (Figs. 4.3a and b) is -2.0×10^{-3} /s. From the density field in Fig. 4.2 the estimated horizontal density gradient over the shelf is $\frac{1}{\rho_o}\frac{\partial \rho_o}{\partial z'} = 0.94\times10^{-8}$ /m giving, therefore,

$$VS = \frac{\partial V_g}{\partial z'} = -\frac{g}{f\,\rho_o}\frac{\partial \rho_o}{\partial z'} = -1.5\times10^{-3}/s\,.$$

These two estimates of the thermal wind shear are thus roughly the same, even though the data presented in Fig. 4.2 were taken on 2 June 1972, four years earlier than those in Fig. 4.3 (3 to 5 July 1976). During southward interior flow the vertical shear in the interior is of opposite sign and is estimated to be 2.0×10^{-3}/s (Fig. 4.3d).

The bottom slopes are still taken as $\beta = 0.26\times10^{-3}$ during northward interior flow, and $\beta = -2.4\times10^{-3}$ during southward interior flow, which are the values used by Weatherly and Martin (1978). The time series of thickness, ϵ, speed and veering angle obtained from the vertically integrated model with thermal wind

are presented in Figs. (5.9) to (5.15). As in the previous section, $V_g(0, 0)$ was determined for a given value of VS by setting $V_g = 15$ cm/s at $z = 20$ m. Both values of α' (0.59 and 6.3) were used but the results were very similar.

During northward interior flow, corresponding to the downwelling case, the parameters are: $N_o = 1.28\times10^{-2}$/s, $f = 0.63\times10^{-4}$/s, $VS = -2.0\times10^{-3}$/s and $\beta = 0.26\times10^{-3}$. Therefore from Eq. (5.7)

$$\beta_1' = -\frac{VSf}{N_o^2} = 0.77\times10^{-3}.$$

and thus the magnitude of β_1' exceeds β, and the mixed layer growth should depend mainly on the thermal wind. Because VS is negative as pointed out in Section 5.2 the thickness will decrease with time if unmixing is not inhibited. The results are shown in Fig. 5.9, which is similar to Fig. 5.4 for a horizontal flat bottom with negative vertical shear. From Fig. 5.9 it can be seen that the maximum thickness is 7.8 m. When "unmixing" is inhibited (Fig. 5.10) the thickness is 7.8 m, as compared to the 6.0 m observed, and the veering angle is 32° (from $t = 55$ h to $t = 159$ h), comparable to the observed value 30°.

Because VS is negative and the isopycnal slope is larger than the magnitude of the bottom slope ($\beta_1' > \beta$) ϵ increases with time after 45 hours. If the density is dominated by temperature, then this implies a decrease in temperature with time, contradictory to the observations of Weatherly and Van Leer (1977) during northward flow. The reason for this may be related to the choice of bottom slope. The station is located where the slope is 2.4×10^{-3}, but following Weatherly and

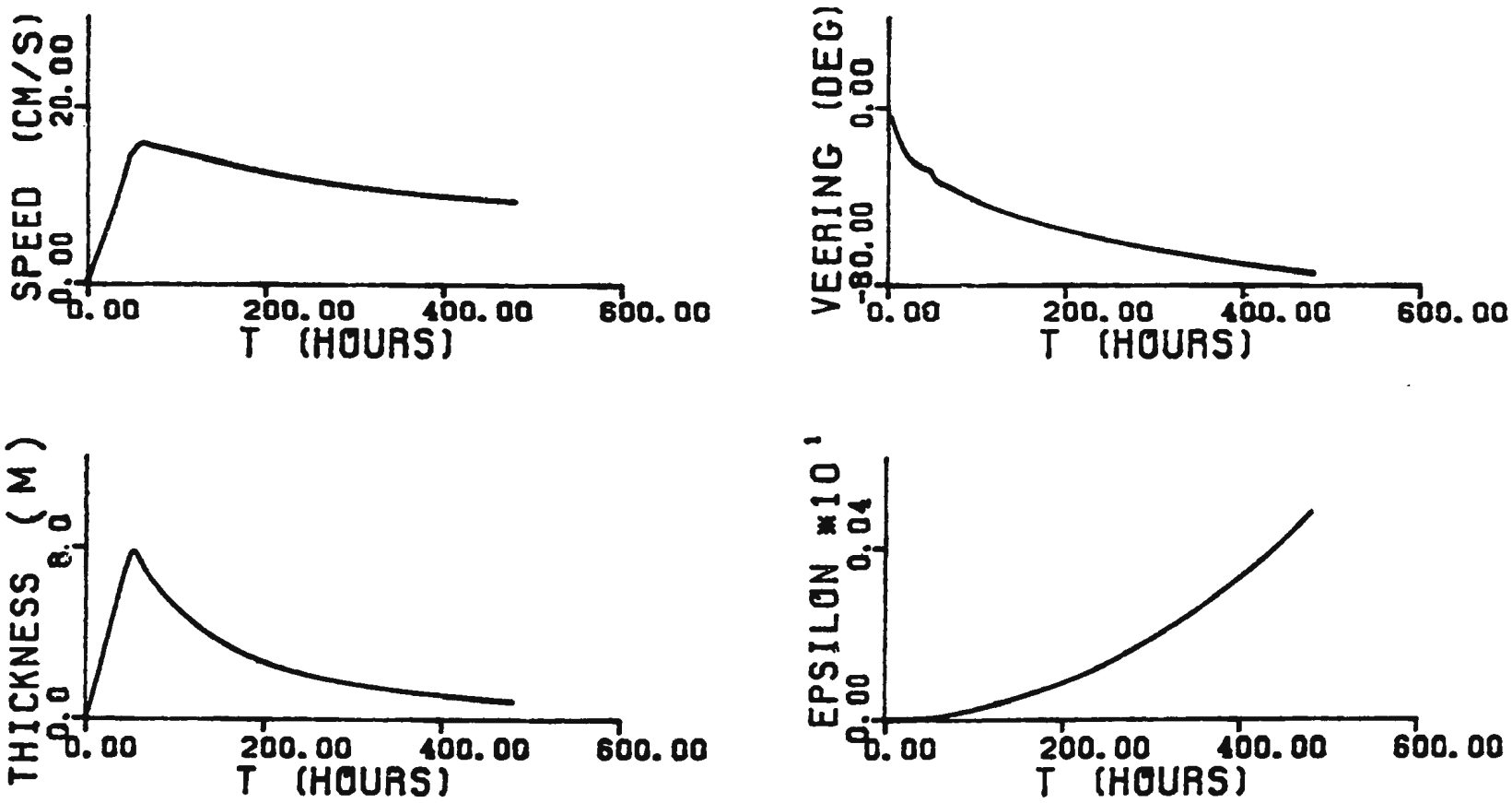

Figure 5.9. Time series of thickness, speed, veering angle and ϵ (EPSILON) during the growth of the bottom mixed layer on a sloping flat bottom, with negative vertical shear and positive bottom slope. Unmixing is not inhibited. $VS = -2.0\times10^{-3}$ /s, $\beta = 0.26\times10^{-3}$, $\beta_1' = 0.77\times10^{-3}$ and all other parameter values are the same as in Fig. 4.6. The units of EPSILON are g/cm^3. Compare to Fig. 4.6, the downwelling case with no thermal wind.

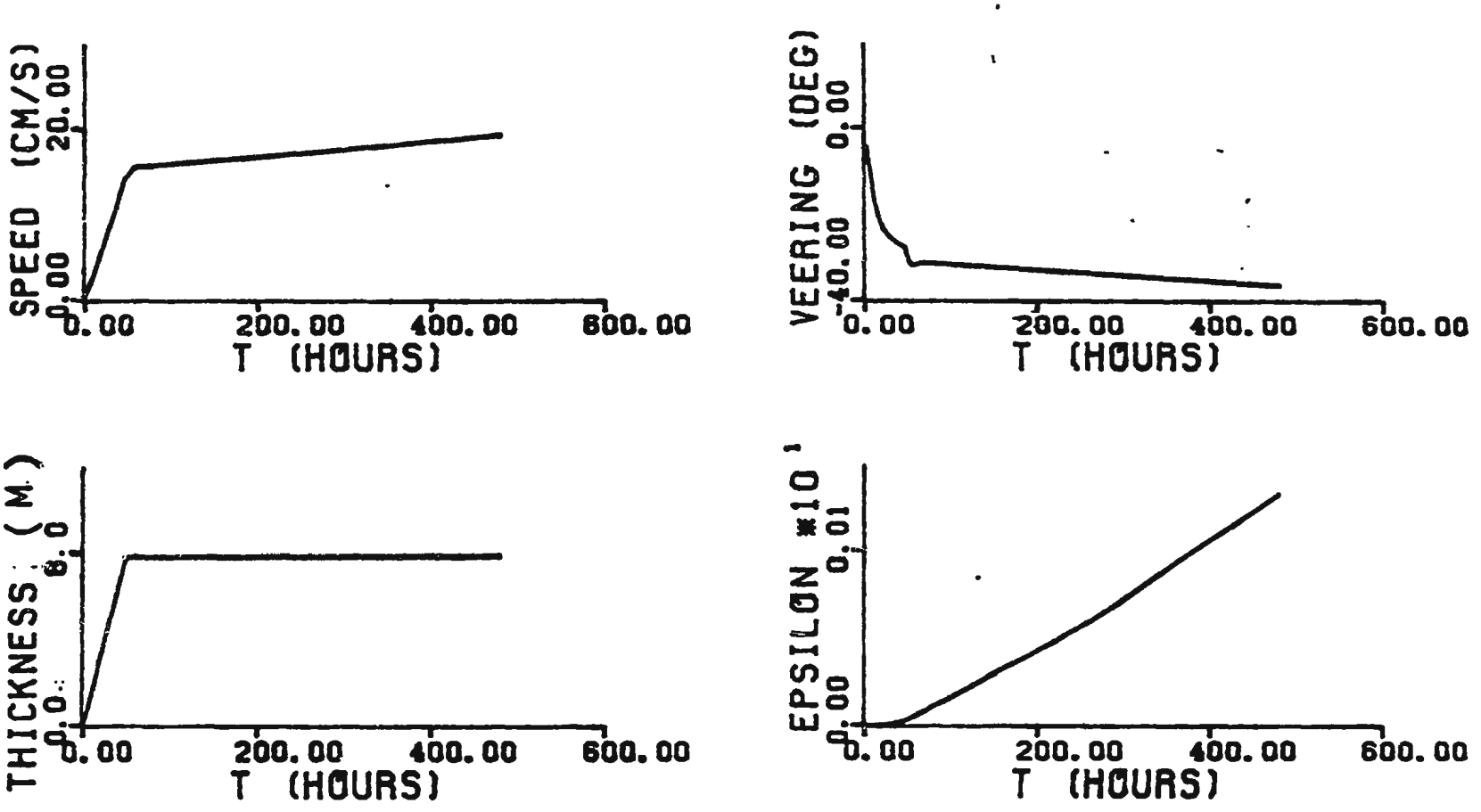

Figure 5.10. Time series of thickness, speed, veering angle and ϵ (EPSILON) during the growth of the bottom mixed layer on a sloping flat bottom, with negative vertical shear and positive bottom slope. Unmixing is inhibited. All parameters are the same as in Fig. 5.9. The units of EPSILON are g/cm^3. Compare to Fig. 4.6, the downwelling case with no thermal wind.

Martin (1978) the smaller value (0.26×10^{-3}) has been used, as explained in Chapter 4. This value may be too small. If a tangent to the bottom is drawn on the shallower side passing through the station (see Fig. 4.2) $\beta = 0.8\times10^{-3}$. This is comparable to β_1'. The results for this case are presented in Figs. 5.11 and 5.12. In Fig. 5.11 unmixing is allowed to occur. It can be seen that the thickness reaches a local maximum of 9.2 m at $t = 59$ h, decreases until $t = 70$ h, and then increases but more slowly than in Fig. 4.6, and is thus in better agreement with the observations on the western Florida Continental Shelf made by Weatherly and Van Leer, which show that the thickness does not increase with time. When unmixing is not allowed (Fig. 5.12), the differences are small. The thickness is about 9.2 m in contrast to the observed value of 6 m. The veering angle is about 28° (from $t = 52$ h to $t = 180$ h) compared to the observed value 30°. The time series of temperature is given in Fig. 5.13. The temperature increases monotonically with time, but at a rate slower than the equivalent (downwelling) case in Fig. 4.5, and the thickness no longer increases indefinitely with time.

These results are summarized together with the observations in Table 5.1. Comparing Table 5.1 with the downwelling case values in Table 4.2, it is seen that the vertically-integrated model results including thermal wind are in better agreement with observation than those obtained from the Level II and the vertically integrated model without considering thermal wind. In particular, the predicted thickness has become constant as observed.

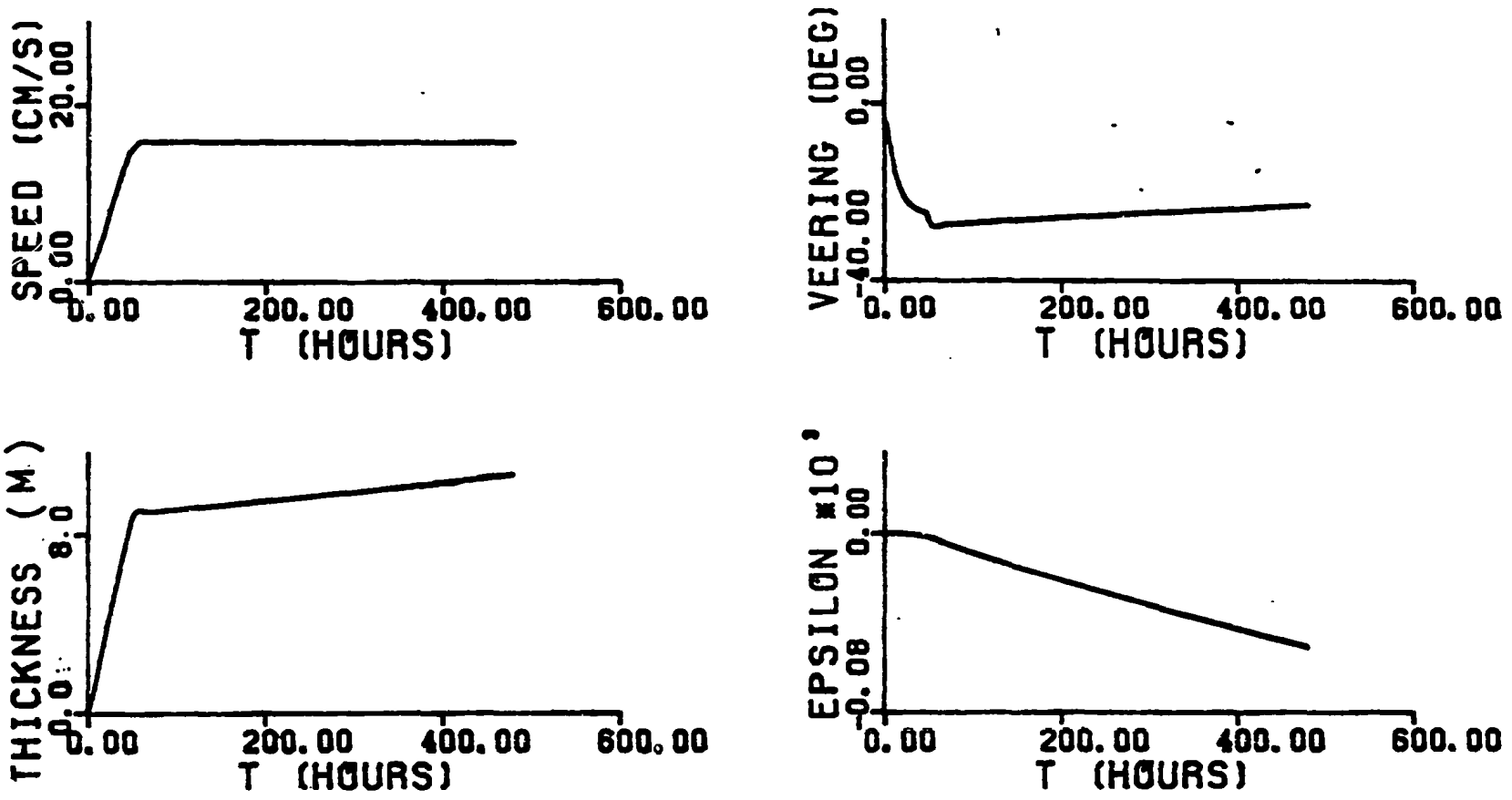

Figure 5.11. Time series of thickness, speed, veering angle and ϵ (EPSILON) during the growth of the bottom mixed layer on a sloping flat bottom, with negative vertical shear and positive bottom slope. Unmixing is not inhibited. $\beta = 0.8 \times 10^{-5}$. All other parameter values are the same as in Fig. 5.9. The units of EPSILON are g/cm^3. Compare to Fig. 4.6, the downwelling case with no thermal wind and smaller slope ($\beta = 0.26 \times 10^{-5}$).

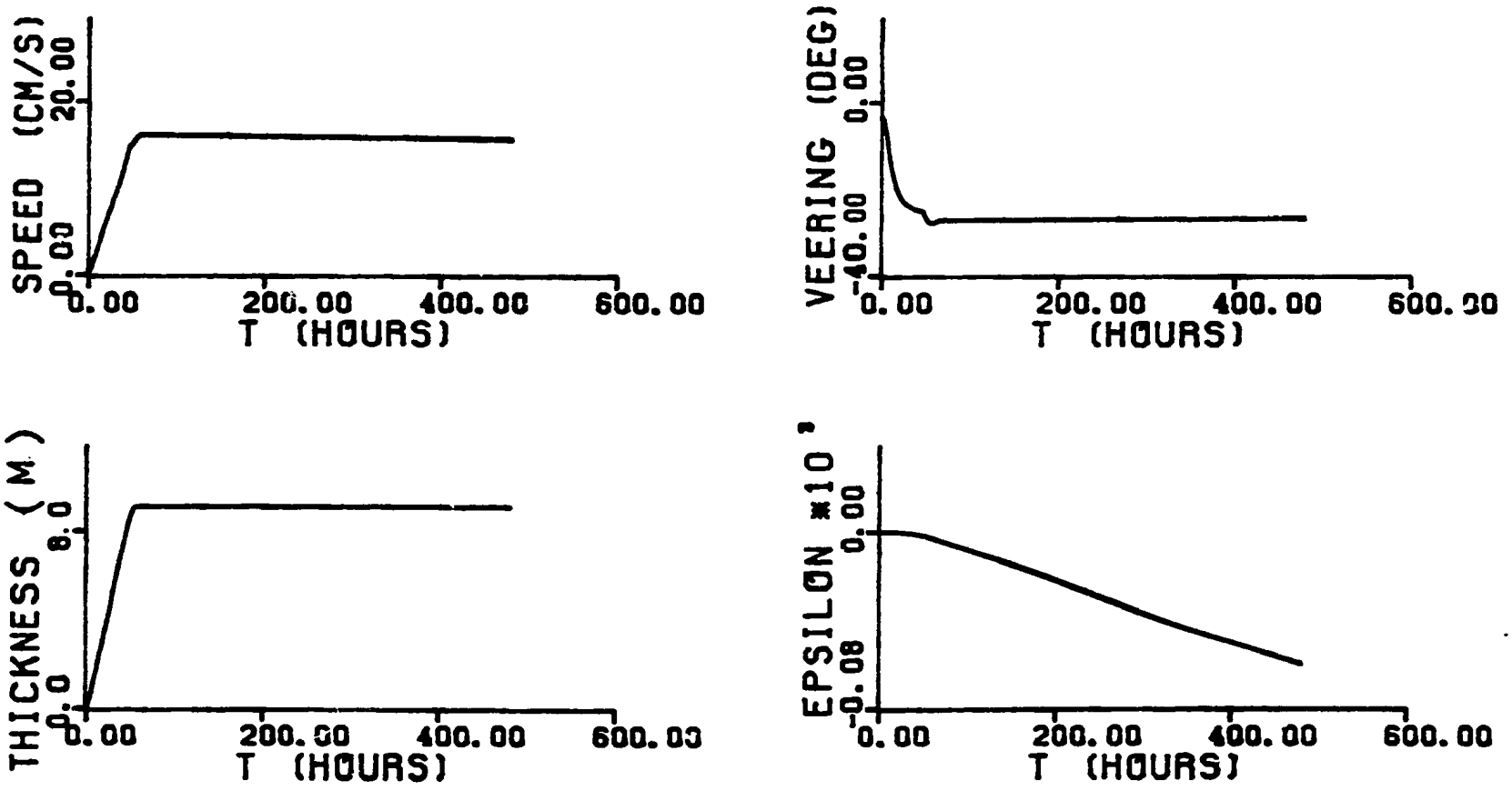

Figure 5.12. The time series of thickness, speed, veering angle and ϵ (EPSILON) during the growth of the bottom mixed layer on a sloping flat bottom, with negative vertical shear and positive bottom slope. Unmixing is inhibited. All parameter values used here are the same as in Fig. 5.11. The units of EPSILON are g/cm^3. Compare to Fig. 4.6.

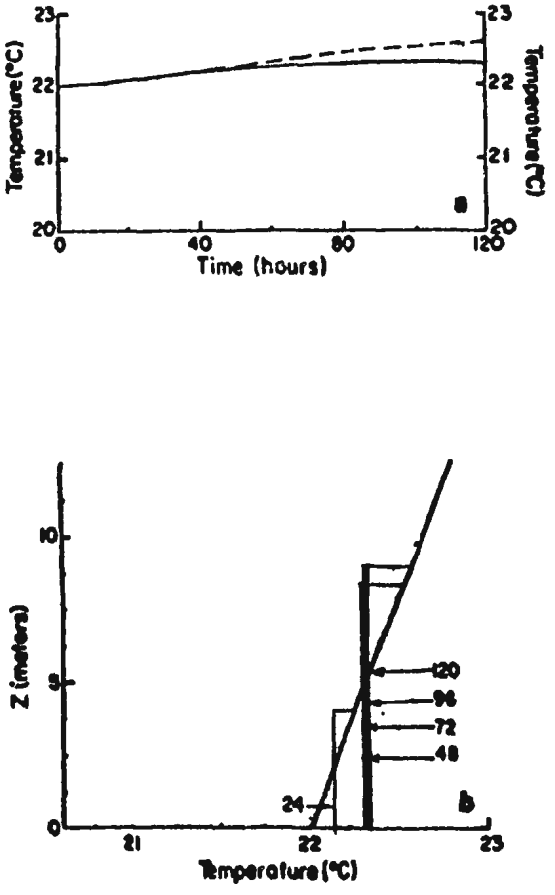

Figure 5.13. Time series (a) of the temperature of the bottom mixed layer and temperature profiles (b) at times 0, 24, 48, 72, 96 and 120 h for the case $\beta = 0.8\times10^{-3}$, $N_0 = 1.28\times10^{-2}$ /s, $VS = -2.0\times10^{-3}$ /s, $f = 0.63\times10^{-4}$ /s, and geostrophic velocity at height 20 m above the bottom is 15 cm/s and northward. The dashed curve in (a) shows the result from Fig. 4.5a with no thermal wind.

model	Vertically Integrated		Observations	
case	downwelling	upwelling	downwelling	upwelling
h (m)	9.2	5.2	6	11
T (°C)	22.4	21.3	22.8	18.9
α (degrees)	-28	-29	-30	-75
$\bar{U}$ (cm/s)	16.0	6.1	20.0	4.6

Table 5.1. The values of thickness h, temperature T, veering angle α and speed $\bar{U}$ in the mixed layer obtained from the vertically integrated model when including thermal wind for the runs in Figures 5.12 and 5.15. The observed values are the same as in Table 4.2.

When the interior flow is southward, corresponding to the upwelling case, $N_o = 1.28\times10^{-2}$/s, $VS = 2.0\times10^{-3}$/s, $f = 0.63\times10^{-4}$/s and $\beta = -2.4\times10^{-3}$. Therefore from Eq. (5.7)

$$\beta_1' = \frac{VSf}{N_o^2} = -0.77\times10^{-3}.$$

Thus the magnitude of β_1' is less than the magnitude of β, and the growth of the mixed layer should depend mainly on the bottom slope. The results are shown in Figs. 5.14 and 5.15. In Fig. 5.14 unmixing is allowed to occur and overshoot appears in the time series of thickness at $t = 50$ h. In Fig. 5.15 unmixing is not allowed. When Figs. 5.14 and 5.15 are respectively compared with Figs. 4.7 and 4.8, the upwelling case without thermal wind, the differences are small. The thickness in Fig. 5.15 is 5.2 m, compared to 4.6 m in Fig. 4.8. The maximum veering angle is 29° reached at $t = 54$ h, one hour later than the results in Fig. 4.8.

5.4.2. Comparisons with the results of Bird et al.

Using the Level II turbulent closure model including thermal wind, Bird et al. (1982) simulated observations made on the Eastward Scarp of the Bermuda Rise in a water depth of 4620 m. The velocity time series were recorded by four vector averaging current meters (VACMs) positioned at 0.8, 6.9, 12, 62 m above the bottom from September 1978 through April 1979. A 5-day section of the data in September 1978 was used for comparison with the simulations. The averaged geostrophic speed at 62 m above the bottom over the 5-day section was 18.92

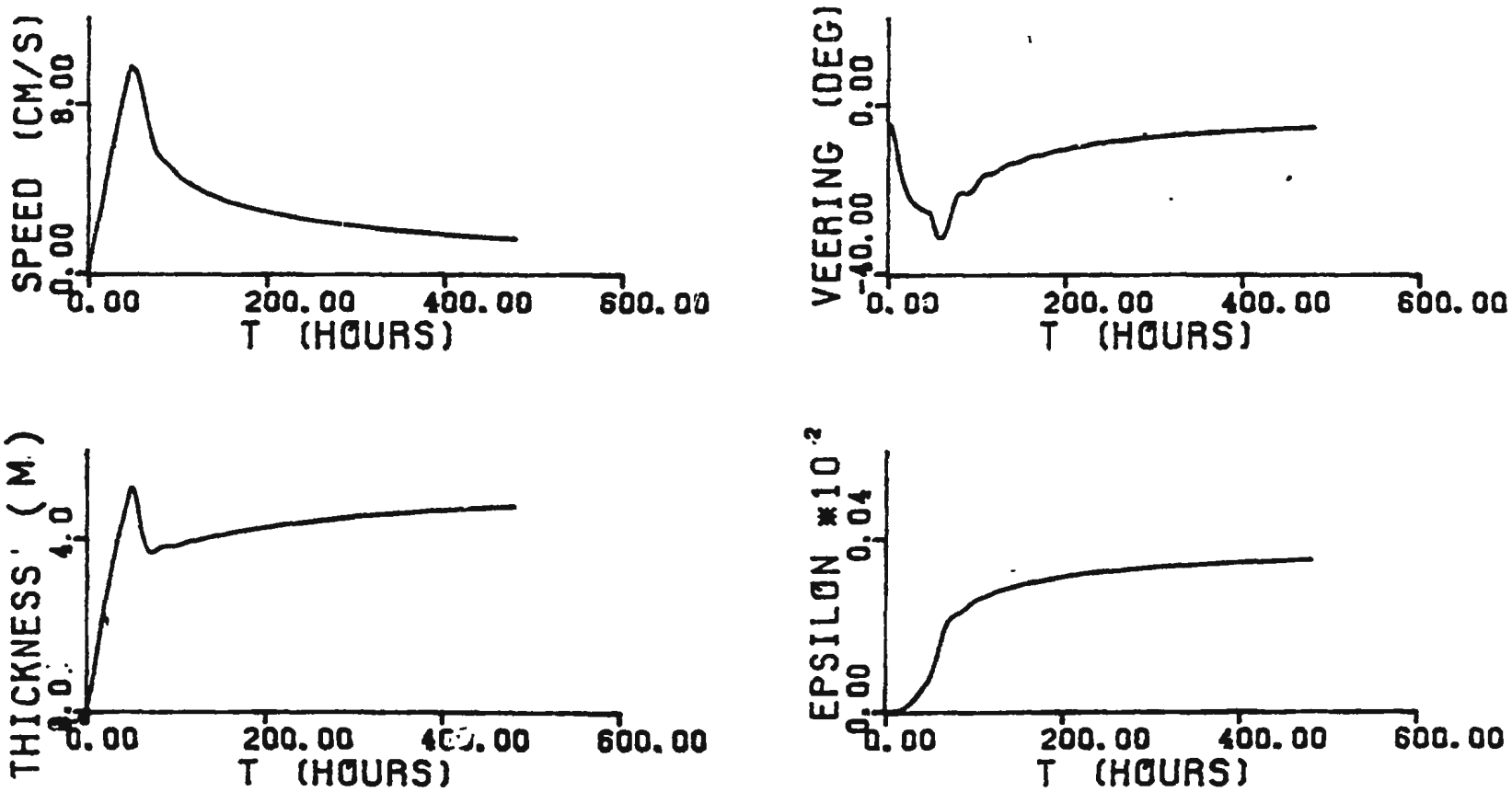

Figure 5.14. The time series of thickness, speed, veering angle and ϵ (EPSILON) during the growth of the bottom mixed layer on a sloping flat bottom, with positive vertical shear and negative bottom slope. $\beta = -0.24\times10^{-3}$, $VS = 2.0\times10^{-3}$ /s $\beta_1' = -0.8\times10^{-3}$. All other parameters are the same as in Fig. 4.7. Unmixing is not inhibited. The units of EPSILON are g/cm^3. Compare to Fig. 4.7, the upwelling case without thermal wind.

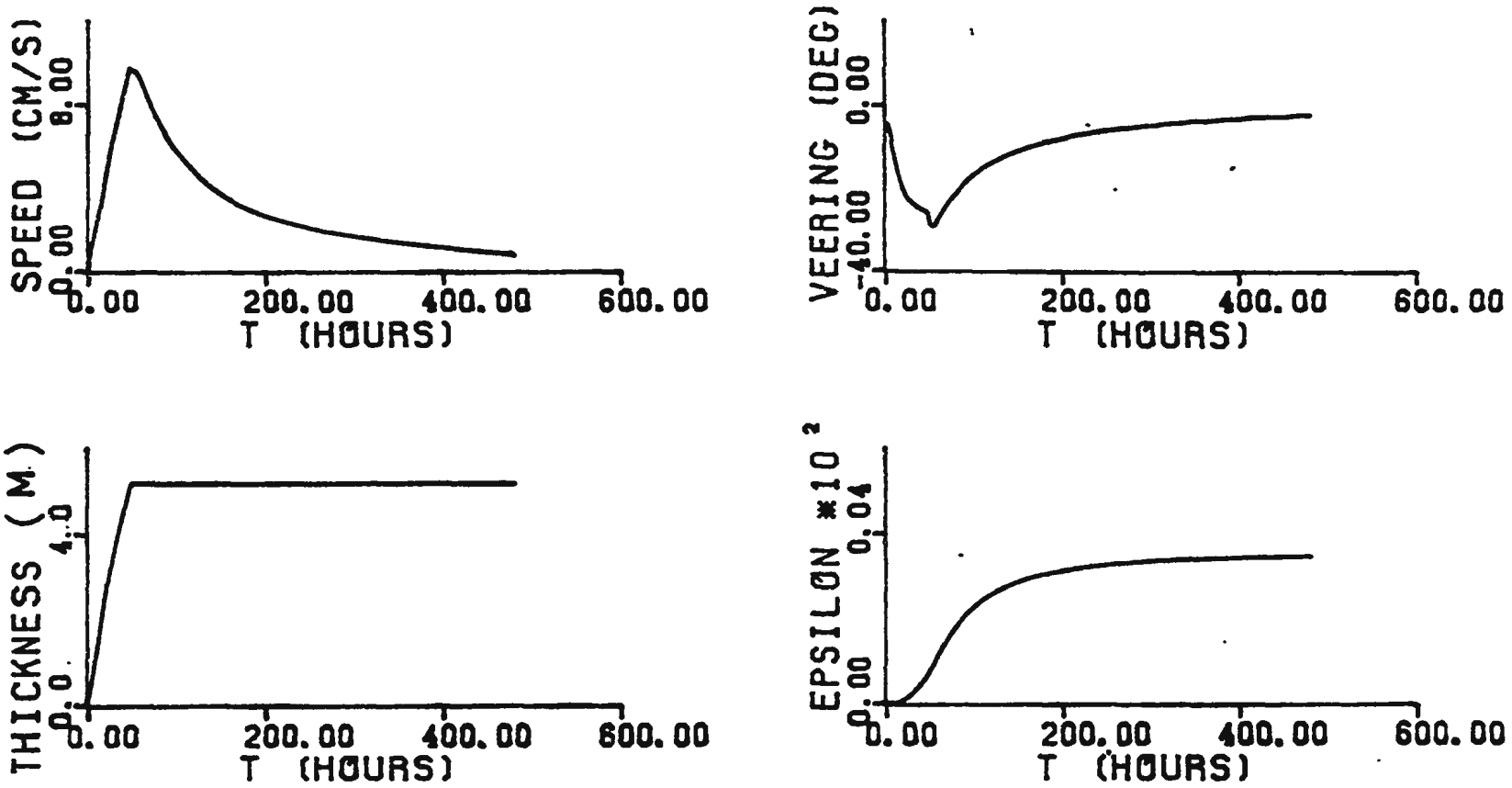

Figure 5.15. The time series of thickness, speed, veering angle and ϵ (EPSILON) during the growth of the bottom mixed layer on a sloping flat bottom, with positive vertical shear and negative bottom slope. Unmixing is inhibited. All parameters are the same as in Fig. 5.14. The units of EPSILON are g/cm^3. Compare to Figs. 4.7 and 5.14.

cm/s. The y-direction was always taken in the direction of the geostrophic velocity, and in this coordinate system the bottom slope β was positive and equal to 0.035: that is, this is a downwelling case. The Brunt-Vaisala frequency 7×10^{-5} /s was estimated from potential temperature profiles obtained at the time of deployment and the potential temperature-salinity relation for the area. The Coriolis parameter $f = 8\times10^{-5}$/s. Based on the VACM temperature data they inferred that during the 5-day period the thickness of the mixed layer was between 12-62 m, and the observed veering angle was 4.6 degrees (Table 5.2). The isopycnal slope was not available.

When the geostrophic velocity is 18.92 cm/s the estimated thickness from Weatherly and Martin's formula Eq. (1.4) is 92.9 m. When the bottom slope and thermal wind are excluded the analytic and numerical results from the vertically integrated model are given in Table 4.1 (run 382 and 383). It shows that the thickness is about 37 m and the veering angle is -5.8 degrees when velocity profile coefficient $\alpha' = 6.3$, and that the thickness is about 93 m and the veering is about -2.3 degrees when $\alpha' = 0.59$. The results for $\alpha' = 6.3$ are in better agreement with the observations.

Because the isopycnal slope was not available Bird et al. (1982) assumed isopycnal slopes such that $\beta_1 = 0, -0.01, -0.035$ in order to make thermal wind sensitivity tests. Here the same values of β_1 are used and the velocity profile coefficient α' is set equal to 6.3. Using the above values of β_1, the corresponding values of β_1' and VS can be calculated, and then $V_g(0,0)$ can be obtained from the

Comparison	Observation	Computed from Vertically Integrated Model (Level II Model)		
		$\beta_t = 0$	-0.01	-0.035
V_g cm/s	18.92			
u_* cm/s	0.7			
h (m)	41	78.7(36.7)	80.0(36.7)	82.0(90.4)
α (degrees)	-4.6	-2.7(-13.9)	-2.4(-13.4)	-2.3(-9.3)

Table 5.2. Observed and computed thicknesses h and veering angles α from the Level II turbulent closure model (Bird et al., 1982) and the vertically integrated model presented in this thesis when including thermal wind. Observed values and the Level II model results are taken from Table 3b in Bird et al. (1982).

geostrophic velocity of 18.92 cm/s at 62 m above the bottom based on Eq. (5.8). From Eq. (5.7) it can be seen that the values of VS are very small due to the very small Brunt-Vaisala frequency. Therefore $V_g(0, 0)$ is almost the same as 18.92 cm/s. From Eq. (5.5c) the isopycnal slope β_1' is respectively much less than or less than the bottom slope β for the cases $\beta_1 = -0.035$ and $\beta_1 = -0.01$. According to the discussions given in the last section the flow will therefore mainly depend on the bottom slope for these cases. Therefore the thickness should increase with time since the bottom slope is positive (downwelling case).

Note that it was found for these runs that when using Eq. (5.4) to eliminate $\frac{\partial h}{\partial t}$ first in Eqs. (5.1)-(5.3), the singular point of Eqs. (5.1)-(5.4) at $t = 0$ was a serious problem. $B_1^2 - 4A_1C_1$ (Eq. 5.9) became negative. It is believed that this problem was caused by the very small value of $\frac{N_o}{f}$ in this case. In order to overcome this difficulty, Eqs. (5.1)-(5.4) were solved by eliminating $\frac{\partial \epsilon}{\partial t}$ first based on Eq. (5.4). The results obtained from the vertically integrated model are also given in Table 5.2. The ramp period T_f is 24 h, as in Bird et al. (1982). The values from the Level II turbulent closure model listed in Table 5.2 are taken from Table 3b in Bird et al. (1982).

All values listed in Table 5.2 from the vertically integrated model are taken at $t = 24$ h, the end of the ramp period. (Note that Bird et al. (1982) did not specify at what time the values listed in their Table 3b are taken.) When $\beta_1 = 0$

the results are very similar to that for a horizontal flat bottom (see Fig. 5.8) and all variables reach a steady state. But there are some oscillations appearing just after the ramp period because the Brunt-Vaisala frequency is much smaller than in Fig. 5.8. These oscillations diminish after several days. Table 5.2 shows that for $\beta_1 = 0$ and -0.01 the thicknesses are much greater than the values obtained from the Level II model, but the veering angles are much smaller and in better agreement with the observations. For $\beta_1 = -0.035$ both the thickness and the veering angle are less than those computed from the Level II turbulent closure model and are closer to the observed values.

Note that here the value of α' greatly affects the results because the $\frac{N_o}{f}$ is less than one. Therefore the dependence of α' on the bottom slope β and the ratio $\frac{VS}{f}$ may be important but cannot be determined here. This may contribute to the discrepancies between the model results and the observations.

Another factor which may also contribute to the discrepancies is the stringent limit of small bottom slope for the assumption of x-independence in the mixed layer in both the Level II turbulent closure model (Bird et al., 1982) and the vertical integrated model, because the bottom slope here is not small.

CHAPTER 6

SUMMARY AND CONCLUSIONS

A new vertically-integrated model for bottom mixed layer growth has been presented. An important feature of the model is that the vertical variation of mean velocity with height is retained throughout the derivation, finally appearing as a parameter in the vertically-integrated energy equation. This distinguishes it from conventional slab models. A second feature is the separation of mixed layer density into two components: one due to local vertical mixing, and one to advection parallel to the bottom. The effects of both bottom slope and thermal wind in the interior geostrophic flow are included.

For a horizontal flat bottom without thermal wind an analytic solution is obtained which yields a formula for bottom mixed layer thickness containing the velocity profile parameter α'. This formula is consistent with all previous formulae for bottom boundary layer thickness, including that proposed by Weatherly and Martin (1978) on the basis of their numerical results from the Level II turbulent closure scheme. Although α' depends explicitly on the stratification $(\frac{N_o}{f})$, this dependence appears to be rather weak. Two choices for α' are therefore suggested: one ($\alpha' = 0.59$) for thicknesses defined as the height at which the turbulent kinetic energy vanishes; the other ($\alpha' = 6.3$) for thicknesses defined in terms of the mean velocity profile. The latter is consistent with $h = 0.4\frac{u_*}{f}$ in the

neutrally stratified case. The choice of α' is most important for the case $\frac{N_0}{f}$ less than or of order unity. Formulae for the dependence of friction velocity and veering angle on geostrophic velocity and stratification are also obtained for this case.

For a sloping flat bottom at the initial stage of bottom boundary layer growth the vertically integrated model gives results similar to those obtained by Weatherly and Martin (1978) using a Level II turbulent closure model. The main effect of bottom slope is to produce upwelling or downwelling within the bottom mixed layer depending on the sign of the bottom slope. After the initial period of bottom boundary layer development the vertically integrated buoyancy force can grow to reach a balance with the vertically integrated driving pressure gradient so that the flow becomes steady and the Ekman transport is extinguished. The layer is arrested in a vertically integrated sense. The length of the initial period greatly depends on the sign of bottom slope, and in the downwelling case may approach infinity.

The effect of thermal wind in the interior flow on bottom mixed layer growth is shown to be important. For a horizontal flat bottom when the vertical shear in the interior is positive, at the initial stage of bottom boundary layer development the effect of thermal wind is similar to that of positive bottom slope. However after the initial stage the effect of thermal wind is different, and the mixed layer thickness and the speed of mixed layer can increase indefinitely. When the verti-

cal shear is negative the thickness cannot grow if the geostrophic velocity is constant. This is readily understood physically. When the vertical shear is positive the geostrophic velocity at the interface increases as the mixed layer grows, and thus the kinetic energy of water entrained into the mixed layer increases with time, providing a steadily increasing source of energy for mixing. When the vertical shear is negative the geostrophic velocity at the interface decreases as the layer grows, and the kinetic energy supply for mixing decreases. Besides, the transverse flow always drives denser fluid from the positive x-direction towards the negative x-direction along the bottom, and therefore ϵ is always positive and the potential energy term $\frac{\epsilon g h}{\rho_o}$ can increase indefinitely if the thickness doesn't decrease.

For a sloping flat bottom with thermal wind, when the isopycnals are parallel to the bottom, the flow approaches a steady state quickly and the results are very similar to that for a horizontal flat bottom with no thermal wind: that is, the effects of bottom slope and isopycnal slope offset each other. When the bottom slope is much larger than the isopycnal slope, thermal wind is unimportant (and vice-versa).

Solutions are also obtained for the relaxation of motion in the boundary layer after the interior geostrophic velocity is suddenly stopped, and are presented in Appendix 3. It is shown that the frequency of inertial oscillations is increased by bottom slope and Brunt-Vaisala frequency, because the buoyancy

force parallel to the bottom provides an additional restoring force.

The dependence of α' on bottom slope, β, and on the ratio $\frac{VS}{f}$ has not been obtained. When $\frac{N_o}{f} < 1$, or of order 1, the dependence of α' on bottom slope β, and $\frac{VS}{f}$ could be important because the value of α' appears then to have a greater effect on the results. This should probably wait for further experiments and observations to determine.

The discontinuity of density at the interface may be another problem in this model, particularly on a sloping bottom. The improvement of this aspect may be expected through adding a transition layer outside the well mixed layer to incorporate the effects of restratification produced by secondary circulation.

The vertically integrated model could be extended to include variations in the plane parallel to the bottom, which the observations made by Armi and D'Asaro (1980) have shown to be important. Such an extension would permit, for example, investigation of how the bottom mixed layer separates from the sea floor and intrudes into the ocean interior. Finally, the vertically integrated model is readily adapted to the wind-driven surface mixed layer.

APPENDIX 1

Derivation of Energy Equation for Sloping Bottom Case.

Now the energy equation is derived. In the bottom coordinate system the dot product of Eqs. (3.30)-(3.32) with $\vec{U}$ produces

$$\frac{\rho_o}{2}\frac{\partial(u^2)}{\partial t} + \rho_o\frac{\partial \hat{u}}{\partial t}u + \rho_o(u^2 + u\hat{u})\frac{\partial}{\partial x}(u + \hat{u})$$
$$+ \rho_o(uv + uV_g + u\hat{v})\frac{\partial}{\partial y}(u + \hat{u}) + \rho_o(uW + u\hat{w})\frac{\partial}{\partial z}(u + \hat{u})$$
$$+ \frac{\rho_o}{2}\frac{\partial(v + V_g)^2}{\partial t} + \rho_o\frac{\partial \hat{v}}{\partial t}(v + V_g) + \rho_o(v + V_g)(u + \hat{u})\frac{\partial}{\partial x}(v + V_g + \hat{v})$$
$$+ \rho_o(v + V_g)(v + V_g + \hat{v})\frac{\partial}{\partial y}(v + V_g + \hat{v})$$
$$+ \rho_o(W + \hat{w})(v + V_g)\frac{\partial}{\partial z}(v + V_g + \hat{v}) + \frac{\rho_o}{2}\frac{\partial W^2}{\partial t} + \rho_o\frac{\partial \hat{w}}{\partial t}W$$
$$+ \rho_o W(u + \hat{u})\frac{\partial}{\partial x}(W + \hat{w}) + \rho_o W(v + V_g + \hat{v})\frac{\partial}{\partial y}(W + \hat{w})$$
$$+ \rho_o(W^2 + W\hat{w})\frac{\partial}{\partial z}(W + \hat{w}) = -\frac{\partial P'}{\partial x}u - \frac{\partial \hat{p}}{\partial x}u - (\rho' + \hat{\rho})g\beta u$$
$$- \frac{\partial P'}{\partial z}W - \frac{\partial \hat{p}}{\partial z}W - (\rho' + \hat{\rho})gW. - \frac{\partial P'}{\partial y}(v + V_g) - \frac{\partial \hat{p}}{\partial y}(v + V_g)$$
$$+ \mu\left[u\nabla^2(u + \hat{u}) + (v + V_g)\nabla^2(v + V_g + \hat{v}) + W\nabla^2(W + \hat{w})\right] \qquad \text{(A1.1)}$$

Time-averaging Eq. (A1.1) yields

$$\frac{\rho_o}{2}\frac{\partial}{\partial t}[u^2 + (v + V_g)^2] + \frac{\rho_o}{2}(v + V_g)\frac{\partial}{\partial y}[u^2 + (v + V_g)^2]$$
$$+ \frac{\rho_o}{2}u\frac{\partial}{\partial x}[u^2 + (v + V_g)^2] = -uP'_x - \rho' g\beta u - \rho_o u\frac{\partial<\hat{u}^2>}{\partial x} - \rho_o u\frac{\partial<\hat{u}\hat{v}>}{\partial y}$$
$$- \rho_o u\frac{\partial<\hat{u}\hat{w}>}{\partial z} - \rho_o(v + V_g)\frac{\partial<\hat{u}\hat{v}>}{\partial x} - \rho_o(v + V_g)\frac{\partial<\hat{v}^2>}{\partial y}$$
$$- \rho_o(v + V_g)\frac{\partial<\hat{v}\hat{w}>}{\partial z}, \qquad \text{(A1.2)}$$

where $W = 0$ is assumed, the mean quantities are independent of x and y, the viscous terms are ignored because the Reynolds number is large and the incompressibility condition is used. Since the horizontal scales are much larger than the vertical scale $\frac{\partial}{\partial x} \ll \frac{\partial}{\partial z}$ and $\frac{\partial}{\partial y} \ll \frac{\partial}{\partial z}$. Therefore the mean mechanical energy balance equation is, after ignoring the advection terms,

$$\frac{\rho_o}{2}\frac{\partial}{\partial t}(u^2 + (v + V_g)^2) = -uP'_x - \rho' g \beta u - \rho_o u\frac{\partial <\hat{u}\hat{w}>}{\partial z} - \rho_o (v + V_g)\frac{\partial <\hat{v}\hat{w}>}{\partial z}. \tag{A1.3}$$

The dot product of the momentum equations with $\vec{u}'$ yields

$$\begin{aligned}
&\frac{\rho_o}{2}\frac{\partial \hat{u}^2}{\partial t} + \rho_o \frac{\partial u}{\partial t}\hat{u} + \rho_o(u\hat{u} + \hat{u}^2)\frac{\partial}{\partial x}(u + \hat{u}) + \rho_o(v + V_g)\hat{u}\frac{\partial u}{\partial y} \\
&+ \frac{\rho_o}{2}(v + V_g)\frac{\partial \hat{u}^2}{\partial y} + \rho_o \hat{u}\hat{v}\frac{\partial u}{\partial y} + \frac{\rho_o}{2}\hat{v}\frac{\partial \hat{u}^2}{\partial y} + \rho_o \hat{u}(W + \hat{w})\frac{\partial}{\partial z}(u + \hat{u}) \\
&+ \frac{\rho_o}{2}\frac{\partial \hat{v}^2}{\partial t} + \rho_o \hat{v}\frac{\partial}{\partial t}(v + V_g) + \rho_o \hat{v}(\hat{u} + u)\frac{\partial}{\partial x}(v + V_g + \hat{v}) \\
&+ \rho_o(v + V_g)\hat{v}\frac{\partial}{\partial y}(v + V_g) + \rho_o \hat{v}^2\frac{\partial}{\partial y}(v + V_g) + \frac{\rho_o}{2}(v + V_g)\frac{\partial \hat{v}^2}{\partial y} \\
&\frac{\rho_o}{2}\hat{v}\frac{\partial \hat{v}^2}{\partial y} + \rho_o \hat{v}(W + \hat{w})\frac{\partial}{\partial z}(v + V_g + \hat{v}) \\
&+ \frac{\rho_o}{2}\frac{\partial \hat{w}^2}{\partial t} + \rho_o \hat{w}\frac{\partial W}{\partial t} + \rho_o \hat{w}(\hat{u} + u)\frac{\partial}{\partial x}(W + \hat{w}) \\
&+ \rho_o \hat{w}(v + V_g + \hat{v})\frac{\partial}{\partial y}(W + \hat{w}) + \rho_o \hat{w}(W + \hat{w})\frac{\partial}{\partial z}(W + \hat{w}) = -\frac{\partial P'}{\partial x}\hat{u} \\
&- \frac{\partial \hat{p}}{\partial x}\hat{u} - (\rho' + \hat{\rho})g\beta\hat{u} - \hat{w}\frac{\partial P'}{\partial z} - \hat{w}\frac{\partial \hat{p}}{\partial z} - g\hat{w}(\rho' + \hat{\rho}) - \frac{\partial P'}{\partial y}\hat{v} - \hat{v}\frac{\partial \hat{p}}{\partial y} \\
&+ \mu\hat{u}[\nabla^2 u + \nabla^2\hat{u}] + \mu\hat{v}[\nabla^2(v + V_g) + \nabla^2\hat{v}] + \mu\hat{w}[\nabla^2 W + \nabla^2\hat{w}].
\end{aligned} \tag{A1.4}$$

The last terms involving the viscosity can be rewritten using

$$\begin{aligned}
&\hat{u}\nabla^2\hat{u} + \hat{v}\nabla^2\hat{v} + \hat{w}\nabla^2\hat{w} = \hat{u}\nabla^2\hat{u} + \hat{v}\nabla^2\hat{v} + \hat{w}\nabla^2\hat{w} + (\vec{u}\cdot\vec{\nabla})(\vec{\nabla}\cdot\vec{u}) \\
&= \frac{\partial}{\partial x_j}[\hat{u}_i(\frac{\partial \hat{u}_i}{\partial x_j} + \frac{\partial \hat{u}_j}{\partial x_i})] - 2\hat{s}_{ij}\frac{\partial \hat{u}_j}{\partial x_i}
\end{aligned}$$

where

$$\hat{s}_{ij} = \frac{1}{2}\left(\frac{\partial \hat{u}_i}{\partial x_j} + \frac{\partial \hat{u}_j}{\partial x_i}\right).$$

We also have

$$2\hat{s}_{ij}\frac{\partial \hat{u}_j}{\partial x_i} = 2\hat{s}_{ij}\,\hat{s}_{ij}$$

(Monin and Yaglom, 1979, p. 375). Substituting the above result in Eq. (A1.4), time-averaging and making use of the condition $W = 0$ result in

$$\begin{aligned}
&\frac{\rho_o}{2}\frac{\partial <q^2>}{\partial t} + \frac{\rho_o}{2}u\frac{\partial <q^2>}{\partial x} + \frac{\rho_o}{2}(v + V_g)\frac{\partial <q^2>}{\partial y} + \rho_o <\hat{u}^2>\frac{\partial u}{\partial x} \\
&+ \rho_o <\hat{u}\hat{v}>\frac{\partial u}{\partial y} + \rho_o <\hat{u}\hat{w}>\frac{\partial u}{\partial z} + \rho_o <\hat{u}\hat{v}>\frac{\partial}{\partial x}(v + V_g) \\
&+ \rho_o <\hat{v}^2>\frac{\partial}{\partial y}(v + V_g) + \rho_o <\hat{w}\hat{v}>\frac{\partial}{\partial z}(v + V_g) \\
&+ \frac{\rho_o}{2}\frac{\partial}{\partial x}<\hat{u}q^2> + \frac{\rho_o}{2}\frac{\partial}{\partial y}<\hat{v}q^2> + \frac{\rho_o}{2}\frac{\partial}{\partial z}<\hat{w}q^2> \\
&= -\frac{\partial <\hat{p}\hat{u}>}{\partial x} - \frac{\partial <\hat{p}\hat{v}>}{\partial y} - \frac{\partial <\hat{p}\hat{w}>}{\partial z} - <\hat{\rho}\hat{u}>g\beta - g<\hat{\rho}\hat{w}> \\
&+ \mu\frac{\partial}{\partial x_j}<\hat{u}_i\left(\frac{\partial \hat{u}_i}{\partial x_j} + \frac{\partial \hat{u}_j}{\partial x_i}\right)> - 2\mu<\hat{s}_{ij}\,\hat{s}_{ij}>. \qquad \text{(A1.5)}
\end{aligned}$$

By ignoring advective terms, taking $\frac{\partial}{\partial x} \ll \frac{\partial}{\partial z}$, $\frac{\partial}{\partial y} \ll \frac{\partial}{\partial z}$ and assuming $<\hat{\rho}\hat{u}>\beta \ll <\hat{\rho}\hat{w}>$, Eq. (A1.5) reduces to

$$\begin{aligned}
&\rho_o\frac{\partial <q^2>}{\partial t} + \frac{\rho_o}{2}\frac{\partial}{\partial z}<\hat{w}q^2> = -\frac{\partial}{\partial z}<\hat{w}\hat{p}> - \rho_o <\hat{u}\hat{w}>\frac{\partial u}{\partial z} \\
&- \rho_o <\hat{v}\hat{w}>\frac{\partial (v + V_g)}{\partial z} - <\hat{w}\hat{\rho}>g \\
&+ 2\mu\frac{\partial}{\partial z}<\hat{u}\hat{s}_{xz} + \hat{v}\hat{s}_{yz} + \hat{w}\hat{s}_{zz}> - \varsigma \qquad \text{(A1.6)}
\end{aligned}$$

in which $\varsigma = 2\mu<\hat{s}_{ij}\,\hat{s}_{ij}>$ is the average mechanical dissipation rate. Adding Eq.

(A1.6) to Eq. (A1.3) yields

$$\frac{\rho_o}{2}\frac{\partial}{\partial t}(u^2 + (v + V_g)^2 + \langle q^2\rangle) + \frac{\rho_o}{2}\frac{\partial}{\partial z}\langle \hat{w}q^2\rangle + \frac{\partial}{\partial z}\langle \hat{w}\hat{p}\rangle$$
$$= -uP'_x - \rho' g\,\beta u - \rho_o \frac{\partial}{\partial z}[u\langle \hat{u}\hat{w}\rangle + (v + V_g)\langle \hat{v}\hat{w}\rangle]$$
$$+ 2\mu\frac{\partial}{\partial z}\langle \hat{u}\hat{s}_{xz} + \hat{v}\hat{s}_{yz} + \hat{w}\hat{s}_{zz}\rangle - \varsigma - \langle \hat{w}\hat{\rho}\rangle g \qquad \text{(A1.7)}$$

which is Eq. (3.35).

APPENDIX 2

Derivation of Governing Equations Including Thermal Wind

A.2.1. Horizontal Flat Bottom Case.

A.2.1.1. Interior Flow.

As in Chapter 2 the flow in the interior is assumed to be geostrophic:

$$\rho_o \vec{\Omega} \times \vec{V}_g = -\vec{\nabla} P_o + \rho_o \vec{g} \tag{A2.1.1}$$

Note that now V_g depends on the vertical coordinate z', whereas before it was independent of depth. The component equations of Eq. (A2.1.1) become

$$-\rho_o f V_g(z) = -\frac{\partial P_o}{\partial x} \tag{A2.1.2}$$

$$0 = \frac{\partial P_o}{\partial y} \tag{A2.1.3}$$

$$0 = \frac{\partial P_o}{\partial z} + \rho_o(z, z) g \tag{A2.1.4}$$

Assuming the isopycnals in the interior are inclined at an angle β_1' (see Fig. A2.1) to the horizontal, then

$$\tan\beta_1' = -\frac{\dfrac{\partial \rho_o}{\partial x}}{\dfrac{\partial \rho_o}{\partial z}} \tag{A2.1.5}$$

From Eqs. (A2.1.2), (A2.1.4) and (A2.1.5) it can be deduced that

$$\frac{\partial V_g}{\partial z} = -\tan\beta_1' \frac{N_o^2}{f} \equiv VS \tag{A2.1.6}$$

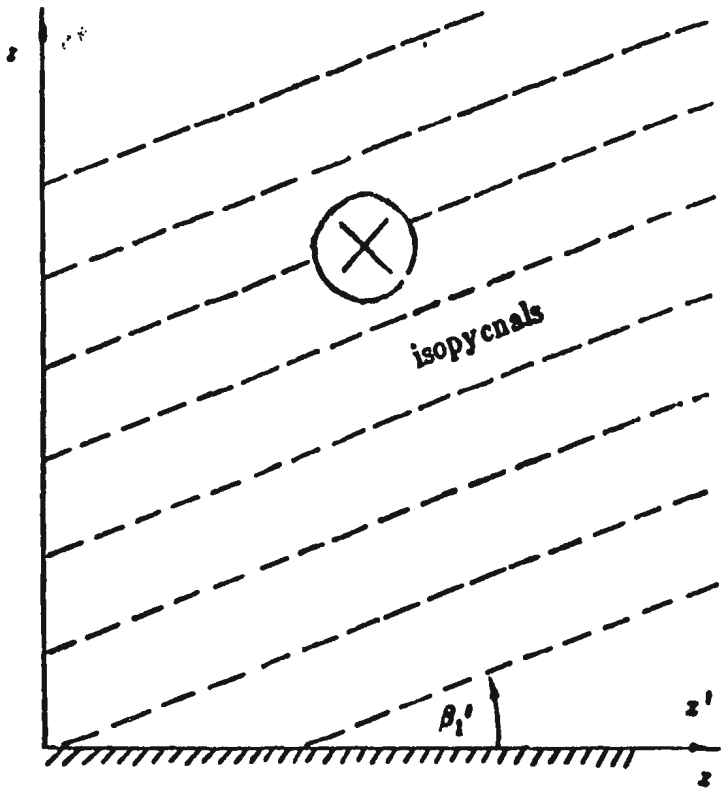

Figure A2.1. A sketch of a horizontal flat bottom with horizontal density gradient.

which is the usual thermal relation (Pond and Pickard, 1981), and where VS stands for the vertical shear. When β_1' is small this becomes

$$\frac{\partial V_g}{\partial z} = -\beta_1' \frac{N_o^2}{f}. \tag{A2.1.7}$$

It is important to note that N_o^2 and therefore VS are independent of both x and z. Integrating Eq. (A2.1.7) with respect to z yields

$$V_g(z) = V_g(0) + zVS \tag{A2.1.8}$$

and the geostrophic velocity averaged over the bottom mixed layer height h is

$$\bar{V}_g = \frac{1}{h}\int_0^h V_g(z)dz = V_g(0) + \frac{1}{2}hVS \tag{A2.1.9}$$

A.2.1.2. Density in the Mixed Layer.

When thermal wind is included the density ρ' in the mixed layer is still assumed to be uniform in the z-direction and can be separated into two parts:

$$\rho' = [\rho_o(x, z) + \rho''(z, t)] + \epsilon(t) \tag{A2.1.10a}$$

where as before the first part caused by local mixing is always equal to the average of the density profile prior to mixing and is given by Eq. (3.9) which is rewritten here for convenience

$$\rho_o(x, z) + \rho''(z, t) = \rho_o(x, 0) + \rho_{oz}\frac{h}{2}. \tag{A2.1.10b}$$

The second part ϵ is the advective contribution caused by Ekman transport, present now in the horizontal bottom case because of the thermal wind. Note that it is again assumed that ϵ and h are independent of x since the geostrophic velocity, N_o and $\frac{\partial V_g}{\partial z}$ are independent of x. Therefore Eqs. (3.9)-(3.13) and

(3.26)-(3.27) are still valid here.

A.2.1.3. Momentum Equations

The assumption made is that in the mixed layer the flow is still hydrostatic. Therefore

$$\frac{\partial P'}{\partial z} = -\rho' g. \tag{A2.1.11a}$$

By substituting Eq. (A2.1.10a) into Eq. (A2.1.11a) and using Eq. (A2.1.4), Eqs. (3.14) and (3.17) can be deduced. Therefore

$$P'_z = P_{oz}. \tag{A2.1.11}$$

The momentum equation in the bottom mixed layer is

$$\rho' \frac{\partial \vec{U}}{\partial t} + \rho' \vec{\Omega} \times \vec{U} = -\nabla P' + \rho' \vec{g} + \frac{\partial \vec{\tau}}{\partial z}, \tag{A2.1.12}$$

where all the assumptions made in Chapter 2 for linearizing the momentum equation have been used. By using the Boussinesq approximation and Eq. (A2.1.11) the x and y components become

$$\rho_o \frac{\partial u}{\partial t} - \rho_o f (v + V_g) = -\frac{\partial P_o}{\partial x} + \frac{\partial \tau^x}{\partial z} \tag{A2.1.13a}$$

$$\rho_o \frac{\partial (v + V_g)}{\partial t} + \rho_o f u = -\frac{\partial P_o}{\partial y} + \frac{\partial \tau^y}{\partial z}. \tag{A2.1.13b}$$

After substituting Eqs. (A2.1.2) and (A2.1.3) and because $\frac{\partial V_g}{\partial t} = 0$ the momentum equations become:

$$\rho_o \frac{\partial u}{\partial t} - \rho_o f v = \frac{\partial \tau^x}{\partial z} \tag{A2.1.14a}$$

$$\rho_o \frac{\partial v}{\partial t} + \rho_o f u = \frac{\partial \tau^y}{\partial z}, \tag{A2.1.14b}$$

which, after vertical integration and making use of Eq. (2.6) and the assumption (2.9), identically become Eqs (2.7) and (2.8), the momentum equations in the mixed layer in the absence of thermal wind.

A.2.1.4. Mass Conservation.

The continuity equation is the same as Eq. (2.3) and Eq. (2.4) can be applied here. It is also assumed that Eq. (2.5) and therefore (2.6) are valid, again since V_g and N_o are independent of z.

Because when including the thermal wind the density is no longer independent of z, deriving an equation for mass conservation must begin with Eq. (3.19). The vertically integrated form (3.24) also holds, as does the expression (3.25) for the turbulent mass flux at the interface in terms of entrainment, since it includes the dependence of the density of the entrained fluid on z and h. The density in the mixed layer may still be written in the form Eq. (3.26), but now

$$\frac{\partial \rho'}{\partial z} = \frac{\partial \rho_o}{\partial z} = -\tan\beta_1' \frac{\partial \rho_o}{\partial z} \qquad \text{(A2.1.15a)}$$

where use has been made of (A2.1.5). Otherwise the derivation which led to Eq. (3.29) is unchanged, and its equivalent for the present case is therefore

$$\frac{g}{\rho_o}(h\epsilon)_t = -\tan\beta_1' \, h\bar{u}N_o^2 \qquad \text{(A2.1.15)}$$

which is to be compared with Eq. (3.29). It is seen that for β_1' small the two equations have the same form, with the negative isopycnal slope now taking the place of the bottom slope.

A.2.1.5. Energy Equation

For the horizontal flat bottom case including thermal wind Eq. (2.15) is still valid. For convenience it is rewritten here:

$$\frac{\rho_o}{2}\int_0^h\left[\frac{\partial}{\partial t}(u^2+(v+V_g)^2+<q^2>)\right]dz = -\int_0^h uP'_x\,dz$$
$$-\int_0^h <\hat{w}\,\hat{\rho}>g\,dz - \int_0^h \varsigma\,dz. \qquad \text{(A2.1.16)}$$

Note that Eq. (2.16a) is not applicable because the density varies in the horizontal plane. Instead the mass conservation Eq. (3.19) can be applied for calculating the buoyant production term $\int_0^h <\hat{w}\,\hat{\rho}>g\,dz$ on the right-hand side of the equation above. Substituting Eqs. (3.27), (A2.1.15a) and (2.20a) into Eq. (3.19) and then integrating the resulting equation from 0 to z yields

$$-<\hat{\rho}\hat{w}>|_z = \frac{\rho_{oz}}{2}\frac{\partial h}{\partial t}z + \epsilon_t z - \bar{u}\tan\beta_1'\rho_{oz}z - [\int_0^z \Delta u\,dz\,']\tan\beta_1'\rho_{oz}. \qquad \text{(A2.1.17)}$$

After integrating from 0 to h and by making use of Eq. (A2.1.15), Eq. (A2.1.17) becomes

$$-\int_0^h g<\hat{\rho}\hat{w}>dz = \frac{1}{4}\rho_{oz}gh^2h_t - \frac{g\epsilon h}{2}h_t - \tan\beta_1'\rho_{oz}g\int_0^h[\int_0^z \Delta u\,dz\,']dz. \qquad \text{(A2.1.18)}$$

Substituting Eqs. (A2.1.11) and (A2.1.18) into Eq. (A2.1.16) yields

$$\frac{\rho_o}{2}\int_0^h\left[\frac{\partial}{\partial t}(u^2+(v+V_g)^2+<q^2>)\right]dz = -\int_0^h uP_{ox}\,dz$$
$$\frac{1}{4}\rho_{oz}gh^2h_t - \frac{g\epsilon h}{2}h_t - \tan\beta_1'\rho_{oz}g\int_0^h[\int_0^z \Delta u\,dz\,']dz - \int_0^h \varsigma\,dz, \qquad \text{(A2.1.19)}$$

which corresponds to Eq. (2.17) but is different because the buoyant production

term is now not only caused by local mixing, but also by the advective contribution ϵ and the vertical variation of u, and because the pressure gradient in the interior varies in the z-direction (see Eq. A2.1.2).

Again the assumption Eq. (2.18) is made which is rewritten here

$$\frac{\rho_o}{2}\int_0^h \frac{\partial \langle q^2 \rangle}{\partial t} dz + \int_0^h \varsigma dz = \vec{\tau}_b \cdot \vec{U}. \tag{A2.1.20}$$

Substituting Eq. (A2.1.20) into Eq. (A2.1.19) yields

$$\frac{\rho_o}{2}\int_0^h \frac{\partial}{\partial t}[u^2 + (v + V_g)^2]dz - \frac{1}{4}\rho_{oz} g h^2 h_t + \frac{g\epsilon h}{2} h_t + \tan\beta_1' \rho_{oz} g \int_0^h [\int_0^z \Delta u dz']dz$$
$$= -\int_0^h u P_{ox}\, dz - \bar{u}\tau_b{}^x - (\bar{v} + \bar{V}_g)\tau_b{}^y. \tag{A2.1.21}$$

The first term on the right-hand side of the equation above is the rate of work done by the geostrophic pressure gradient. Letting

$$u = \bar{u} + \Delta u \tag{A2.1.22a}$$
$$v + V_g = \bar{V} + \Delta v = \bar{V}_g + \bar{v} + \Delta v. \tag{A2.1.22b}$$

and using Eqs. (A2.1.2), (A2.1.6), (A2.1.8) and (A2.1.9) this term becomes:

$$-\int_0^h u P_{ox}\, dz = -\int_0^h (\bar{u} + \Delta u)\rho_o f V_g\, dz$$
$$= -\rho_o f \bar{u}\bar{V}_g h - \rho_o f VS \int_0^h z\, \Delta u dz$$
$$= -\rho_o f \bar{u}\bar{V}_g h - \rho_{oz} g \tan\beta_1' \int_0^h z\, \Delta u dz \tag{A2.1.23}$$

As in Chapter 3 it can be shown using integration by parts that the sum of $\int_0^h \Delta u z dz$ in Eq. (A2.1.23) and $\int_0^h [\int_0^z \Delta u dz']dz$ in Eq. (A2.1.21) vanishes. Therefore

substituting Eq. (A2.1.23) into Eq. (A2.1.21) yields

$$\frac{\rho_o}{2}\int_0^h \frac{\partial}{\partial t}[u^2 + (v + V_g)^2]dz - \frac{1}{4}\rho_{oz} g h^2 h_t + \frac{g\epsilon h}{2} h_t$$
$$= -\rho_o f \bar{u}\bar{V}_g h - \bar{u}\tau_b^x - (\bar{v} + \bar{V}_g)\tau_b^y, \qquad \text{(A2.1.24)}$$

which corresponds to Eq. (2.19). Note that now $\bar{V}_g$ is the vertical average of V_g over the boundary layer thickness.

The first term of Eq. (A2.1.24) becomes, after using Eqs. (A2.1.22a) and (A2.1.22b)

$$\frac{\rho_o}{2}\int_0^h \frac{\partial}{\partial t}[u^2 + (v + V_g)^2]dz = \frac{\rho_o}{2}\frac{\partial}{\partial t}\int_0^h [u^2 + (v + V_g)^2]dz - \frac{\rho_o}{2}U^2|_{z=h}\frac{\partial h}{\partial t}$$
$$= \frac{\rho_o}{2}\frac{\partial}{\partial t}\left[h(\bar{u}^2 + \bar{v}^2 + 2\bar{v}\bar{V}_g)\right] + \frac{\rho_o}{2}\frac{\partial}{\partial t}\int_0^h [(\Delta u)^2 + (\Delta v)^2]dz$$
$$+ \frac{\rho_o}{2}\left[\frac{\partial}{\partial t}(\bar{V}_g{}^2 h) - V_g{}^2|_{z=h}\frac{\partial h}{\partial t}\right] \qquad \text{(A2.1.25)}$$

where $U^2 = V_g{}^2$ at $z = h$ has been used. From Eqs. (A2.1.8) and (A2.1.9) it can be shown that

$$\frac{\partial}{\partial t}(\bar{V}_g{}^2 h) - V_g{}^2|_{z=h}\frac{\partial h}{\partial t} = -\frac{1}{4}(VS)^2 h^2 \frac{\partial h}{\partial t} \qquad \text{(A2.1.26)}$$

and

$$\frac{\partial \bar{V}_g}{\partial t} = \frac{1}{2} VS \frac{\partial h}{\partial t} \qquad \text{(A2.1.27)}$$

Substituting Eqs. (A2.1.26) and (A2.1.27) into Eq. (A2.1.25) yields

$$\frac{\rho_o}{2}\int_0^h \frac{\partial}{\partial t}[u^2 + (v + V_g)^2]dz = \frac{\rho_o}{2}(\bar{u}^2 + \bar{v}^2 + 2\bar{v}\bar{V}_g)\frac{\partial h}{\partial t}$$
$$+ \frac{\rho_o}{2} h \frac{\partial}{\partial t}(\bar{u}^2 + \bar{v}^2) + \rho_o h \bar{V}_g \frac{\partial \bar{v}}{\partial t} + \frac{\rho_o}{2}\frac{\partial}{\partial t}\int_0^h [(\Delta u)^2 + (\Delta v)^2]dz$$

$$-\frac{\rho_o}{8} VS^2h^2\frac{\partial h}{\partial t} + \frac{\rho_o}{2} VSh\bar{v}\frac{\partial h}{\partial t}. \qquad \text{(A2.1.28)}$$

By using Eqs. (A2.1.28) and (2.7) and (2.8), Eq. (A2.1.24) reduces to

$$\frac{\rho_o}{2}\left[\frac{N_o^2h^2}{2} + \frac{g\epsilon h}{\rho_o}(\bar{u}^2+\bar{v}^2) - \frac{1}{4} VS^2h^2 + VSh\bar{v}\right]\frac{\partial h}{\partial t}$$

$$+ \frac{\rho_o}{2}\frac{\partial}{\partial t}\int_0^h[(\Delta u)^2 + (\Delta v)^2]dz = 0 \qquad \text{(A2.1.29)}$$

which reduces to Eq. (2.21) in the absence of thermal wind.

A.2.1.6. The Velocity Profile Parameter

As discussed in Chapter 2 the integral $\int_0^h[(\Delta u)^2 + (\Delta v)^2]dz$ is approximately proportional to $V_g^2|_{z=h}h$, because it is assumed that the velocity profiles remain self-similar during growth:

$$\Delta u = -V_g|_{z=h} G'(\zeta_1)$$
$$\Delta v = V_g|_{z=h} F'(\zeta_1).$$

Therefore

$$\int_0^h[(\Delta u)^2 + (\Delta v)^2]dz$$

$$= (V_g|_{z=h})^2 h\int_0^1 (G'^2 + F'^2)d\zeta_1 = E'hV_g^2|_{z=h} \qquad \text{(A2.1.30)}$$

where E' is a proportionality coefficient, and then

$$\frac{\partial}{\partial t}\int_0^h[(\Delta u)^2 + (\Delta v)^2]dz = 2E'V_g|_{z=h}\frac{\partial(V_g|_{z=h})}{\partial t}h$$

$$+ E'V_g^2|_{z=h}\frac{\partial h}{\partial t} = \left[E'V_g^2|_{z=h} + 2E'V_g|_{z=h} VS\ h\right]\frac{\partial h}{\partial t} \qquad \text{(A2.1.31)}$$

where Eq. (A2.1.8) has been used. Note that from the dimensional analysis here

α' should depend on $\frac{VS}{f}$ and $\frac{N_o}{f}$. Substituting Eq. (A2.1.31) into Eq. (A2.1.29) yields

$$\frac{\rho_o}{2}\left[\frac{N_o{}^2h^2}{2}+\frac{g\epsilon h}{\rho_o}(\bar{u}^2+\bar{v}^2)-\frac{1}{4}VS^2h^2+VSh\bar{v}\right.$$
$$\left.+E'V_g{}^2|_{z=h}+2E'V_g|_{z=h}VS\ h\right]\frac{\partial h}{\partial t}=0. \qquad \text{(A2.1.32)}$$

During mixed layer growth $\frac{\partial h}{\partial t}\neq 0$ it is deduced that

$$\frac{N_o{}^2h^2}{2}+\frac{g\epsilon h}{\rho_o}(\bar{u}^2+\bar{v}^2)-\frac{1}{4}VS^2h^2+VSh\bar{v}$$
$$+E'V_g{}^2|_{z=h}+2E'V_g|_{z=h}VSh=0. \qquad \text{(A2.1.33)}$$

The only problem left in Eq. (A2.1.33) is how to deal with E'. Again the velocity profile parameter is introduced using Eq. (2.22a). Substituting Eq. (2.22a) into Eq. (A2.1.30) yields

$$E'V_g{}^2|_{z=h}=\alpha' u_*{}^2. \qquad \text{(A2.1.34)}$$

Using Eq. (2.35) it may be written

$$E'V_g|_{z=h}=\alpha' C_d\bar{U}\frac{\bar{U}}{V_g|_{z=h}}. \qquad \text{(A2.1.35)}$$

When the approximation:

$$\frac{\bar{U}}{V_g|_{z=h}}\approx 1 \qquad \text{(A2.1.36)}$$

is made,

$$E'V_g|_{z=h}=\alpha' C_d\bar{U} \qquad \text{(A2.1.37)}$$

can be obtained. Equation (A2.1.34) is used to replace the first E' term in (A2.1.33). The second is replaced using (A2.1.36) and (A2.1.37), yielding

$$\alpha' u_*^2 - (\bar{u}^2 + \bar{v}^2) + 2h\,\alpha' C_d \bar{U} VS + \frac{N_*^2 h^2}{2}$$

$$+ \frac{\epsilon g h}{\rho_*} + h\ VS\left[\bar{v} - \frac{1}{4} hVS\right] = 0 \qquad \text{(A2.1.38)}$$

Note that the approximation (A2.1.36) is not necessary but makes the problem easier to solve because Eq. (A2.1.38), which is quadratic in h, would otherwise be cubic. Numerical tests showed that (A2.1.37) has little effect on the results. This is readily understood. Comparing the two terms which are first order in VS in (A2.1.38), it is seen that since $\alpha' \sim O(1)$, $|\bar{U}| \sim |\bar{v}|$ and $C_d \ll 1$, that the contribution from the term involving C_d (which was obtained using the approximation A2.1.36) is small.

A.2.1.7. Summary of Governing Equations

The governing equations including thermal wind for a horizontal flat bottom are: the momentum equations are the same as Eqs. (2.7) and (2.8), the mass conservation equation (A2.1.15) and the energy equation (A2.1.38). For convenience they are written out together as follows, for $|\beta_1'| \ll 1$:

$$\frac{\partial(\bar{u}h)}{\partial t} - f\bar{v}h = -\frac{1}{\rho_*}\tau_b^{\,x} \qquad \text{(A2.1.39)}$$

$$\frac{\partial(\bar{v}h)}{\partial t} + f\bar{u}h = -\frac{1}{\rho_*}\tau_b^{\,y} \qquad \text{(A2.1.40)}$$

$$\frac{\partial(h\epsilon)}{\partial t} = -\frac{\beta_1'}{g}\rho_* N_*^2 \bar{u}h \qquad \text{(A2.1.41)}$$

$$\alpha' u_*^2 - (\bar{u}^2 + \bar{v}^2) + \frac{N_*^2 h^2}{2} + \frac{\epsilon g h}{\rho_*} - \frac{2h\,\alpha' C_d \bar{U} \beta_1' N_*^2}{f}$$

$$- \beta_1'\left[\frac{N_*^2 \bar{v}h}{f} + \frac{\beta_1' N_*^4 h^2}{4f^2}\right] = 0, \qquad \text{(A2.1.42)}$$

A.2.2. Sloping Flat Bottom Case.

A.2.2.1. Momentum Equations.

In the interior the geostrophic balance is

$$\rho_o \vec{\Omega} \times \vec{V}_g = -\vec{\nabla} P_o + \rho_o \vec{g} \tag{A2.2.1}$$

which is the same as Eq. (A2.1.1). In the unrotated (x', y', z') coordinate system (Fig. 6.1) $\vec{\Omega} = (\Omega_{z'}, \Omega_{y'}, f)$, $\vec{V}_g = (0, V_g(z'), 0)$ and $\vec{g} = (0, 0, -g)$. If ϕ is the latitude and θ is the angle between the x'-direction and due east, then $\Omega_{z'} = 2\Omega\cos\phi\cos\theta$, $\Omega_{y'} = 2\Omega\cos\phi\sin\theta$.

From Eqs. (3.1)-(3.3) the bottom coordinates (x, y, z) are:

$$x = x'\cos\beta + z'\sin\beta \approx x' + z'\beta \tag{A2.2.2}$$

$$y = y' \tag{A2.2.3}$$

$$z = -x'\sin\beta + z'\cos\beta \approx -x'\beta + z'. \tag{A2.2.4}$$

So that in the bottom coordinate system,

$$\vec{\Omega} = (\Omega_{z'} + f\beta, \Omega_{y'}, -\Omega_{z'}\beta + f)$$

$$\vec{V}_g = (0, V_g(z'), 0)$$

The component equations of Eq. (A2.2.1) become

$$-\rho_o f V_g(x, z) = -\frac{\partial P_o}{\partial x} - g\beta\rho_o(x, z) \tag{A2.2.5}$$

$$0 = \frac{\partial P_o}{\partial y} \tag{A2.2.6}$$

$$0 = \frac{\partial P_o}{\partial z} + \rho_o(x, z)g \tag{A2.2.7}$$

because $\Omega_{z'}\beta \ll f$ when $\beta \ll 1$ and ϕ is not too small, and $(\Omega_{z'} + f\beta)V_g \ll g$. Note that in the bottom coordinate system, V_g is in general

a function of both x and z.

Again it is assumed that the isopycnals are inclined at a constant angle β_1' to the horizontal. Then from Fig. (5.1)

$$\beta_1 = \beta_1' - \beta \tag{A2.2.8a}$$

where β_1 is the isopycnal slope relative to the bottom. As shown in Eq. (A2.1.5) it is known that

$$\frac{\partial \rho_o}{\partial x'} = -\tan\beta_1' \frac{\partial \rho_o}{\partial z'} \tag{A2.2.8b}$$

and

$$\frac{\partial \rho_o}{\partial x} = -\tan\beta_1 \frac{\partial \rho_o}{\partial z} \tag{A2.2.8c}$$

Note that from the coordinate transformations Eqs (3.1)-(3.3) and (A2.2.2)-(A2.2.4)

$$\rho_{0x} = \rho_{ox'}\cos\beta + \rho_{oz'}\sin\beta$$
$$\rho_{0z} = -\rho_{ox'}\sin\beta + \rho_{oz'}\cos\beta.$$

Therefore

$$\tan\beta_1 = -\frac{\frac{\partial \rho_o}{\partial x}}{\frac{\partial \rho_o}{\partial z}} = \frac{\frac{\partial \rho_o}{\partial x'}\cos\beta + \frac{\partial \rho_o}{\partial z'}\sin\beta}{\frac{\partial \rho_o}{\partial x'}\sin\beta - \frac{\partial \rho_o}{\partial z'}\cos\beta} = \tan(\beta_1' - \beta)$$

which also leads to $\beta_1 = \beta_1' - \beta$, the same as Eq. (A2.2.8a). By using the Boussinesq approximation from Eqs. (A2.2.5), (A2.2.7) and (A2.2.8c) the thermal wind relation in the bottom coordinate system is:

$$\frac{\partial V_g}{\partial z} = -\frac{N_o^2}{f}(\tan\beta_1 + \beta) \approx -\frac{N_o^2}{f}\tan\beta_1' \equiv VS \tag{A2.2.9}$$

because β is small. When β_1' is also small

$$VS = -\frac{\beta_1' N_0^2}{f} \tag{A2.2.10}$$

From Eq. (A2.2.9) and the fact that V_g depends only on the vertical coordinate z', the geostrophic velocity can be written as

$$V_g(z, z) = V_g(z, 0) + z \ VS. \tag{A2.2.11}$$

where

$$V_g(z, 0) = V_g(0, 0) + \beta z \ VS \tag{A2.2.12}$$

For a sloping bottom it is still assumed that the second part ϵ in Eq. (A2.1.10a) is independent of z. Note that this is approximately true only when the bottom slope is small since for a sloping bottom the geostrophic velocity varies with z. (Note also, however, that Bird et al. (1982) also assumed that all deviations in the bottom boundary layer from the interior quantities only vary with the distance away from the bottom and time, even in the presence of thermal wind.) This assumption allows us to employ Eqs. (A2.1.10a), (A2.1.10b), (3.26) and (3.27) for the sloping bottom case.

The momentum equation in the bottom mixed layer is

$$\rho' \frac{\partial \vec{U}}{\partial t} + \rho' \vec{\Omega} \times \vec{U} = -\nabla P' + \rho' \vec{g} + \frac{\partial \vec{\tau}}{\partial z}. \tag{A2.2.13}$$

The hydrostatic assumption is still used so that Eq. (3.17) is valid here. Therefore

$$P'_z = P_{oz}. \tag{A2.2.14}$$

By using the Boussinesq approximation and Eqs. (3.8) and (A2.2.14), the x and y

component equations of momentum equation (A2.2.13) in the bottom coordinate system are

$$\rho_o \frac{\partial u}{\partial t} - \rho_o f (v + V_g) = -\frac{\partial P_o}{\partial x} - \rho' g \beta + \frac{\partial \tau^x}{\partial z} \qquad \text{(A2.2.15a)}$$

$$\rho_o \frac{\partial (v + V_g)}{\partial t} + \rho_o f u = -\frac{\partial P_o}{\partial y} + \frac{\partial \tau^y}{\partial z}. \qquad \text{(A2.2.16a)}$$

After substituting Eqs. (A2.2.5) and (A2.2.6) and because $\frac{\partial V_g}{\partial t} = 0$, Eqs. (A2.2.15a) and (A2.2.16a) become

$$\frac{\partial u}{\partial t} - f v = -\frac{\rho''}{\rho_o} g \beta - \frac{\epsilon g \beta}{\rho_o} + \frac{1}{\rho_o} \frac{\partial \tau^x}{\partial z} \qquad \text{(A2.2.15)}$$

$$\frac{\partial v}{\partial t} + f u = \frac{1}{\rho_o} \frac{\partial \tau^y}{\partial z} \qquad \text{(A2.2.16)}$$

which are the same as Eqs. (3.15) and (3.16). Integrating Eqs. (A2.2.15) and (A2.2.16) in the z-direction from 0 to h, and making use of Eq. (2.6) and the assumption (2.9), yields Eqs. (3.22) and (3.23).

A.2.2.2. Mass Conservation.

As before it is assumed that $\bar{u}$, $\bar{v}$, ϵ and h are independent of z. Therefore Eqs. (2.5) and (2.6) still bold.

The derivation of the mass conservation equation can start from Eq. (3.19) which is valid here. Integrating Eq. (3.19) from $z = 0$ to h yields Eq. (3.24). Making use of Eqs. (2.5), (3.25), (3.27), and the fact that $\frac{\partial \rho'}{\partial x} = \frac{\partial \rho_o}{\partial x}$, then using (A2.2.8c) it can be shown that Eq. (3.24) becomes

$$\frac{g}{\rho_o}(h \epsilon)_t = -\tan\beta_1 h \bar{u} N_o^2. \qquad \text{(A2.2.17)}$$

Note that β in Eq. (3.29) is replaced by $-\tan\beta_1$ in Eq. (A2.2.17).

A.2.2.3. Energy Equation

Deriving the energy equation begins with Eq. (3.36):

$$\frac{\rho_o}{2}\int_0^h \frac{\partial}{\partial t}[u^2+(v+V_g)^2]dz = -\int_0^h u\frac{\partial P'}{\partial x}dz - \bar{u}\tau_b{}^x - (\bar{v}+V_g)\tau_b{}^y$$

$$-\rho' g\beta\bar{u}h - \int_0^h <\hat{\rho}\hat{w}>gdz, \qquad (3.36)$$

because it remains valid for the case including thermal wind.

In order to calculate the first term on the right-hand side of the equation above, using Eq. (A2.2.14) and then Eqs. (A2.1.22a), (A2.2.5) (A2.2.9), and (A2.2.11) yields

$$-\int_0^h uP'_x\,dz = -\int_0^h uP_{ox}\,dz$$

$$= -\int_0^h(\bar{u}+\Delta u)\left[\rho_o f\,[V_g(z,0)+VS\ z]-(\rho_o(z,0)+\rho_{oz}z)g\beta\right]dz$$

$$= -\rho_o f\bar{u}V_g(z)h + \rho_o(z,0)g\beta\bar{u}h + \frac{\bar{u}}{2}\rho_{oz}g\beta h^2 - (\tan\beta_1'-\beta)\rho_{oz}g\int_0^h \Delta u z dz.$$

$$= -\rho_o f\bar{u}V_g(z)h + \rho_o(z,0)g\beta\bar{u}h + \frac{\bar{u}}{2}\rho_{oz}g\beta h^2$$

$$-\tan\beta_1\,\rho_{oz}g\int_0^h \Delta u z dz. \qquad (A2.2.18)$$

From the mass conservation equation (3.19) it can be shown, as in deriving Eq. (A2.1.18), that:

$$-\int_0^h g\,\overline{\rho}\overline{w}dz = \frac{1}{4}\rho_{oz}gh^2h_t - \frac{g\rho_{oz}\tan\beta_1}{2}\bar{u}h^2 + \frac{gh^2\epsilon_t}{2}$$

$$- \tan\beta_1 \rho_{oz} g \int_0^h [\int_0^z \Delta u dz'] dz. \qquad \text{(A2.2.19)}$$

From Eq. (A2.2.17)

$$\frac{1}{2} g \epsilon_t h^2 = - \frac{\rho_o}{2} \tan\beta_1 h^2 \overline{u} N_o^2 - \frac{g \epsilon h}{2} h_t \qquad \text{(A2.2.20)}$$

is obtained. Substituting Eq. (A2.2.20) in Eq. (A2.2.19) yields

$$- \int_0^h g \overline{\rho w} dz = \frac{1}{4} \rho_{oz} g h^2 h_t - \frac{g \epsilon h}{2} h_t - \tan\beta_1 \rho_{oz} g \int_0^h [\int_0^z \Delta u dz'] dz. \qquad \text{(A2.2.21)}$$

The expression for the time rate of change of local mean kinetic energy per unit area, Eq. (A2.1.28), is still valid for the sloping bottom case. Substituting Eqs (A2.1.28), (3.22), (3.23), (3.26), (A2.2.18) and (A2.2.21) into Eq. (3.36) yields

$$\frac{\rho_o}{2} \left[\frac{N_o^2 h^2}{2} + \frac{g \epsilon h}{\rho_o} (\overline{u}^2 + \overline{v}^2) - \frac{1}{4} VS^2 h^2 + VSh\overline{v} \right] \frac{\partial h}{\partial t}$$

$$+ \frac{\rho_o}{2} \frac{\partial}{\partial t} \int_0^h [(\Delta u)^2 + (\Delta v)^2] dz = 0 \qquad \text{(A2.2.22)}$$

which is identical to Eq. (A2.1.29). Note that in deriving the Equation (A2.2.22), the sum of $\int_0^h \Delta u z dz$ from Eq. (A2.2.18) and $\int_0^h [\int_0^z \Delta u dz'] dz$ from Eq. (A2.2.21) appears. As before, this sum can be shown to be zero by integration by parts.

A.2.2.4. The Velocity Profile Parameter

The last term of Eq. (A2.2.22) is handled in exactly the same way as in Section A.2.1.6, so that after introducing α', the energy equation again reduces to Eq. (A2.1.38). But here α' also depends on the bottom slope β.

A.2.2.5. Summary of Governing Equations

For a sloping bottom the governing equations are: the momentum equations are the same as Eqs. (3.22) and (3.23), the mass conservation equation (A2.2.17) and the energy equation (A2.1.38). For convenience, all of them are presented together as follows

$$\frac{\partial(\overline{u}h)}{\partial t} - f\overline{v}h = -\frac{1}{\rho_o}\tau_b{}^x - \frac{\epsilon g h \beta}{\rho_o} \tag{A2.2.23}$$

$$\frac{\partial(\overline{v}h)}{\partial t} + f\overline{u}h = -\frac{1}{\rho_o}\tau_b{}^y \tag{A2.2.24}$$

$$\frac{\partial(h\epsilon)}{\partial t} = -\frac{\beta_1}{g}\rho_o N_o{}^2 \overline{u}h \tag{A2.2.25}$$

$$c_*'u_*{}^2 - (\overline{u}^2 + \overline{v}^2) + \frac{N_o{}^2 h^2}{2} + \frac{\epsilon g h}{\rho_o} - \frac{2h\alpha' C_d \overline{U}\beta_1' N_o{}^2}{f}$$

$$- \beta_1'\left[\frac{N_o{}^2 \overline{v}h}{f} + \frac{\beta_1' N_o{}^4 h^2}{4f^2}\right] = 0, \tag{A2.2.26}$$

where $\beta_1 = -\dfrac{\partial \rho_o}{\partial z} \Big/ \dfrac{\partial \rho_o}{\partial z}$, $\beta_1' = \beta_1 + \beta$ and $\overline{U} = \sqrt{\overline{u}^2 + (\overline{v} + V_g)^2}$.

APPENDIX 3

A MIXED LAYER RELAXATION PROBLEM

The results obtained in Chapter 4 show that during mixed layer growth over a sloping bottom, potential energy is stored in the density field as fluid columns are advected either up or down the slope within the bottom boundary layer. The component of buoyancy parallel to the slope therefore provides an additional restoring force, and the frequency of oscillatory motion of fluid columns must be modified accordingly. This section investigates the relatively simple problem of the oscillations generated when the geostrophic flow is suddenly stopped after the mixed layer has been formed.

A.3.1. Analytic Solutions

Because "unmixing" is not allowed, the thickness will remain constant after V_g is suddenly set to zero. Therefore the governing equations for the relaxation problem become (see Eqs. 4.5 to 4.7)

$$h\frac{\partial \bar{u}}{\partial t} = f\bar{v}h - \frac{1}{\rho_o}\tau_b{}^x - \frac{\beta g}{\rho_o}h\epsilon \tag{A3.1}$$

$$h\frac{\partial \bar{v}}{\partial t} = -f\bar{u}h - \frac{1}{\rho_o}\tau_b{}^y \tag{A3.2}$$

$$\frac{\partial \epsilon}{\partial t} = \frac{1}{g}\rho_o \beta N_o{}^2 \bar{u}. \tag{A3.3}$$

The initial conditions are taken to be the values of $\bar{u}$, $\bar{v}$ and ϵ at four and half days (108 hours) during the growth of the layer with ramp function (4.9). Note

that the geostrophic velocity is zero for the relaxation problem, and therefore $\bar{u}$ and $\bar{v}$ are the same as the depth-averaged velocity components.

Using a linear drag law

$$\frac{\tau_b{}^x}{\rho_o} = r\bar{u} \tag{A3.4}$$

$$\frac{\tau_b{}^y}{\rho_o} = r\bar{v}, \tag{A3.5}$$

it can be deduced from Eqs. (A3.1) to (A3.3) that

$$\frac{d^3\bar{v}}{dt^3} + \frac{2r}{h}\frac{d^2\bar{v}}{dt^2} + \left(\frac{r^2}{h^2} + \beta^2 N_o{}^2 + f^2\right)\frac{d\bar{v}}{dt} + \frac{r\beta^2 N_o{}^2}{h}\bar{v} = 0. \tag{A3.6}$$

Eq. (A3.6) has been solved for three cases: (1) sloping bottom with no friction ($r = 0$); (2) horizontal flat bottom with friction ($\beta = 0$); (3) sloping bottom with friction.

A.3.1.1. Sloping bottom with no friction.

The solution is

$$\bar{v} = A_1 + B_1 \cos\left[f\sqrt{1 + \frac{\beta^2 N_o{}^2}{f^2}}\, t + C_1\right] \tag{A3.7}$$

where the constants A_1, B_1, and C_1 are determined by the initial conditions. These are modified inertial oscillations with frequency $f\sqrt{1 + \frac{\beta^2 N_o{}^2}{f^2}}$: that is, the frequency is slightly higher than f, being modified by the additional buoyancy force parallel to the slope as expected.

A.3.1.2. Horizontal flat bottom ($\beta = 0$) with friction.

The solution is

$$\bar{u} = -A_2 e^{-\frac{rt}{h}} \cos(ft + \phi) \tag{A3.8}$$

$$\bar{v} = -A_2 e^{-\frac{rt}{h}} \sin(ft + \phi) \tag{A3.9}$$

where the constants A_2 and ϕ are determined by the initial conditions. These are just frictionally damped inertial oscillations.

A.3.1.3. Sloping bottom with friction.

The solutions are

$$\bar{u} = u_1 A_3 e^{p_1 t} + (u_2 B_3 - u_3 C_3) e^{p_{2a} t} \cos p_{2b} t + (u_2 C_3 + u_3 B_3) e^{p_{2a} t} \sin p_{2b} t \tag{A3.10}$$

$$\bar{v} = A_3 e^{p_1 t} + B_3 e^{p_{2a} t} \cos p_{2b} t + C_3 e^{p_{2a} t} \sin p_{2b} t \tag{A3.11}$$

$$\epsilon = \epsilon_1 A_3 e^{p_1 t} + (\epsilon_2 B_3 + \epsilon_3 C_3) e^{p_{2a} t} \cos p_{2b} t + (\epsilon_2 C_3 - \epsilon_3 B_3) e^{p_{2a} t} \sin p_{2b} t \tag{A3.12}$$

where

$$a_1 = \beta^2 N_o^2 + f^2 - \frac{r^2}{3h^2} \tag{A3.13}$$

$$a_2 = \frac{r}{27h}(9\beta^2 N_o^2 - \frac{2r^2}{h^2} - 18f^2) \tag{A3.14}$$

$$b_1 = \left[-\frac{a_2}{2} + \sqrt{\frac{a_2^2}{4} + \frac{a_1^3}{27}}\right]^{\frac{1}{3}} \tag{A3.15}$$

$$b_2 = \left[-\frac{a_2}{2} - \sqrt{\frac{a_2^2}{4} + \frac{a_1^3}{27}}\right]^{\frac{1}{3}} \tag{A3.16}$$

$$p_1 = b_1 + b_2 - \frac{2r}{3h} \tag{A3.17}$$

$$p_{2a} = -\frac{b_1 + b_2}{2} - \frac{2r}{3h} \tag{A3.18}$$

$$p_{2b} = \frac{\sqrt{3}}{2}(b_1 - b_2) \tag{A3.19}$$

$$u_1 = -\frac{r}{fh} - \frac{p_1}{f} \tag{A3.20}$$

$$u_2 = -\frac{r}{fh} - \frac{p_{2a}}{f} \tag{A3.21}$$

$$u_3 = \frac{p_{2b}}{f} \tag{A3.22}$$

$$\epsilon_1 = -\frac{\rho_o r}{\beta g h}u_1 + \frac{\rho_o f}{\beta g} - \frac{\rho_o u_1 p_1}{\beta g} \tag{A3.23}$$

$$\epsilon_2 = -\frac{\rho_o r}{\beta g h}u_2 + \frac{\rho_o f}{\beta g} - \frac{\rho_o u_2 p_{2a}}{\beta g} - \frac{\rho_o u_3 p_{2b}}{\beta g} \tag{A3.24}$$

$$\epsilon_3 = \frac{\rho_o r}{\beta g h}u_3 + \frac{\rho_o u_3 p_{2a}}{\beta g} - \frac{\rho_o u_2 p_{2b}}{\beta g}. \tag{A3.25}$$

The constants A_3, B_3, and C_3 can be determined from the initial conditions.

A.3.2. Numerical Solutions

The Eqs. (A3.1) to (A3.3) are also solved numerically with both a linear drag law and quadratic drag law. The linear drag coefficient r was estimated by assuming that the range of u_* is 0.19 to 0.6 cm/s and the speed in the mixed layer $U = O(10)$ cm/s. Therefore the range of r is 3.6×10^{-3} to 3.6×10^{-2} cm/s. The range of the quadratic drag coefficient C_d was chosen as 0.2×10^{-2} to 1×10^{-2}.

The results obtained from the analytic solutions and numerical solutions are presented together for two typical cases in Figures A3.1 and A3.2. The parameter values for Fig. A3.1 are: $C_d = 0.002$, $r = 0.36\times10^{-2}$cm/s, $\beta = 1\times10^{-2}$, $N_o = 1\times10^{-2}$ /s and $V_g = 15$ cm/s. In Fig. A3.2 $C_d = 0.01$, $r = 3.6\times10^{-2}$cm/s, $\beta = -2.4\times10^{-3}$, $N_o = 1.28\times10^{-2}$ /s and $V_g = 15$ cm/s. During the growth of the layer $\alpha' = 0.5$ is used (Note that here $\frac{N_o}{f} = 203$. It is very large therefore the

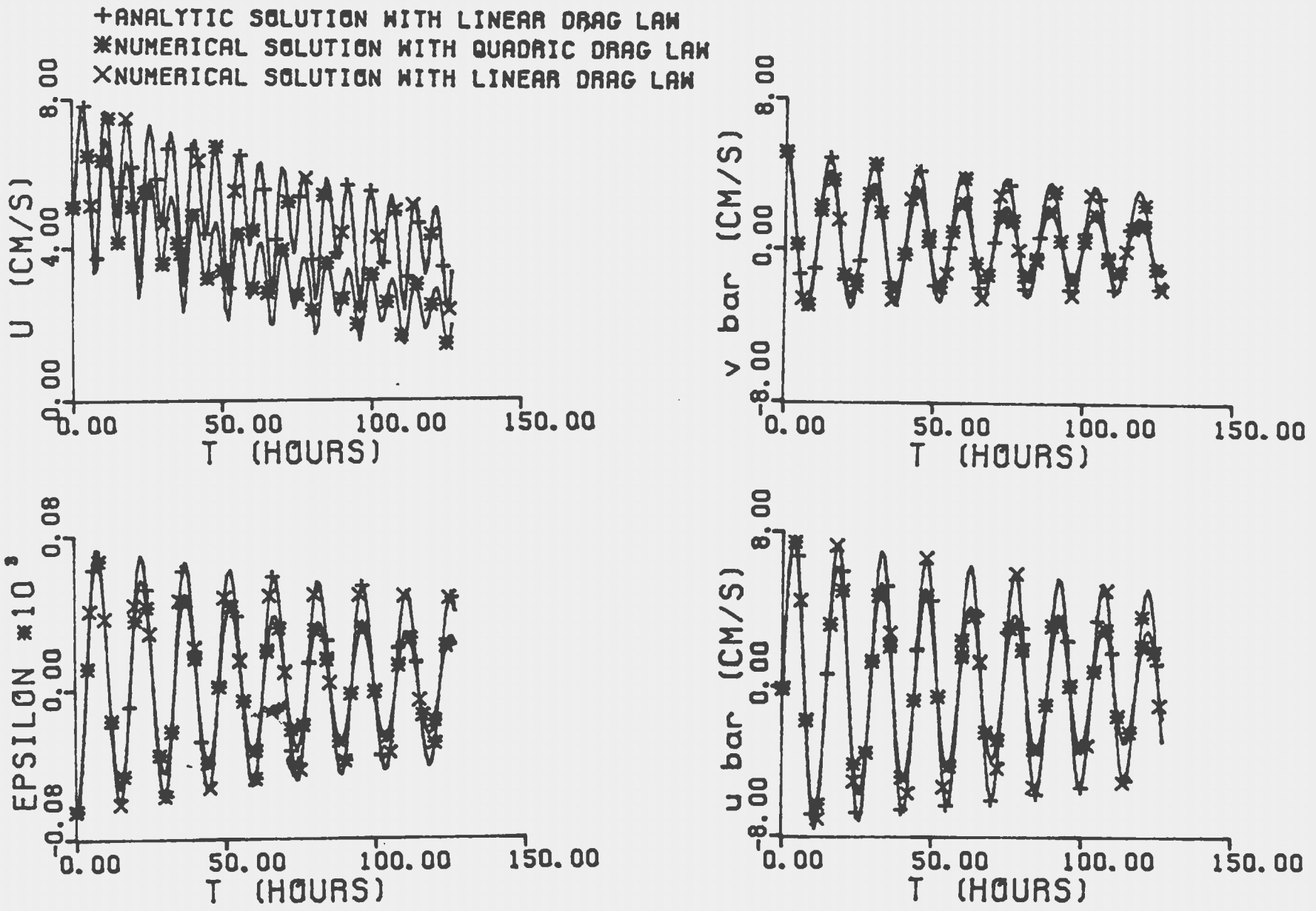

Figure A3.1. The variation of the speed, the x-component $\bar{u}$ and the y-component $\bar{v}$ of velocity, and ϵ when the geostrophic velocity is suddenly set to zero after four and half days of bottom boundary layer growth. The parameters are: $\alpha' = 2.5$, the quadratic drag law coefficient $C_d = 2\times10^{-3}$, the linear drag law coefficient $r = 0.36\times10^{-2}$cm/s, $N_o = 1\times10^{-2}$/s and $\beta = 10^{-2}$.

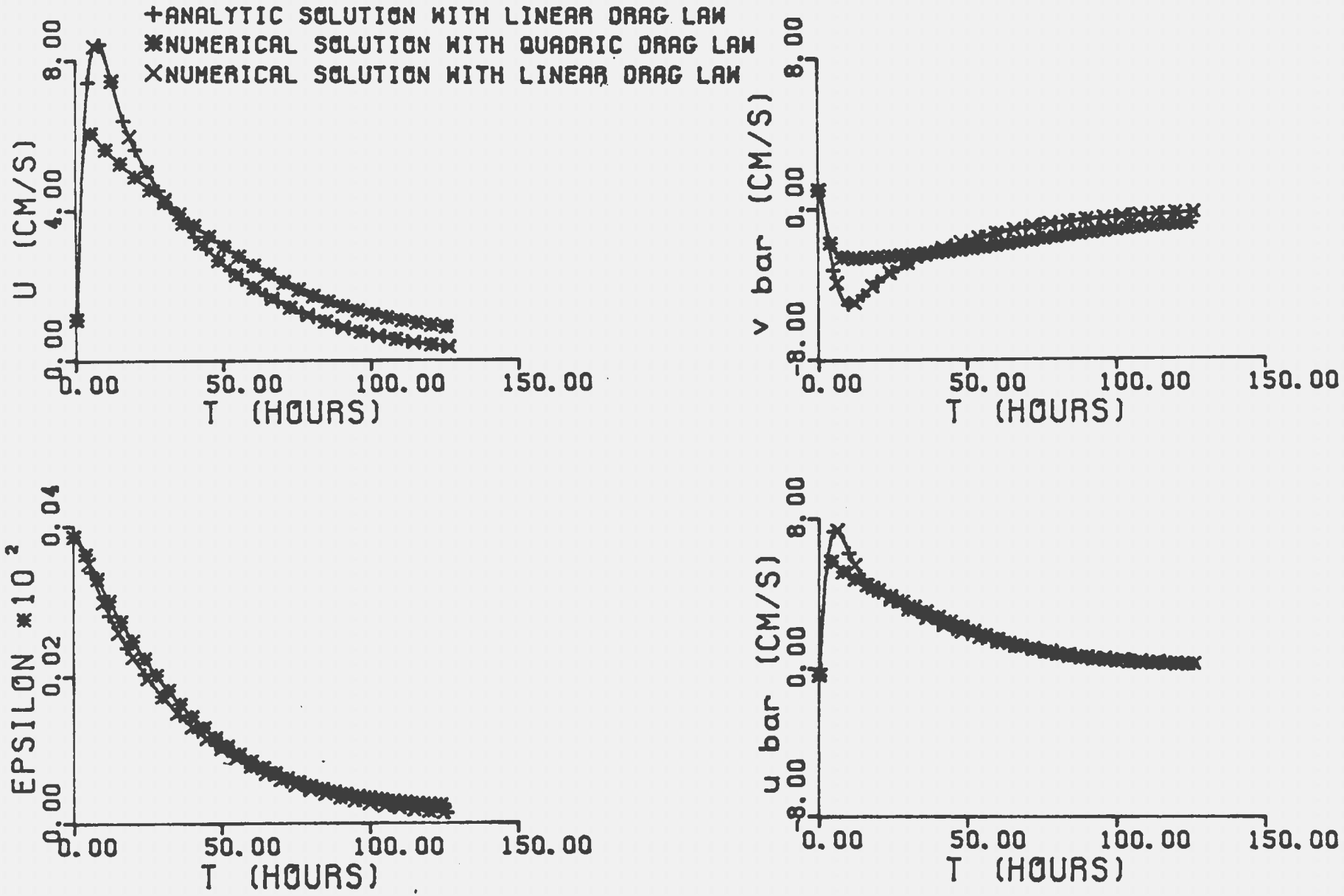

Figure A3.2. The variation of the speed, the x-component $\bar{u}$ and the y-component $\bar{v}$ of velocity, and ϵ when the geostrophic velocity is suddenly set to zero after four and half days of bottom boundary layer growth. The parameters are: $\alpha' = 2.5$, the quadratic drag law coefficient $C_d = 1\times10^{-2}$, the linear drag law coefficient $r = 3.6\times10^{-2}$cm/s, $N_e = 1.28\times10^{-2}$/s and $\beta = -2.4\times10^{-3}$.

value of α' doesn't affect the results).

The results show that the numerical solutions with a linear drag law are almost identical to the analytic solutions, and the numerical solutions with a quadratic law are very close to the analytic solutions. Figure A3.1 indicates that the flow oscillates at the modified inertial frequency and decays with time. In Fig. A3.2 the flow only decays with time and no oscillations appear because the values of the drag coefficients are an order of magnitude larger than in Fig A3.1. The decay times in Figs. A3.1 and A3.2 are long: at least two days to diminish to half the mean value.

Different values of the Brunt-Vaisala frequency, bottom slope and drag coefficient were tried. With the quadratic drag coefficient $C_d = 2\times10^{-3}$, the results for different values of β and N_o are presented in Tables A3.1-A3.4. In the Tables the oscillation frequency ω is calculated from the analytic solution with linear drag law in which ω is P_{2b}, since from Figure A3.1 based on numerical and analytic solutions there is little difference in the frequency of oscillation between the solutions with quadratic drag and with linear drag. The mean value is the average over one oscillation. The amplitude is the difference between the maximum and mean. The results show that when the bottom slope and the Brunt-Vaisala frequency increase the oscillation frequency increases. The mean flow decay rate decreases when the bottom slope and the Brunt-Vaisala frequency increase. The decay rate of oscillation amplitude in speed, ϵ and the z-component

Speed U(cm/s)						
β ($\times 10^{-3}$)	N_o ($\times 10^{-3}$ /s)	ω ($\times 10^{-4}$ /s)	Amplitude		Mean	
			$t = 0$	$t = 54$	$t = 0$	$t = 54$
10	10.	1.18	1.8	1.0	5.5	2.0
	1.	0.638	0.3	0.2	14.5	5.2
1	10.	^ 838	2.2	2.0	13.5	1.5
	1.	0.630	0.0	0.0	14.8	2.5
-10	10.	1.18	2.1	1.0	5.2	1.3
	1.	0.638	2.0	1.9	13.0	1.7
-1	10.	0.635	1.0	0.0	9.0	2.7
	1.	0.630	0.0	0.0	14.8	2.5

Table A3.1. The comparisons of results for speed between a high value of $\beta = 10^{-2}$ and a low value of $\beta = 10^{-3}$, a high value of $N_o = 10^{-2}$ /s and a low value of $N_o = 10^{-3}$ /s when $C_d = 2\times 10^{-3}$ and the Coriolis parameter $f = 0.63\times 10^{-4}$ /s.

Advective Density Anomaly ϵ ($\times 10^{-4}$g /cm ^{3})						
β ($\times 10^{-3}$)	N_o ($\times 10^{-3}$ /s)	ω ($\times 10^{-4}$ /s)	Amplitude		Mean	
			$t = 0$	$t = 54$	$t = 0$	$t = 54$
10	10.	1.18	0.73	0.3	0.1	0.0
	1.	0.638	0.027	0.012	-0.01	-0.007
1	10.	0.638	0.2	0.05	-0.75	-0.6
	1.	0.630	0.002	0.0008	-0.0036	-0.0033
-10	10.	1.18	0.65	0.18	0.13	0.0
	1.	0.638	0.015	0.003	0.09	0.08
-1	10.	0.635	0.008	0.0	2.6	2.1
	1.	0.630	0.002	0.0007	0.005	0.0045

Table A3.2. The comparisons of results for the advective density anomaly ϵ between a high value of $\beta = 10^{-2}$ and a low value of $\beta = 10^{-3}$, a high value of $N_o = 10^{-2}$ /s and a low value of $N_o = 10^{-3}$ /s when $C_d = 2\times 10^{-3}$ and the Coriolis parameter $f = 0.63\times 10^{-4}$ /s.

x-Component of Velocity $\bar{u}$ (cm/s)						
β ($\times 10^{-3}$)	N_o ($\times 10^{-3}$ /s)	ω ($\times 10^{-4}$ /s)	Amplitude		Mean	
			$t = 0$	$t = 54$	$t = 0$	$t = 54$
10	10.	1.18	8.0	2.5	-0.1	0.0
	1.	0.638	11.0	6.0	-0.3	0.0
1	10.	0.638	7.0	1.7	0.9	0.2
	1.	0.630	8.5	4.0	0.8	0.0
-10	10.	1.18	7.0	1.6	0.2	0.0
	1.	0.638	7.0	1.8	0.4	0.0
-1	10.	0.635	5.5	0.5	0.3	0.0
	1.	0.630	8.0	3.1	0.5	0.0

Table A3.3. The comparisons of results for the x-component of velocity between a high value of $\beta = 10^{-2}$ and a low value of $\beta = 10^{-3}$, a high value of $N_o = 10^{-2}$ /s and a low value of $N_o = 10^{-3}$ /s when $C_d = 2\times 10^{-3}$ and the Coriolis parameter $f = 0.63\times 10^{-4}$ /s.

y-Component of Velocity $\bar{v}$ (cm/s)						
β ($\times 10^{-3}$)	N_o ($\times 10^{-3}$ /s)	ω ($\times 10^{-4}$ /s)	Amplitude		Mean	
			$t = 0$	$t = 54$	$t = 0$	$t = 54$
10	10.	1.18	4.0	1.5	0.8	0.2
	1.	0.638	13.0	4.5	0.8	0.0
1	10.	0.638	9.1	2.1	0.7	0.0
	1.	0.630	13.2	3.5	0.9	0.1
-10	10.	1.18	3.7	1.7	-0.5	0.0
	1.	0.638	9.1	2.0	-1.7	-1.0
-1	10.	0.635	5.2	0.0	-1.6	-3.5
	1.	0.630	11.9	2.5	2.0	-0.4

Table A3.4. The comparisons of results for the y-component of velocity between a high value of $\beta = 10^{-2}$ and a low value of $\beta = 10^{-3}$, a high value of $N_o = 10^{-2}$ /s and a low value of $N_o = 10^{-3}$ /s when $C_d = 2\times 10^{-3}$ and the Coriolis parameter $f = 0.63\times 10^{-4}$ /s.

of velocity increase with increasing bottom slope and/or Brunt-Vaisala frequency, but the decay rate of oscillation amplitude of the y-component of velocity decreases when the bottom slope and/or the Brunt-Vaisala frequency increase.

REFERENCES

Armi, L. and D'Asaro, E. (1980) Flow structures of the benthic ocean. *J. Geophys. Res.*, 85, 469-484.

Armi, L. (1979) Reply to comments by C. Garrett. *J. Geophys. Res.*, 84, 5097-5098.

Armi, L. (1978) Some evidence for boundary mixing in the deep ocean. *J. Geophys. Res.*, 83, 1971-1979.

Bird, A. A. (1981) A study of the bottom boundary layer over the Eastward Scarp of the Bermuda Rise. *M.S. Thesis, Florida State Univ., Tallahasee.* 92 pp.

Bird, A. A., G. L. Weatherly and M. Wimbush (1382) A study of the bottom boundary layer over the East Scarp of the Bermuda Rise. *J. Geophys. Res.*, 87, 7941-7954.

Blackadar, A. K. and H. Tennekes (1968) Asymptotic similarity in neutral barotropic planetary boundary layers. *J. Atmos. Sci.*, 25, 1015-1020.

Bowden, K. F. (1978) Physical problems of the benthic boundary layer. *Geophysical Surveys*, 3, 255-296.

Brown, R. A. (1974) Matching classical boundary-layer solutions toward a geostrophic drag coefficient relation. *Bound.-Layer Meteor.*, 7, 489-500.

Caldwell, D. R., C. W. Van Atta and K. N. Helland (1972) A laboratory study of

the turbulent Ekman layer. *Geophys. Fluid Dyn.*, 3,125-160.

Carson, D. J. and F. B. Smith (1974) Thermodynamic model for the development of a convectively unstable boundary layer. *Advances in Geophys.*, 18A, 111-124.

Clarke, R. H., A. J. Dyer, R. R. Brook, D. G. Reid and A. J. Troup (1971) The Wangara Experiment: boundary layer data. Tech. Paper 19, Div. Meteor. Phys., CSIRO Australia, 363 pp, ISBN 0643 00648 6. NTIS N71-37838.

Csanady, G.T. (1967) On the resistance law of a turbulent Ekman layer. *J. Atmos. Sci.*, 24, 467-471.

Dewey, R. K. (1987) Turbulent energy dissipation over the continental shelf. *Ph. D thesis. Univ. of British Columbia.*, 163 pp.

Dickey, T. D. and J. C. Van Leer (1984) Observations and simulation of a bottom Ekman layer on a continental shelf. *J. Geophys. Res.*, 89, 1983-1988.

Ekman, V. W. (1905) On the influence of the earth's rotation on ocean currents. *Arkir. Mat. Astron. Fysik* 2(11), 1-53.

Garrett, C. N. (1979) Comment on ' Some evidence for boundary mixing in the deep ocean ' by Laurence Armi. *J. Geophys. Res.*, 84, 5095.

Garrett, C. N. (1990) The role of secondary circulation in boundary mixing. *J. Geophys. Res.*, 95, C3, 3181-3188.

Geisler, J. E. and E. B. Kraus (1969) The well-mixed Ekman boundary layer. *Deep-sea Research* 16, 73-84.

Gill, A. E. (1982) Atmosphere-Ocean Dynamics. Academic Press. 663 p.

Gutman, L. N. (1969) Vvedeniye v nelineynuyu teoriyu mezometeorologicheskikh protsessov (Introduction to the nonlinear theory of mesometeorological processes). Gidrometeoizdat Press. 224p.

Howroyd, G. C. and P. R. Slawson (1975) The characteristics of a laboratory produced turbulent Ekman layer. *Boundary Layer Meteorol.* 8, 201-219.

Kline, S. J., W. C. Reynolds, F. A. Schraub and P. W. Runstadler (1967) The structure of turbulent boundary layers. *J. Fluid Mech.*, 30, part 4, 741-773.

Kraus, E. B. (1968) What we do not know about the sea surface wind stress. *Bull. Am. Met. Soc.*, 49, 247-253.

Krauss, Wolfgang (1973) Methods and results of theoretical oceanography. Vol. I, Dynamics of the homogeneous and the quasihomogeneous ocean. *Borntraeger, Berlin.* 302 pp.

Mahrt, L and D. H. Lenschow (1976) Growth dynamics of the convectively mixed layer. *J. Atmos. Sci.*, 33, 41-51.

Manins, P. C. (1982) The daytime planetary boundary layer: A new interpretation of Wangara data. *Quart. J. R. Met. Soc.*, 108, 689-705.

Mellor, G. L. (1973) Analytic prediction of the properties of stratified planetary surface layers. *J. Almos. Sci.*, 30, 1061-1069.

Mellor, G. L. and T. Yamada (1974) A hierarchy of turbulence closure models for plantary boundary layers. *J. Atmos. Sci.*, 31, 1791-1806.

Mercado, A. and J. Van Leer (1976) Near bottom velocity and temperature profiles observed by cyclosonde. *Geophys. Res. Lett.*, 3, 633-636.

Mofjeld, H. O. and J. W. Lavelle (1984) Setting the length scale in a second order closure model of the unstratified bottom boundary layer. *J. Phys. Oceanogr.*, 14,833-839

Monin, A. S. and A. M. Yaglom (1979) Statistical fluid mechanics: mechanics of turbulence. Vol. 1. MIT press (English translation). 769 pp.

Nowell, A. R. M. (1983) The benthic boundary layer and sediment transport. *Reviews of Geophysics and Physics*, Vol. 21, No.5, 1181-1192.

Ng, K. H. and D. B. Spalding (1972) Turbulence model for boundary layers near walls. *Phys. Fluids*, Vol. 15, 20-30.

Pao, Richard H. F., (1961) Fluid dynamics. John Wiley & Sons, Inc., New York. 502 p.

Phillips, O. M. (1970) On flows induced by diffusion in a stably stratified fluid. *Deep-Sea Res.*, 17, 435-443.

Phillips, O. M., J.-H. Shyu and H. Salmun (1986) An experiment on boundary mixing: Mean circulation and transport rates. *J. Fluid Mech.*, 173, 473-499.

Pollard, R. T., R. B. Rhines and R. O. R. Y. Thompson (1973) The deepening of the wind-mixed layer. *Geophys. Fluid Dyn.*, 3, 381-404.

Pond, S. and Jeorge L. Pickard (1978) Introductory Dynamic Oceanography. Pergamon Press. 241 pp.

Price, J. F., R. A. Weller and R. Pinkel (1986) Diurnal cycling: Observations and models of the upper ocean response to diurnal heating, cooling and wind mixing. *J. Geophys. Res.*, C-91, July, 8411-8427.

Rhines, P and P. MacCready (1989) Boundary control over the large-scale circulation. *Proceedings of the fifth 'Aha Huliko'a Hawaiian winter workshop on parameterization of small-scale processes*, 75-97, Hawaii Institute of Geophysics, Honolulu.

Richards, K. J. (1982) Modeling the benthic boundary layer. *J. Phys. Oceanogr.*, 12, 428-439.

Riehl, H., T. C. Yeh, J. S., Malkus and N. E. La Seur (1951) The northeast trades of the Pacific Ocean. *Q. J l. R. Met. Soc.*, 77, 598-628.

Tennekes, H. and J. L. Lumley (1972) A first course in turbulence. The MIT Press. 300 p.

Thompson, R. O. R. Y. (1973) Stratified Ekman boundary layer models. *Geophysical Fluid Dynamics*, 5, 201-210.

Thorpe, S. A. (1987) Current and temperature variability on the continental slope. *Philos. Trans. R. Sci. London, ser. A*, 323, 471-517.

Tritton, D. J. (1977) Physical fluid Dynamics. *Van Nostrand Reinhold Company Ltd.*, 362 pp.

Turner, J. S., (1973) Buoyancy effects in fluids. Cambridge Univ. Presss, 367 pp.

Van Leer, J. C. and A. E. Ross (1979) Velocity and temperature data observed by Cyclesonde during Joint II off the coast of Peru, *CUEA Data Rep.* 61, *RSMAS Data Rep. DR79-2,* Univ. of Miami, Miami, Flo.

Weatherly, G. L. (1975) A numerical study of time-dependent turbulent Ekman layers over horizontal and sloping bottom. *J. Phys. Oceanogr.*, 5, 288-299.

Weatherly, G. L. and P. J. Martin (1978) On the structure and dynamics of the oceanic boundary layer. *J. Phys. Oceanogr.*, 8, 557-570.

Weatherly, G. L. and J. Van Leer (1977) On the importance of stable stratification to the structure of the bottom layer on the western Florida Shelf. *Bottom Turbulence,* J. Nihoul, Ed., Elsevier, 103-122.

Weatherly, G. L.,S. L. Blumsack and A. A. Bird (1980) Notes and correspondence on the effect of diurnal tidal currents in determining the thickness of the turbulent Ekman bottom boundary layer. *J. Phys. Oceanogr.*, 10, 297-300.

Weatherly, G. L. and M. Wimbush (1980) Near-bottom speed and temperature observations on the Blake-Bahama Outer Ridge. *J. Geophys. Res.*, 3971-3981.

Wimbush, M., and W. Munk (1970) The benthic boundary layer. *The Sea.* Vol.4, Part 1, Wiley, pp. 731-758.

Wunsch, C. (1970) On oceanic boundary mixing. *Deep-Sea Res.*, 17, 293-301

Wyngaard, J. C. and O. R. Cote (1971) The budgets of turbulent kinetic energy and temperature variance in the atmospheric surface layer. *J. Atmos. Sci.*, 28, 190-201.

Yamada, T. and G. Mellor (1975) A simulation of the Wangara atmospheric boundary layer data. *J. Atmos. Sci.*, 32, 2309-2329.

Zilitinkevich, S. S. (1972) On the determination of the height of the Ekman layer. *Boundary-Layer Meteorol.*, 3, 141-145.

Zilitinkevich, S. S. (1970) Dynamics of the atmosphere's boundary layer. Hydrometeorological publishing house, Leningrad. 291 p.